Time Resolved Laser Induced Incandescence Analysis of Metal Aerosols

by

Nigel Roshan Singh

A thesis

presented to the University of Waterloo

in fulfillment of the

thesis requirement for the degree of

Master of Applied Science

in

Mechanical and Mechatronics Engineering (Nanotechnology)

Waterloo, Ontario, Canada, 2016

Author's Declaration

I hereby declare that I am the sole author of this thesis. This is a true copy of the thesis, including any required final revisions, as accepted by my examiners.

I understand that my thesis may be made electronically available to the public.

Abstract

Synthetic nanoparticles are finding widespread adoption in a growing number of commercial and research applications. Their size dependent properties offer researchers a variety of ranging including targeted drug delivery, catalysis, and environmental remediation. As these materials are being adopted into these applications, there is a pressing need for a diagnostic which allows the accurate real time measurement of the particle size since the functionality of the nanoparticles are size dependent. Time-resolved laser-induced incandescence (TiRe-LII) is an *in situ* technique which allows the non-destructive inference of the nanoparticle size in real time. This technique was developed as a particle size diagnostic for soot primary particles and has been modified to characterize synthetic nanoparticles. The aerosolized nanoparticles are heated with a laser pulse to its incandescence temperature and the incandescence is measured as the nanoparticles are allowed to thermally equilibrate with the surrounding gas. As nanoparticles of different sizes will cool at different rates, the nanoparticle size can be inferred by modeling the incandescence using a spectroscopic and heat transfer model.

The present work summarizes experiments conducted on aerosolized iron, silver, and molybdenum nanoparticles using TiRe-LII analysis. This includes the spectroscopic and heat transfer models, TiRe-LII instrument calibration and operating conditions, the nanoparticle preparation, comparisons of the TiRe-LII derived particle sizes to existing *ex situ* techniques, and the associated error analysis. The models required to interpret the TiRe-LII data, the spectroscopic and heat transfer models, are presented with the optical and physical parameters to solve them, as well as simulate the expected heat transfer modes of each of the nanoparticles. The calibration of the apparatus used as well as the nanoparticle preparation, and TiRe-LII experimental measurement methods are discussed, as well as the error bounds on the results.

A fluence study was conducted by looking at the peak temperatures measured as a function of the fluence of the TiRe-LII instrument laser to determine the accuracy of the optical properties and to compare the results to the trends to previous studies. The nanoparticle size and thermal accommodation coefficient (TAC) of each of the aerosolized nanoparticle mixtures were attempted to be recovered based on the heat transfer modes present in the TiRe-LII measurements. The aerosolized iron nanoparticles had sufficient evaporation and conduction heat transfer modes which allowed the recovery of both the nanoparticle size and thermal accommodations coefficient, while the aerosolized silver nanoparticles only

had heat transfer due to evaporation which only allowed the recovery of the nanoparticle size, and the aerosolized molybdenum nanoparticles only had heat transfer due to conduction which only allowed the recovery of the nanoparticle size to TAC ratio. The molybdenum TAC was recovered by introducing the *ex situ* calculated molybdenum nanoparticle size and nanoparticle size distribution, using electron microscopy, into the models. Finally, the error bounds for the TiRe-LII measurements are presented, and a perturbation analysis was performed due to the lack of provided error bounds on the optical and physical properties used. It was shown that the optical properties had a significant impact on the recovered nanoparticle size and TAC for all of the materials, while there was a lesser but non-trivial impact on the recovered values from the nanomaterials' physical properties.

Acknowledgements

I would like to thank my supervisor Dr. Kyle Daun for giving me the opportunity to become involved in an exciting research field. I would like to thank him for his support and understanding throughout the study.

I would like to thank the collaborators who have also helped me with the technical aspects throughout this study. I would like to thank Mr. Navid Bizmark for his assistance with the iron nanoparticle experiments, Mr. Robert Liang for his assistance with the silver nanoparticle experiments and Mr. Andrew Kacheff for his valuable insight on the *ex situ* analysis. I would like to thank Dr. Zhongchao and Raheleh Givehchi for access and their assistance with the TSI atomizer system.

I would like to thank my readers Dr. Kyle Daun, Dr. Ehsan Toyserkani, and Dr. Zhongchao Tan for their time and insight for reviewing this study.

Finally, I would like to thank my family, colleagues from the Radiative Heat Transfer group (including Josh Rasera, Noel Chester, Kamal Jhajj, Roger Tsang, Sam Grauer, Natalie Field, and Paul Hadwin) for their assistance throughout the completion of this degree.

Table of Contents

Author's Declaration ii
Abstract iii
Acknowledgements v
Table of Contents vi
List of Figures viii
List of Tables x
Nomenclature xi
Chapter 1 Introduction 1
1.1 Motivation 1
1.2 Background 4
1.2.1 TiRe-LII studies on synthetic metal nanoparticles size characterization 4
1.2.2 TiRe-LII studies on TAC 6
1.3 Motivation of Present Work and Thesis Outline 7
Chapter 2 TiRe-LII Theory and Methods 10
2.1 Spectroscopic Model 10
2.2 Nanoparticle Cooling Model 12
2.3 Material Properties 15
2.3.1 Spectroscopic Properties 15
2.3.2 Nanoparticle Cooling Properties 22
2.3 Nanoparticle Size and TAC Inference, and Uncertainty Quantification 27
Chapter 3 Experimental Apparatus 29
3.1 TiRe-LII Experimental Overview 29
3.2 TiRe-LII Subsystem 31
3.3 TSI Atomizer Subsystem 35
3.4 *Ex Situ* Characterization 36
Chapter 4 Experimental Procedure 39
4.1 Nanoparticle Preparation 39
4.1.2 Iron Nanoparticle Preparation 40
4.1.3 Silver Nanoparticle Preparation 41
4.1.4 Molybdenum Nanoparticle Preparation 44
4.2 TiRe-LII Measurement Procedure 46

4.2.1 Preparation and Inspection 46
4.2.2 Nanocolloid Synthesis and Setup 46
4.2.3 Activate TiRe-LII Apparatus 46
4.2.3 Shut Down and Cleanup 47
4.3 Laboratory Safety 47
Chapter 5 Results 48
5.1 Fluence and Spectroscopic Results 48
5.2 TiRe-LII Nanoparticle Size and TAC Analysis 55
5.2.1 Nanoparticle size and TAC recovery 55
5.2.2 Perturbation Analysis 64
Chapter 6 Conclusions and Future Work 67
References 69

List of Figures

Fig. 1 Magnetic response curves for iron oxide [3] 2
Fig. 2 Schematic of a TiRe-LII experimental measurement [22] 3
Fig. 3 Cooling curves for a simulated iron nanoparticle at different sizes. 4
Fig. 4 Experimental iron nanoparticle incandescence and calculated effective temperature. 12
Fig. 5 Real and imaginary components of the refractive index for molten iron 17
Fig. 6 $E(\mathbf{m}_\lambda)$ values molten iron 18
Fig. 7 Real and imaginary components of the refractive index for molten silver 19
Fig. 8 $E(\mathbf{m}_\lambda)$ values molten silver 20
Fig. 9 Real and imaginary components of the refractive index for molybdenum 21
Fig. 10 $E(\mathbf{m}_\lambda)$ values for molybdenum at different temperatures 22
Fig. 11 Heat transfer modes for a simulated iron nanoparticle 24
Fig. 12 Heat transfer modes for a simulated silver nanoparticle 25
Fig. 13 Heat transfer modes for a simulated molybdenum nanoparticle 26
Fig. 14 Marginalization plot for a Fe-Ar aerosol 28
Fig. 15 Schematic of the TiRe-LII experimental apparatus [28]. 29
Fig. 16 Relative pressure changes during a TiRe-LII Experiment 31
Fig. 17 Beam profile results of a) the direct laser beam, and b) the laser beam passing through the ceramic aperture and relay lens. 32
Fig. 18 TiRe-LII Apparatus showing a) aperture and lens system, b) window 1, c) pyroelectric sensor 33
Fig. 19 TiRe-LII Apparatus showing a) collection aperture wheel, b) density filter wheel, c) beam splitter and the wavelength specific PMTs 34
Fig. 20 TSI atomizer subsystem, aerosolizing an iron nanocolloid 35
Fig. 21 Preparation of the TEM grids 38
Fig. 22 Nanocolloids of: a) iron; b) silver; c) molybdenum 40
Fig. 23 Sample TEM images of the iron nanoparticles, a) a larger nanoparticle showing the CMC coating, b) a smaller nanoparticle. Scale bars corresponds to 50 nm in both images. 41
Fig. 24 Sample SEM image of the silver nanoparticles 42
Fig. 25 Silver Nanoparticle SEM Histogram 43
Fig. 26 Sample TEM image of a molybdenum nanoparticle cluster 44
Fig. 27 Molybdenum Nanoparticle TEM Histogram 45

Fig. 28 Peak temperature vs fluence for iron nanoparticles 50
Fig. 29 Comparison of the $E(\mathbf{m}_{\lambda laser})$ from this study to the literature and Mie theory for iron 51
Fig. 30 Peak temperature vs fluence for silver nanoparticles 52
Fig. 31 Peak temperature vs fluence for molybdenum nanoparticles 53
Fig. 32 Peak temperature vs fluence for silver nanoparticles for $E(\mathbf{m})_r = 0.366$ and $E(\mathbf{m})_r = 1$ 54
Fig. 33 Plot of the experimental and modeled temperatures for the Fe-Ar aerosol 56
Fig. 34 Contour plot of the likelihood for the Fe-Ar aerosol 57
Fig. 35 Iron nanoparticle colloid colour at: a) synthesis completion; b) one hour; c) six hours 57
Fig. 36 Time evolution of the TAC for a Fe-Ar mixture during a TiRe-LII experiment 58
Fig. 37 Plot of the experimental and modeled temperatures for the Ag-Ar aerosol 60
Fig. 38 Contour plot of the likelihood for the Ag-Ar aerosol 61
Fig. 39 Plot of the experimental and modeled temperatures for the Mo-Ar aerosol 63
Fig. 40 Contour plot of the likelihood for the Mo-Ar aerosol 63
Fig. 41 Perturbation analysis results for the nanoparticle size (left) and TAC (right) for iron 65
Fig. 42 (Left) Perturbation analysis results for the nanoparticle size for silver 66
Fig. 43 (Right) Perturbation analysis results for the TAC for molybdenum 66

List of Tables

Table 1 Nanoparticle Cooling Properties 23

Table 2 Laser Energy Measurements 34

Table 3 Iron nanoparticle TiRe-LII size and TAC analysis 56

Table 4 Silver nanoparticle TiRe-LII size analysis 60

Table 5 Molybdenum nanoparticle TiRe-LII TAC analysis using the TEM nanoparticle size 62

Table 6 Sensitivity analysis overview of parameters and perturbation factors 64

Nomenclature

Latin Symbols

Symbol	Unit	Definition
b	-	Observed data
C	Pa	Clausius-Clapeyron material constant
$c_{g,t}$	$m \cdot s^{-1}$	Mean thermal speed of gas molecules
$c_{v,t}$	$m \cdot s^{-1}$	Mean thermal speed of vapor molecules
c_0	$m \cdot s^{-1}$	Speed of light in a vacuum, $3.00 \cdot 10^8$
c_p	$J \cdot kg^{-1} \cdot K^{-1}$	Specific heat capacity
c_v	$m \cdot s^{-1}$	Thermal speed of evaporating atoms
D	$m^2 \cdot s^{-1}$	Diffusion coefficient
d_p	Nm	Particle size
E	J	Energy
E_i	J	Pre-scattering energy of gas molecule
E_o	J	Post scattering energy of gas molecule
$E(\mathbf{m}_\lambda)$	-	Complex absorption function
h	J·s	Planck's constant
Δh_v	$J \cdot atom^{-1}$	Enthalpy of vaporization
$\Delta h_{v,b}$	$J \cdot atom^{-1}$	Enthalpy of vaporization at the material boiling point
$I_{b\lambda}$	W	Blackbody radiation at wavelength λ
J_λ	a.u.	Incandescence at wavelength λ
$K(d_p,t)$	-	Kernal of the incandescence equation
K	$J \cdot atom^{-1}$	Material constant in Watson's equation
k_b	$J \cdot mol^{-1} \cdot K^{-1}$	Boltzmann's constant, $1.38 \cdot 10^{-23}$
K_{opt}	-	Optical constant in the effective temperature equation
k_λ	-	Imaginary component of the complex index of refraction
m_g	$kg \cdot mol^{-1}$	Molecular mass of a gas molecule
m_s	$kg \cdot atom^{-1}$	Mass of a surface atom
m_v	$kg \cdot atom^{-1}$	Mass of vapor atoms
M_v	$kg \cdot mol^{-1}$	Molar mass of vapor

$\mathbf{m}_\lambda$	-	Complex index of refraction
N_A	atoms·mol^{-1}	Avogadro's number
n_g	atoms·m^{-3}	Gas number density
N_g	atoms·s^{-1}·m^{-2}	Incident number flux of gas atoms
N_v	atoms·s^{-1}·m^{-2}	Vapor molecular umber flux
n_λ	-	Real component of complex index of refraction
P(**b**)	-	Evidence
P(**b**|**x**)	-	Likelihood
P(d_p), P(d_p,**x**)	-	Probability density of nanoparticles having size d_p
P(**x**|**b**)	-	Posterior distribution
p_g	Pa	Gas pressure
p_g	Pa	Gas pressure
$P_{pr}(x)$	-	Prior distribution
p_v	Pa	Vapor pressure
$p_{v,o}$	Pa	Vapor pressure of bulk material
$Q_{abs,\lambda}(d_p)$	-	Absorption efficiency at wavelength λ
q_{cond}	W	Conduction heat transfer
q_{evap}	W	Evaporation heat transfer
q_{rad}	W	Radiation heat transfer
R	J·mol^{-1}·K^{-1}	Universal gas constant
R_S	J·kg^{-1}·K^{-1}	Specific gas constant
t	ns	Time
T_b	K	Boiling temperature
T_{cr}	K	Critical temperature
T_{eff}	K	Effective temperature
T_g	K	Gas temperature
T_p	K	Particle temperature
T_{p0}	K	Peak temperature
x	-	Size parameter
x	-	Vector of parameters of interest

Greek Symbols

Symbol	Unit	Definition
α	-	Thermal accommodation coefficient (TAC)
β	-	Collision efficiency
γ_s	$N \cdot m^{-1}$	Surface tension of nanoparticle surface
λ	nm	Wavelength
ρ	$kg \cdot m^{-3}$	Density
σ_j	K, a.u.	Standard deviation or noise in observed data
ζ_{rot}	-	Rotational degrees of freedom of a gas molecule

Subscripts

Subscript	Definition
exp	Experimental
g	Gas
i	Initial
i, j, k	Indices
mod	Modelled
o	Out/final
p	Particle
s	Surface
v	Vapor

Abbreviations

Abbreviation	Definition
CMC	Carboxymethyl cellulose
DLS	Dynamic light scattering
MLE	Maximum likelihood estimator
RSC	Relative sensitivity coefficient
SEM	Scanning electron microscopy
TEM	Transmission electron microscopy
TiRe-LII	Time-resolved laser-induced incandescence

Chapter 1 Introduction

1.1 Motivation

Synthetic metallic nanoparticles have found widespread adoption in a variety of disciplines due to their unique size-dependent chemical and electromagnetic properties, many of which deviate from their bulk counterparts. These properties have been integrated into applications that range from environmental remediation, catalysis, optical devices, antimicrobial coatings, and chemical sensors [1]. For example, iron nanoparticles have been a potential material candidate in research for drug delivery, environmental remediation, and catalytic processes [2], based on its size dependant magnetic properties. The magnetic properties for iron oxide nanoparticles are demonstrated in the magnetic response curves for particle sizes of 4-15 nm, shown in **Fig.** 1 [3], and this result has been incorporated into research including medical contrast imaging materials [4] and catalysis [5]. Silver nanoparticles have been well studied for their antimicrobial properties and have been considered as a promising candidate to combat the evolution of antibiotic resistant bacteria [6].

It is critical that there are real time diagnostics available to provide information on whether the nanoparticles are synthesized at the appropriate size for the desired material property or if there is an underlying experimental issue. Gas phase synthesis is a preferred route for large scale production of nanoparticles due to its ease with scaling up and mass production processes but a potential drawback of these synthesis techniques is that there are limited real time diagnostics available to provide *in situ* nanoparticle size and size distribution measurements to ensure the appropriate particle size or size range are being synthesized for the intended application. While online *ex situ* methods, including scanning mobility particle size characterization could provide this information, they are sometimes limited in the aerosol applications they can be applied to due to probing restrictions. Offline *ex situ* methods, including electron microscopy and surface characterization techniques such as and gas adsorption/desorption characterization, are commonly utilized to determine the nanoparticle size and distribution characteristics, and whether isolated nanoparticles or fractal aggregates of the primary particles are present with the key drawbacks being this information is determined after the nanoparticle synthesis is over, and can be time consuming.

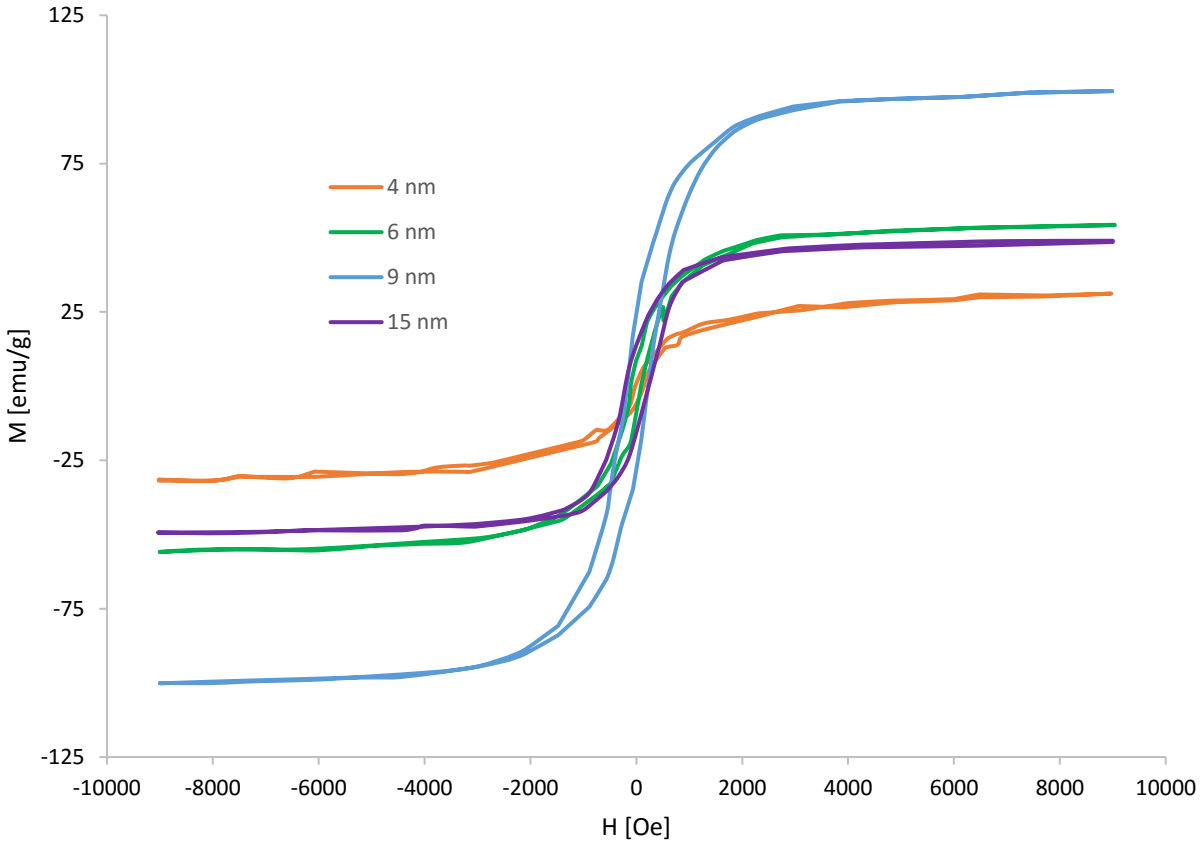

Fig. 1 Magnetic response curves for iron oxide nanoparticles at different particle sizes [3]

Additionally, there is a demand for a diagnostic which can aid with assessing the potential impact of synthetic nanoparticles on the environment and human health [1]. The health and safety concerns of many nanomaterials are still not fully known as research into their impact on the environment and organisms are limited, although there have been efforts to improve upon this knowledgebase as nanomaterial usage increases. The literature available for iron nanoparticle toxicology has weakly suggested that they have an adverse effects on animal cells, plant cells, and human cells [7]. Specifically, human bronchial epithelium cells, a component of the respiratory system, were observed to die in the presence of saline solutions with iron nanoparticles dissolved in them although there are only limited studies on this topic [8, 9]. Research on the toxicology of silver nanoparticles have also suggested that for oral exposure, such as in the case for aerosolized nanoparticles, the intestinal tract and liver are generally the primary targets, although inflammation and accumulation of other organs has been observed [10]. The lack of information for silver nanoparticles is particularly concerning due to its widespread use in

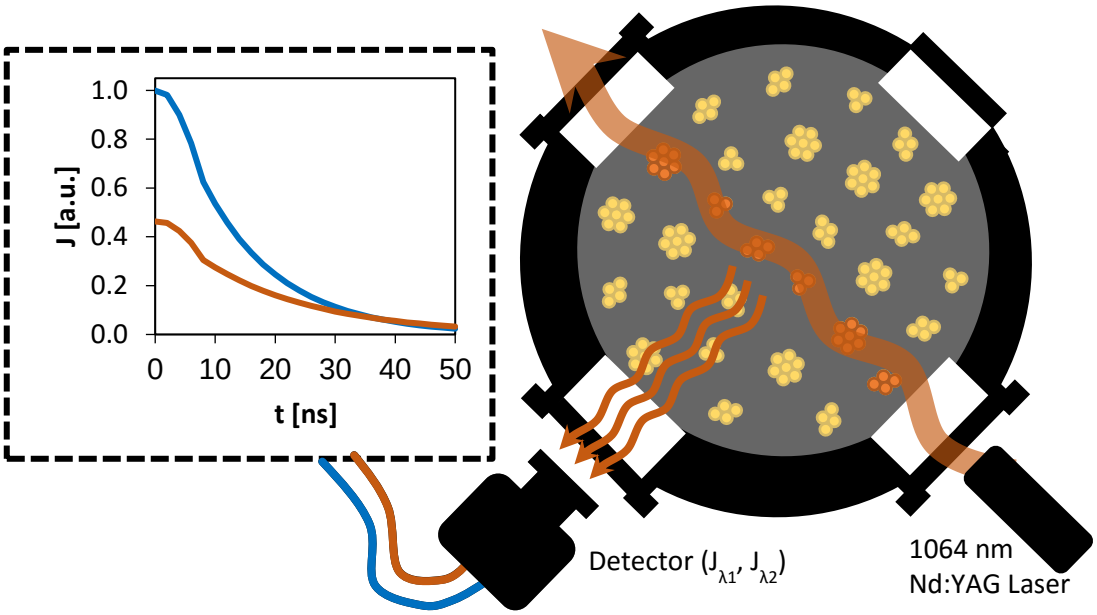

Fig. 2 Schematic of a TiRe-LII experimental measurement [22]

biological research and applications [1, 6, 11]. While there have been review papers identifying the health concerns of iron and silver nanoparticle safety, or lack of research so far, there have been very limited research on molybdenum nanoparticles as it has not seen as widespread adoption yet. While there is very limited toxicology literature for molybdenum nanoparticles, they have been shown to reduce cellular mitochondrial function and inducing cell plasma membrane leakage, causing irreversible cellular damage [12].

Time-resolved laser-induced incandescence (TiRe-LII), a real time combustion diagnostic mainly used for sizing soot primary particles [13, 14, 15], has been extended to measure synthetic zero-valent metal nanoparticles including silver [16], iron [17, 18], molybdenum [19, 20] and silicon [21]. In a TiRe-LII experiment, a laser pulse heats nanoparticles in a sample volume of an aerosol, and the spectral incandescence is measured, usually at multiple wavelengths, as the aerosolized nanoparticles thermally equilibrate with the carrier gas, shown schematically in **Fig.** 2 [22]. An instantaneous effective temperature can be calculated from the measured incandescence data if the radiative properties of the nanoparticles are known. Since smaller nanoparticles cool at a faster rate than larger ones, the nanoparticle size distribution can be inferred by regressing the experimental effective temperature to data generated with a heat transfer model. This model is influenced by parameters which include the nanomaterial's density, specific heat, radiative properties, and thermal accommodation coefficient (TAC,

α), which quantifies the average energy transferred when a gas molecule scatters from the energized nanoparticle. Using these parameters, the cooling curves for a simulated iron nanoparticle can be determined and is shown in **Fig.** 3. In conduction-dominated cooling, it is possible to infer the nanoparticle size to TAC ratio from the effective temperature decay [23], and the TAC can be calculated if the nanoparticle size is known through independent means such as electron microscopy characterization. Kock et al. [18] showed that if sufficient amounts of both conduction and evaporation are present, then the average nanoparticle size and TAC can be inferred simultaneously using nanoparticles of a known distribution type and width.

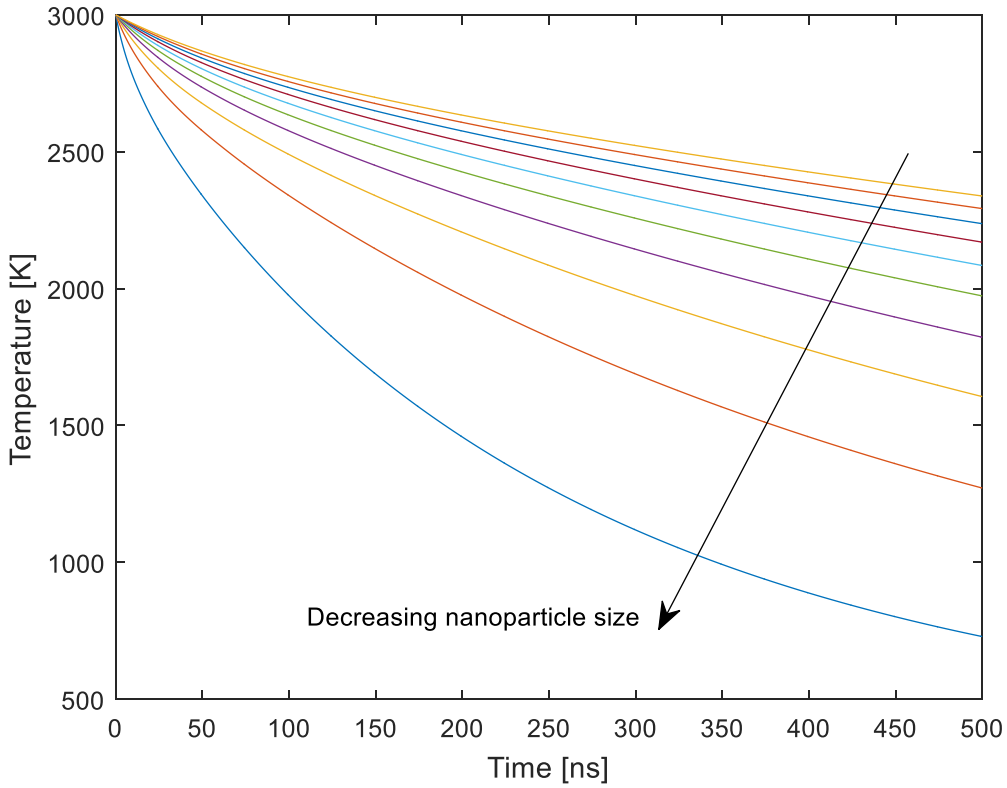

Fig. 3 Cooling curves for a simulated iron nanoparticle at different sizes

1.2 Background

1.2.1 TiRe-LII studies on synthetic metal nanoparticles size characterization

TiRe-LII was originally a soot diagnostic, which provided real time *in situ* particle size measurements. One of the key advantages was that only an aerosolized particle stream was required to be analysed, and thus the constraints of physical probing of a system were greatly reduced. This allowed

TiRe-LII measurements to be performed in applications ranging from diesel internal combustion engine [24] to larger aero-engines [25]. The sampling and size measurements of the aerosol during a TiRe-LII experiment is within an enclosed environment since the laser module and the sample chamber are both sealed, which is a significant advantage due to the potential health concerns of using nanoparticles.

While the heating of materials using laser pulses was not a novel concept, one the earliest attempts to perform TiRe-LII size measurements on synthetic nanoparticles were by Vander Wal et al. in 1999 [26]. The study included TiRe-LII measurements on iron, molybdenum, titanium, and tungsten, although the particle sizes were not recovered. This study did provide that in principle, the nanoparticle size could be recovered if the nanoparticle cooling could be modelled accurately, which was still being developed at the time.

An early attempt to recover the nanoparticle size was by Fillippov et al. [16], who studied ultrafine silver, graphite, and titanium nitride nanoparticles. The nanoparticle size calculations from the TiRe-LII measurements were erroneous as the conduction model used did not incorporate the temperature dependent properties of the system, as well the study made the assumption that the thermal accommodation coefficient was unity, which further research has suggested this value is not likely [27]. Furthermore, this study also reframed the determination of the nanoparticle size characteristics as solving a Fredholm integral equation of the first kind, which is an inherently ill-posed problem but has many well developed methods for solving and quantifying the error.

Murakami et al. [19] performed TiRe-LII measurements on molybdenum nanoparticles formed by laser induced photolysis of $Mo(CO)_6$ in different carrier gases. While the study was able to determine the different aerosolized Mo nanoparticle sizes, there were several underlying issues with this study including: the nanoparticles were assumed to be monodisperse while they are likely to be polydisperse; the study utilised the heat transfer model from Filippov et al. [16] which made the assumption that the TAC was unity; and material and gas properties used for the models were not temperature dependant. A reanalysis of this study was conducted by Sipkens et al. [20] to address these deficiencies by implementing an experimentally supported lognormal nanoparticle size distribution of σ_g = 1.5 [18], implemented temperature dependent properties, and attempted to recover the nanoparticle size and TAC instead of assuming TAC = 1 and recovering only the nanoparticle size. This study showed that unlike materials such as iron which have sufficient evaporation and conduction heat transfer modes which allow the

simultaneous determination of the nanoparticle size and TAC [18], the heat transfer of refractory materials occur in the conduction only regime and the heat transfer model has the nanoparticle size and TAC as a fixed ratio. To determine either the nanoparticle size or the TAC would require further *ex situ* information, such as using electron microscopy to determine the nanoparticle size and then using that in the model to determine the TAC.

1.2.2 TiRe-LII studies on TAC

To take into account of the TAC and how it influences TiRe-LII measurements, researchers started determining the nanoparticle sizes from an alternative *ex situ* method, the preferred being transmission electron microscopy (TEM), to determine the nanoparticle size and size distribution, and then using this information to determine the material's TAC. Kock et al. [18] utilised this method and attempted to simultaneously recover the TAC and particle size from TiRe-LII measurements, based off of the lognormal size distribution observed in TEM data of iron nanoparticles synthesized by the decomposition of $Fe(CO)_5$ to iron nanoparticles using a hot wall reactor. It was found that the TAC was approximately 0.13 for iron nanoparticles in both argon and nitrogen and the TiRe-LII particle sizes were consistent with the TEM calculated sizes. The study also showed that from the TEM results, the iron nanoparticles synthesized in argon were larger than the particles synthesized in nitrogen, which implied that the carrier gas may have been influencing the synthesis. Similarly to Kock et al. [18], Eremin et al. [28] used both TiRe-LII and TEM analysis to study iron nanoparticles formed by the photolysis of in argon, carbon monoxide, and helium to study the effects of the carrier gas on the synthesis of the nanoparticles and how this affects the TiRe-LII results. The study showed that the TAC for the iron nanoparticles changed depending on the carrier gas used, specifically, 0.01 for helium, 0.1 for argon, and 0.2 for carbon monoxide, which supports the claim that the direct comparison of TiRe-LII measurements from different studies is difficult since each study is usually done using different experimental conditions.

An alternative method to calculate the TAC was proposed by Daun in 2009 [29] in which the TAC was calculated using molecular dynamics simulations for interactions between soot and different gases, including nitrogen, carbon monoxide, dinitrogen oxide, carbon dioxide, methane and ethane. The study also showed that the molecular dynamics derived TAC values were consistent with the experimentally derived TAC values. This work was extended to determine the nickel nanoparticle TAC values from both molecular dynamics [30] and experimental data [31] but to date, accurate results have yet to be determined.

While this study will focus on synthetic zero-valent metal nanoparticles, there have been further TiRe-LII studies on metal oxides including MgO [32], TiO_2 [33, 34], Fe_2O_3 [35], and SiO_2 [36].

1.3 Motivation of Present Work and Thesis Outline

Recently, Sipkens et al. [37] successfully carried out TiRe-LII measurements on iron nanoparticles, synthesized as a colloid and aerosolized using a pneumatic atomizer and is used as the starting point for this study. By synthesizing the iron nanoparticles in solution and then aerosolizing with the carrier gas of interest, the influence of the carrier gas on the synthesis of the nanoparticles is removed and allows the TiRe-LII measurements of different aerosol mixtures to be compared directly. Some of the key limitations of this study included: the observation of agglomeration and oxidation that occurred in solution, and subsequent uncertainty regarding how these effects influenced TiRe-LII incandescence signals, the experiments were limited to only iron nanoparticles and the effects of changing the laser fluence on the temperatures observed was not investigated. Also, the iron nanoparticles only showed that this method worked well when a sufficient amount of conduction and evaporation heat transfer is present in the system, so the versatility materials which could also use this method is currently unexplored. This is one of the key topics of investigation in this study by using silver which is expected to have heat transfer almost entirely in the evaporation regime, and molybdenum which is expected to have heat transfer predominately in the conduction regime.

The primary objectives of thesis is: to conduct TiRe-LII experiments using iron, silver, and molybdenum nanoparticles, attempt to recover the nanoparticle size and TAC for different aerosolized nanoparticle mixtures, determine the effects of changing the material properties used to interpret the TiRe-LII signals, and to conduct a nanoparticle temperature study based on the laser fluence. Specifically, this will be accomplished by building upon the experimental work of Sipkens et al. [37], starting with the reanalysis and extension of the iron nanoparticle work including a temperature and fluence study, as well as conducting the same experiments and analysis using silver and molybdenum nanoparticles. Experimental TiRe-LII measurements are performed on aerosolized iron, silver, and molybdenum nanoparticles using different carrier gases. In contrast to iron nanoparticles, silver colloids are known to be stable in solution [1] and this also expected to be the same result for molybdenum. Colloidal solutions of the respective nanoparticles are synthesized, aerosolized with a pneumatic atomizer using Ar, N_2, and CO_2 as the carrier gases, and dried by flowing the mixture through a column of silica gel desiccant prior to

TiRe-LII measurement following the same procedure carried out by Sipkens et al. [37] on iron nanoparticles. The spectral incandescence is measured at two wavelengths, and used to calculate an effective temperature. The effects of changing laser fluence and candidate radiative properties for the nanoparticles on the peak observed effective temperature are explored and how these changes affect the absorption cross-section of the nanoparticles. Then heat transfer model is used to simultaneously infer both the nanoparticle size and the TAC similarly to Sipkens et al. [37] by regressing data generated with a heat transfer model to experimental data.

Chapter 2 provides an overview of the spectroscopic and heat transfer models, and the optical and physical properties of the nanomaterials required to utilise these models. Specifically, the equations used to model the incandescence, calculate the effective temperature, as well as the heat transfer mode equations for evaporation, conduction, and radiation are presented.

Chapter 3 provides an overview of the TiRe-LII experimental apparatus required for nanoparticle size measurements, and then further details each of the specific subsystems: the TiRe-LII subsystem and the atomizer subsystem. A brief overview on the theory and principle of the *ex situ* analysis performed on the nanoparticles in this study is also provided.

Chapter 4 discusses the synthesis methods used to prepare the nanoparticle colloids for iron, silver, and molybdenum. The *ex situ* nanoparticle size and nanoparticle size distribution characterization results from electron microscopy and dynamic light scattering are discussed. Also, the TiRe-LII measurement procedure is also provided, including detailed steps on how the instruments are used and the results are recorded.

Chapter 5 presents the results of the TiRe-LII measurements, as well as the fluence and peak temperature analysis, and a comparison of the modelled spectroscopic properties to the experimentally approximated counterparts. For iron, both the TAC and nanoparticle size could be recovered due to their being sufficient evaporation and conduction, while the nanoparticle size could only be recovered for silver due there only being evaporation, and only the nanoparticle size to TAC ratio could be recovered.

Chapter 6 summarizes the conclusions of the study and then provides recommendations for future experiments. Specifically, further experiments which utilize credible optical and physical material properties should be conducted.

Chapter 2 TiRe-LII Theory and Methods

To infer the nanoparticle size and TAC, the measured incandescence signals from a TiRe-LII experiment are used to derive an instantaneous effective temperature, which can then be regressed with simulated data from a heat transfer model. From this regression, an optimal nanoparticle size and TAC pair is recovered that best reproduces the experimental data. In this chapter, the equations that are used for the interpretation of a TiRe-LII analysis are discussed. Specifically, the spectroscopic and nanoparticle cooling models, are introduced along with their governing equations. The statistical framework for recovering the nanoparticle size and TAC values is presented and lastly, the TiRe-LII instrument setup and calibration procedures are outlined.

2.1 Spectroscopic Model

The incandescence signals recorded during the TiRe-LII measurement is due to the emission from all nanoparticle size classes that are present in the aerosol. At any instant, the spectral incandescence of the laser-energized nanoparticles can be modeled by

$$J_\lambda(t) = C_\lambda \int_0^\infty P(d_p) A_c(d_p) Q_{abs,\lambda}(d_p,\lambda) I_{b,\lambda}[T_p(t,d_p)] d(d_p) \tag{1}$$

where C_λ is an instrument constant which accounts for the nanoparticle volume fraction, as well as the collection optics geometry and photoelectric efficiency of the detectors, d_p is the nanoparticle diameter, $P(d_p)$ is the nanoparticle size distribution, $A_c(d_p) = \pi d_p^2/4$ is the cross-sectional area of the nanoparticle, $Q_{abs}(d_p,\lambda)$ is the spectral absorption efficiency at the detection wavelength, $I_{b,\lambda}[(T_p(t,d_p)]$ is the blackbody intensity, and T_p is the nanoparticle temperature. Nanoparticles are expected to have diameters sufficiently smaller than the detection wavelengths, the laser wavelength, and the mean free path of the carrier gas. Consequently they emit and absorb radiation in the Rayleigh regime [38], so the absorption efficiency is

$$Q_{abs,\lambda} = 4\,\mathrm{Im}\left[\frac{\mathbf{m}_\lambda^2 - 1}{\mathbf{m}_\lambda^2 + 2}\right] x = 4E\left(\mathbf{m}_\lambda\right) x \tag{2}$$

where $\mathbf{m}_\lambda = n_\lambda + ik_\lambda$ is the complex index of refraction, $E(\mathbf{m}_\lambda)$ is the absorption function, and $x = \pi d_p/\lambda$ is the size parameter.

Eq. (1) can be rewritten as a Fredholm integral equation of the first kind following the work by Fillipov et al. [16]

$$J_\lambda(t) = \int_0^\infty P(d_p) K_\lambda(d_p, t)\, d(d_p) \tag{3}$$

where all of the terms are grouped in the kernel, $K_\lambda(d_p,t)$, excluding $P(d_p)$. The simulated incandescence values depend on the size-dependent nanoparticle cooling curves, which in turn are calculated using a nanoparticle cooling model discussed in Section 2.2. While d_p could be inferred by solving Eq. (1) using incandescence measured at a single wavelength, this procedure requires knowledge of C_λ, which is generally not known. Two-color (or auto-correlated) LII removes the dependence of C_λ [39]; this procedure utilizes the spectral incandescence measured at two wavelengths to derive an effective pyrometric temperature

$$T_p^{eff}(t) = \frac{hc_0}{k_B}\left(\frac{1}{\lambda_2} - \frac{1}{\lambda_1}\right)\left[\ln\left(\frac{J_{\lambda_1}(t)}{J_{\lambda_2}(t)}\left(K_{opt}\right)\frac{E(\mathbf{m}_{\lambda_2})}{E(\mathbf{m}_{\lambda 1})}\left(\frac{\lambda_1}{\lambda_2}\right)^6\right)\right]^{-1} \tag{4}$$

where h is Planck's constant, c_0 is the speed of light in a vacuum, k_B is the Boltzmann constant, λ_1 and λ_2 are the two detection wavelengths, $K_{opt} = C_{\lambda 1}/C_{\lambda 2}$ which the LII needs to be calibrated to account for, and $E(\mathbf{m}_{\lambda 2})/E(\mathbf{m}_{\lambda 1})$ is the ratio of the emission efficiencies at the detector wavelengths, also symbolized as $E(\mathbf{m})_r$. An example of TiRe-LII data is shown in **Fig.** 4 where the incandescence of cooling aerosolized iron nanoparticles are measured at two wavelengths and then converted to the effective temperature.

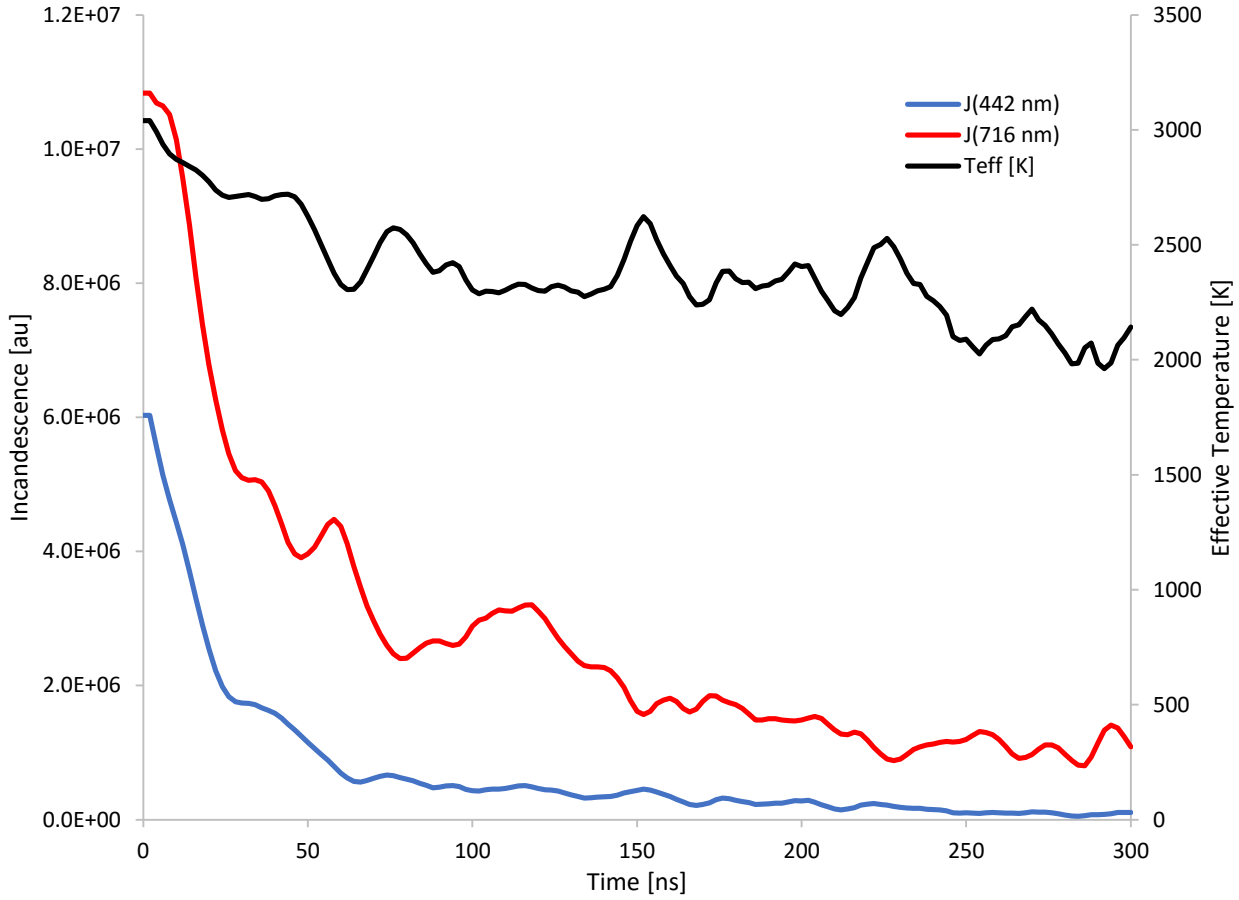

Fig. 4 Experimental iron nanoparticle incandescence and calculated effective temperature.

From Eq. (4), calculating the effective temperature requires the ratio of the emission efficiencies at the detector wavelengths, which by using Kirchhoff's law, is equivalent to the spectral absorption efficiency, defined in Eq. (2). For soot, $E(\mathbf{m}_\lambda)$ is influenced by the fuel used and the combustion environment [38, 40], while in nanoparticles of pure substances, the complex index of refraction should be a reasonable value to use for the spectral absorption efficiency. This is may not work for all materials since the optical properties of nanomaterials deviate from their bulk material properties due to the scattering of electrons [41]. Since there are limited experimental sources which attempt to quantify this for solid high temperature and molten nanoparticles, a dispersion model could be used instead to approximate $E(\mathbf{m}_\lambda)$, and is discussed in Chapter 4.

2.2 Nanoparticle Cooling Model

Modeling the incandescence during nanoparticle cooling requires knowledge of $T_p(d_p, t)$, which can be found by performing an energy balance on the energized nanoparticle as it thermally equilibrates with the

carrier gas. This energy balance sets the sensible energy equal to the nanoparticle heat transfer due to conduction, evaporation and radiation, given by

$$\rho\left(T_p\right)c_p\left(T_p\right)\frac{\pi d_p^3}{6}\frac{dT_p}{dt}=-\left[q_{cond}\left(t,d_p\right)+q_{evap}\left(t,d_p\right)+q_{rad}\left(t,d_p\right)\right] \tag{5}$$

where $\rho(T_p)$ and $c_p(T_p)$ are the temperature-dependent density and specific heat of the aerosolized nanoparticle. Although radiation is the basis for the detection method, it has been shown to have a negligible effect on the nanoparticle cooling model, when compared to the conduction and evaporation modes, and will be omitted from the analysis [18].

The nanoparticle sizes are expected to be equal to or smaller than their mean-free path within the carrier gas, so heat transfer occur in the free molecular regime. For example, Sipkens et al. [37] calculated the mean-free path molecular path of CO_2 to be approximately 40 nm, which is similar to the expected size range of the nanoparticle used in the experiments. Free molecular heat conduction is given by

$$q_{cond}(t,d_p)=\pi d_p^2 N_g^{''}\left\langle E_o-E_i\right\rangle=\pi d_p^2\frac{n_g c_{g,t}}{4}\left\langle E_o-E_i\right\rangle \tag{6}$$

where N_g'' is the incident gas number flux, $n_g = P_g/(k_B T_g)$ is the molecular number density of the carrier gas, $c_{g,t} = [8k_B T_g/(\pi m_g)]^{1/2}$ is the mean thermal speed of the carrier gas, P_g, T_g, and m_g are the carrier gas pressure, temperature, and molecular mass, respectively, and $\langle E_o - E_i \rangle$ is the average energy transfer per collision. The latter term can be rewritten using the TAC, α, which is defined as the ratio between the average energy transfer and maximum energy transfer allowed by the Second Law of Thermodynamics

$$\left\langle E_o-E_i\right\rangle=\alpha\left\langle E_o-E_i\right\rangle_{\max}=\alpha k_B\left(2+\frac{\zeta_{rot}}{2}\right)\left(T_p-T_g\right) \tag{7}$$

where ζ_{rot} is the number of rotational degrees of freedom of the carrier gas. The monatomic gases have no rotational modes available, so $\zeta_{rot} = 0$, while the linear polyatomic gases requires $\zeta_{rot} = 2$. The final form of the heat transfer due to conduction is given by

$$q_{cond}(t,d_p) = \alpha\pi d_p^2 \frac{P_g c_{g,t}}{4T_g}\left(2+\frac{\zeta_{rot}}{2}\right)\left(T_p - T_g\right) \tag{8}$$

with the appropriate value of ζ_{rot} used for the specific aerosolized nanoparticle mixture. The free molecular evaporation is given by

$$q_{evap}\left(t,d_p\right) = \Delta H_v \pi d_p^2 N_v^{''}\beta = \Delta H_v \pi d_p^2 \frac{n_v c_v}{4}\beta \tag{9}$$

where ΔH_v is the heat of vaporization of the metal atoms, N_v'' is the vapor number flux, n_v is the vapor number density, c_v is the mean thermal speed of the vapor and β is the sticking coefficient. Following Sipkens et al. [37], ΔH_v is calculated using Watson's equation [42]

$$\Delta H_v = K\left(1 - T_p / T_c\right)^{0.38} \tag{10}$$

where K is a material constant which can be found by using the nanoparticle boiling temperature and enthalpy of vaporization, and T_c is the critical temperature of the nanoparticle. Assuming that the molten nanoparticle surface and its vapor above the surface are in quasi-equilibrium, the Clausius-Clapeyron equation can be used to relate the heat of vaporization and the vapor pressure

$$\ln\left(P_{v,o}\right) = \frac{\Delta H_v}{R}\frac{1}{T_p} + C \tag{11}$$

where R is the universal gas constant, and C is a material constant. Since this pressure value corresponds to a flat interface between the two phases, this value can be further modified to account for the increased surface energy due to nanoparticle curvature using the Kelvin equation [37]

$$p_v = p_{v,o}\exp\left[\frac{4\gamma_s\left(T_p\right)}{d_p\rho\left(T_p\right)R_s T_p}\right] \tag{12}$$

where R_s is the specific gas constant, and $\gamma_s(T_p)$ is the surface tension of the nanoparticle. The heat transfer due to radiation is given by

$$q_{rad}\left(t,d_p\right)=\int_0^{\infty}\frac{\pi d_p^2}{4}Q_{abs,\lambda}\left(d_p\right)\pi I_{b,\lambda}[T_p(t,d_p),\lambda]d\lambda \tag{13}$$

where $Q_{abs}(d_p,\lambda)$ is the spectral absorption efficiency at the detection wavelength, and $I_{b,\lambda}[(T_p(t,d_p),\lambda]$ is the blackbody intensity. The spectral absorption efficiency corresponds to the incandescence calculated for a single nanoparticle size and then integrated over all wavelengths to account for the total spectral emission.

2.3 Material Properties

The material properties used for this analysis are presented for the spectroscopic and nanoparticle cooling models. For the spectroscopic model, the results of the Drude model of the optical properties are compared to the experimentally observed values reported in the literature, when possible. The nanoparticle cooling model is then used to determine the influence of the fluence on the peak temperatures for different aerosol mixtures, as well as to determine which heat transfer modes are dominant.

2.3.1 Spectroscopic Properties

It is expected that for most materials considered in this study, the energized nanoparticles will exceed their respective melting points [37], so the complex index of refraction for the molten nanoparticles should be used when calculating $E(\mathbf{m}_\lambda)$. There are only limited studies dedicated to quantifying the complex index of refraction or their equivalent complex dielectric function $\boldsymbol{\varepsilon} = \varepsilon_1 + i\varepsilon_2$ of molten metals, and this work utilizes the work previously published by Miller [43], Hodgson [44] and Krishnan et al. [45]. For some metals, it may be possible to model the complex dielectric function using Drude theory [46, 47], in which the kinetic motion of electrons are modeled as they collide with the metal's heavier and immobile positive ions. To model this, the complex dielectric components are given as

$$\varepsilon_1\left(\omega\right)=n^2-k^2=1-\frac{\omega_p^2\tau^2}{1+\omega^2\tau^2} \tag{14}$$

and

$$\varepsilon_2(\omega) = 2nk = \frac{\omega_p^2 \tau}{\omega\left(1+\omega^2\tau^2\right)} \tag{15}$$

where $\omega = 2\pi c_0/\lambda$ is the angular frequency of the E-M field, τ is the relaxation time (average time between electron-ion and electron-neutral collisions), and ω_p is the plasma frequency. The plasma frequency is given by

$$\omega_p^2 = \frac{N^{*2}e^2}{m\varepsilon_0} \tag{16}$$

where N^* is the number of free electrons per unit volume, m and e are the mass and charge of an electron, respectively, and ε_0 is the vacuum permittivity. Miller found that the effective carrier density N^* is larger than the density N of valence electrons, since the electron band structure above the Fermi level disappears upon melting [43]. The relaxation time is found from the DC conductivity,

$$\sigma_{DC} = \frac{N^* e^2 \tau}{m} \tag{17}$$

While there is interest in developing a Drude model for iron nanoparticles, a review of a previous study by Sipkens et al. [37] revealed that the Drude parameters derived by Kobatake et al. [48] was shown to be nonphysical and is not considered for this study. Instead, the experimentally derived spectroscopy properties from Krishnan et al. [45], which are consistent with the values published by Miller [43], is used in this study. The real and imaginary components of the refractive index of molten iron are shown in **Fig.** 5.

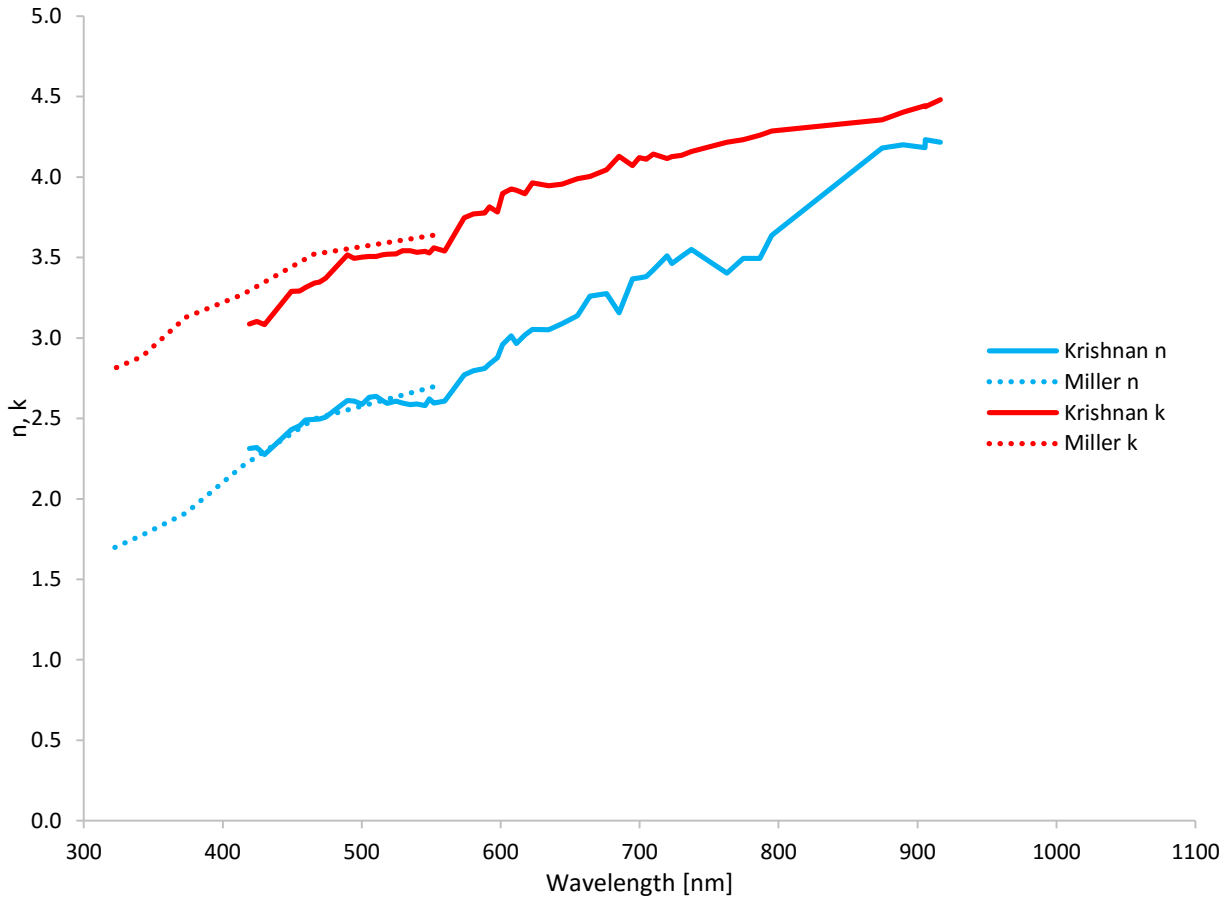

Fig. 5 Real and imaginary components of the refractive index for molten iron

The corresponding $E(\mathbf{m}_\lambda)$ values are shown in **Fig.** 6, where vertical lines denote the $E(\mathbf{m}_\lambda)$ values at the laser wavelength used (1064 nm) and the two detection wavelengths, at 442 nm and 716 nm, respectively. The experimental values from Krishnan et al. contained the required values for the detector wavelengths of the TiRe-LII system, $E(\mathbf{m}_{442\,nm}) = 0.191$ and $E(\mathbf{m}_{716\,nm}) = 0.103$ respectively, but does not include the laser wavelength, so a fourth order polynomial was fit ($r^2 = 0.9797$) to the $E(\mathbf{m}_\lambda)$ values from Krishnan et al. [45] and extrapolated to find $E(\mathbf{m}_{1064\,nm}) = 0.065$, which is also shown in **Fig.** 6.

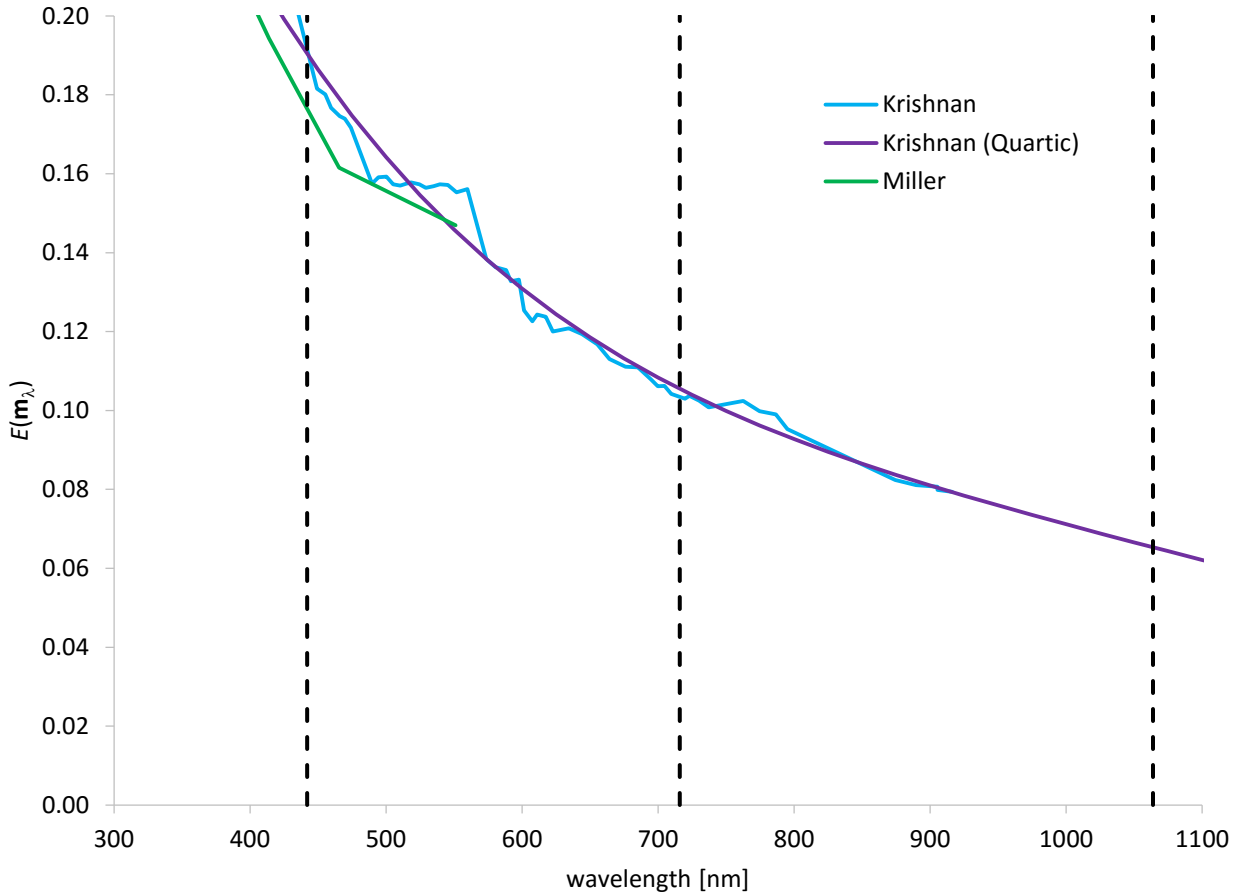

Fig. 6 $E(\mathbf{m}_\lambda)$ values molten iron

For molten silver, the DC conductivity of 58.14×10^3 $(\Omega\cdot\text{cm})^{-1}$ and $N^*/N = 1.05$ was used, following Miller [43] and Krishnan et al. [45], resulting in $\omega_p = 1.3175\times10^{15}$ rad/s and $\tau = 3.7823\times10^{-15}$ s. The real and imaginary refractive indices obtained from Drude theory are plotted in **Fig.** 7.

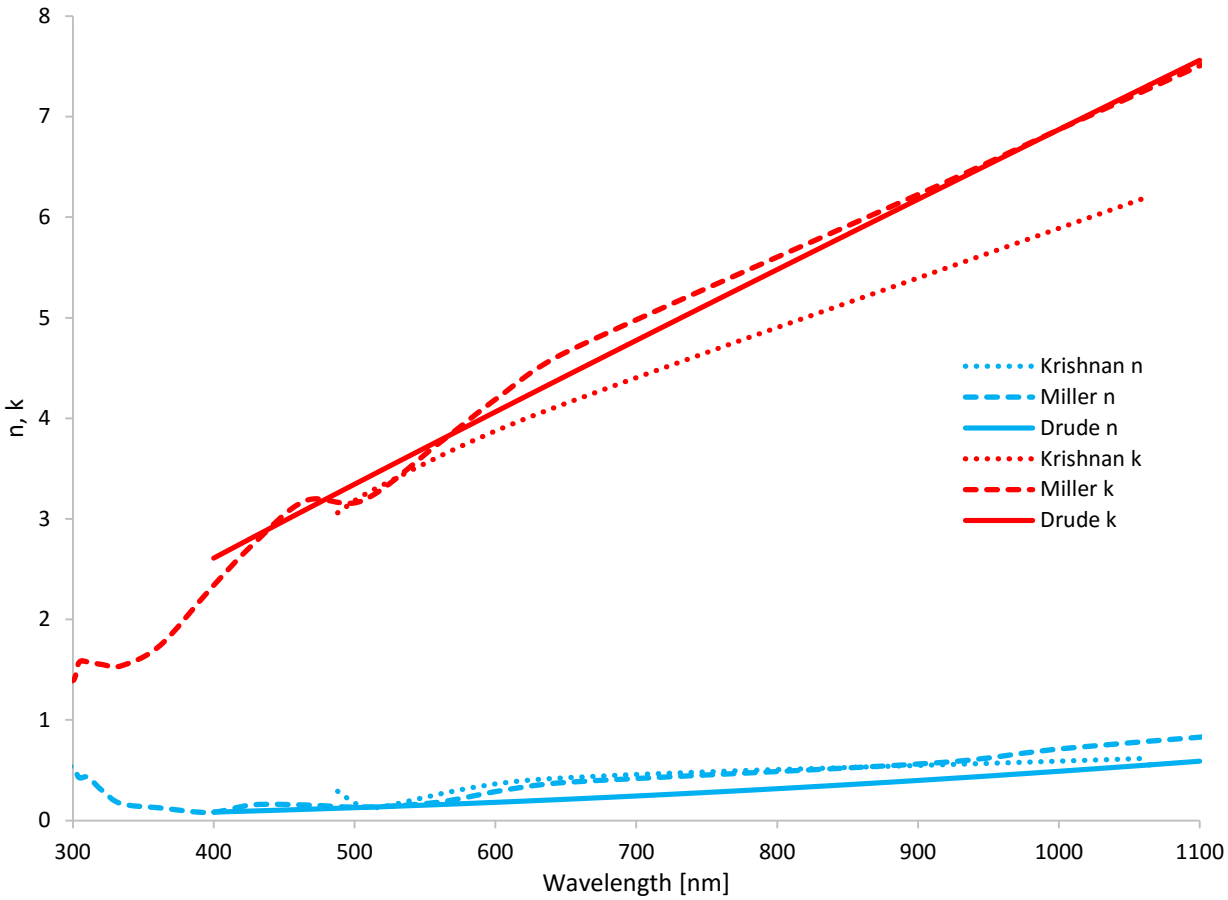

Fig. 7 Real and imaginary components of the refractive index for molten silver

The trends show good agreement with ellipsometry measurements on molten silver, which one would expect since the inter-band absorption structures present for solid metals do not exist in liquid state [43, 45, 49]. The corresponding $E(\mathbf{m}_\lambda)$ values are plotted in **Fig.** 8

Fig. 8 $E(\mathbf{m}_\lambda)$ values molten silver

. For this study the Drude derived $E(\mathbf{m}_\lambda)$ values were selected to interpret the molten silver TiRe-LII data, specifically, $E(\mathbf{m}_{442\,nm}) = 0.041$ and $E(\mathbf{m}_{716\,nm}) = 0.015$ and $E(\mathbf{m}_{1064\,nm}) = 0.009$.

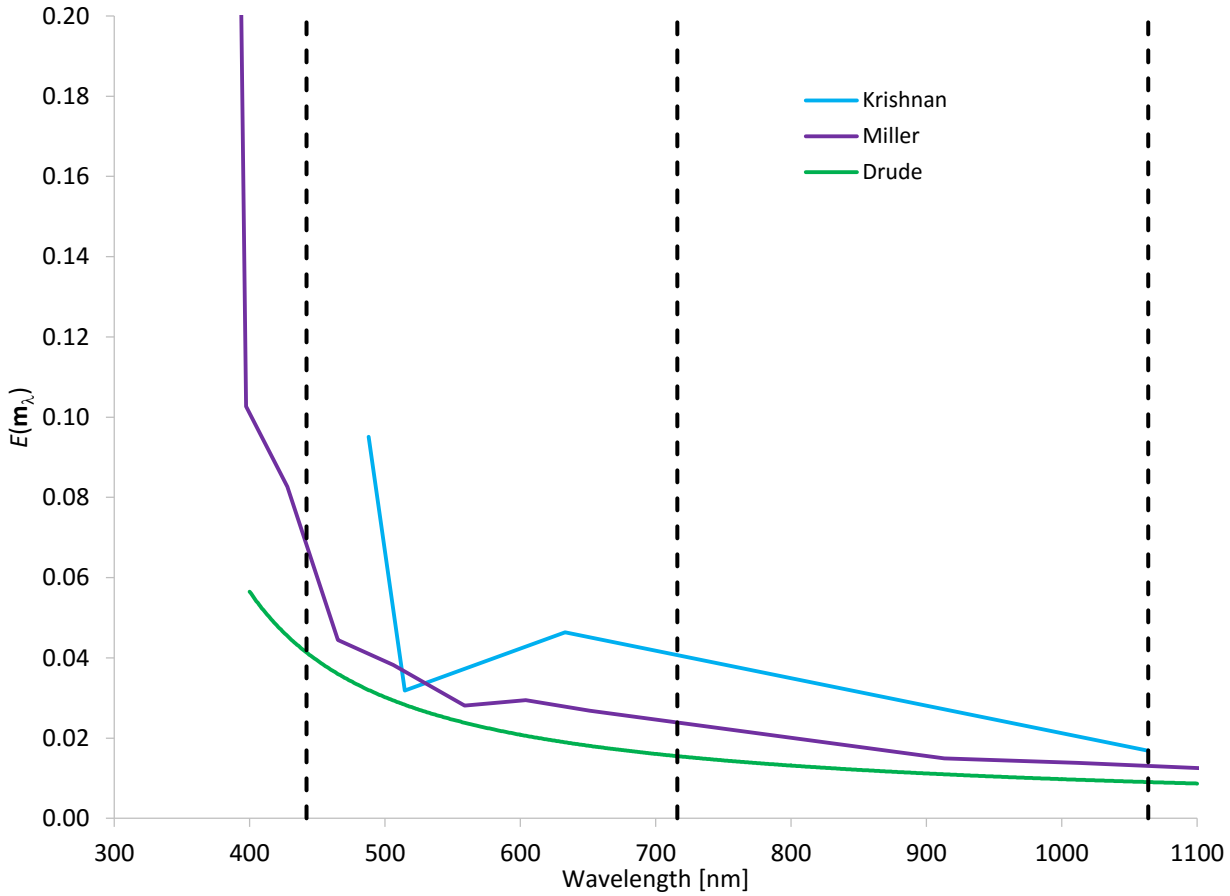

Fig. 8 $E(\mathbf{m}_\lambda)$ values molten silver

From preliminary trials it was observed that the TiRe-LII experiments on molybdenum nanoparticles do not exceed its melting temperature (2896 K [50]), so high temperature solid state values for the index of refraction were investigated. This is because the n_λ, k_λ and $E(\mathbf{m}_\lambda)$ values depend on the DC conductivity of the material which is directly influenced by the temperature through Drude/Hagen-Rubens theory [38]. Experimental refractive index values were taken from Barnes on solid molybdenum at 2000 K [51], Juenker et al. at 2200 K [52], and Palik et al. at 300 K [53] and are plotted in **Fig.** 9 with the corresponding $E(\mathbf{m}_\lambda)$ values plotted in **Fig.** 10. For this study the experimental $E(\mathbf{m}_\lambda)$ values from Barnes [51] were selected to interpret the molybdenum TiRe-LII data, specifically, $E(\mathbf{m}_{442\,nm}) = 0.151$ and $E(\mathbf{m}_{716\,nm}) = 0.097$ and $E(\mathbf{m}_{1064\,nm}) = 0.065$.

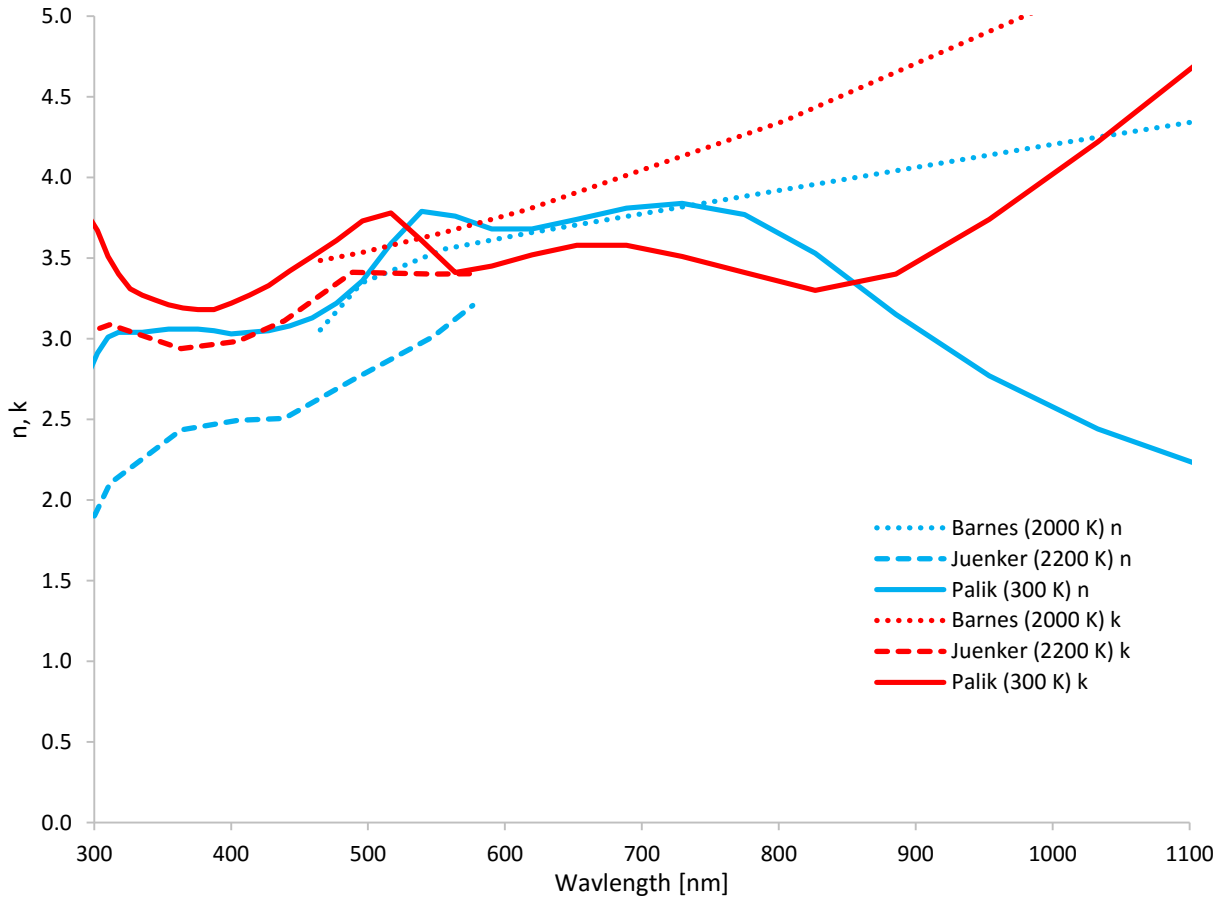

Fig. 9 Real and imaginary components of the refractive index for molybdenum

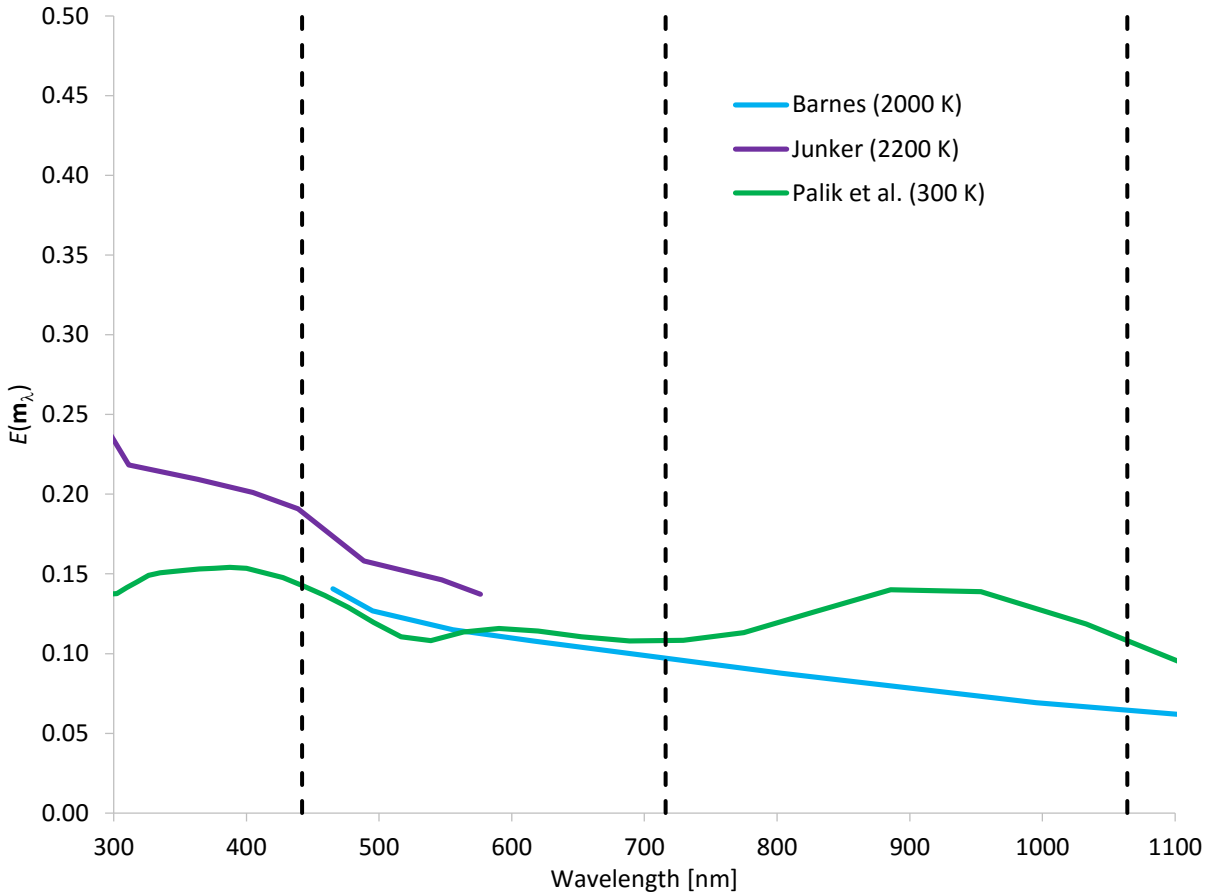

Fig. 10 $E(\mathbf{m}_\lambda)$ values for molybdenum at different temperatures

2.3.2 Nanoparticle Cooling Properties

To solve the nanoparticle cooling model outlined in section 2.2, the literature was surveyed for the molten temperature dependent properties for iron and silver, and high temperature solid state values for molybdenum. From preliminary tests, the peak TiRe-LII derived temperature of molybdenum nanoparticles approaches but never exceeds its melting point, 2896 K [50], so it follows that high temperature solid state values . Temperature dependent values could not be found for all the material properties, such as the surface tension for molybdenum, and the next reasonable value found in the literature were used. All of the values selected are summarized in

Table 1.

Table 1 Nanoparticle Cooling Properties

Property	Fe	Ag	Mo
m_g [kg/mol]	0.05585	0.1080	0.9594
ρ [kg/m^3]	8171-0.64985·T_p [54]	9346-0.9067·(T_p-1234) [55]	9100-0.6·(T_p-T_m), T_p>=T_m 9100-0.5·(T_p-T_m), T_p<T_m [50]
c_p [J/(kg·K)]	835 [56]	531 [57]	56.5+0.01177·(T_p-T_m), T_p>=T_m a(T_p)[a], T_p<T_m [50]
T_m [K]	1811 [56]	1234 [55]	2896 [50]
T_b [K]	3134 [58]	2466 [59]	4913 [60]
T_{cr} [K]	9340 [61]	6410 [55]	14,588 [61]
ΔH_v [J/mol]	340·(10^3) [58]	254·(10^3) [59]	582·(10^3) [62]
γ_s [N/m]	1.865-(T_p-1823)·(0.35)·(10^{-3}) [63]	1.0994-0.0002·T_p [64]	2.11 [65]

[a] a(Tp) = (1582+0.0589·(T_p-T_m))·(3.0+1.03·(10-3)·(T_p-T_m))

Using the physical properties listed in **Table** 1, Eq. (5) can be used to simulate nanoparticle cooling data can be calculated and then used to approximate what kind of heat transfer modes should be dominant as well as how we could modify our heat transfer model when using it to regress experimental data to reduce our computational effort. Hypothetical 50 nm and 0.1 TAC iron, silver and molybdenum nanoparticles were used to calculate the contribution of the conduction, evaporation and radiation heat transfer modes between the expected TiRe-LII experiment temperature range of 1500 K to 3000 K, shown in **Fig.** 11, **Fig.** 12, and **Fig.** 13 for iron, silver and molybdenum respectively.

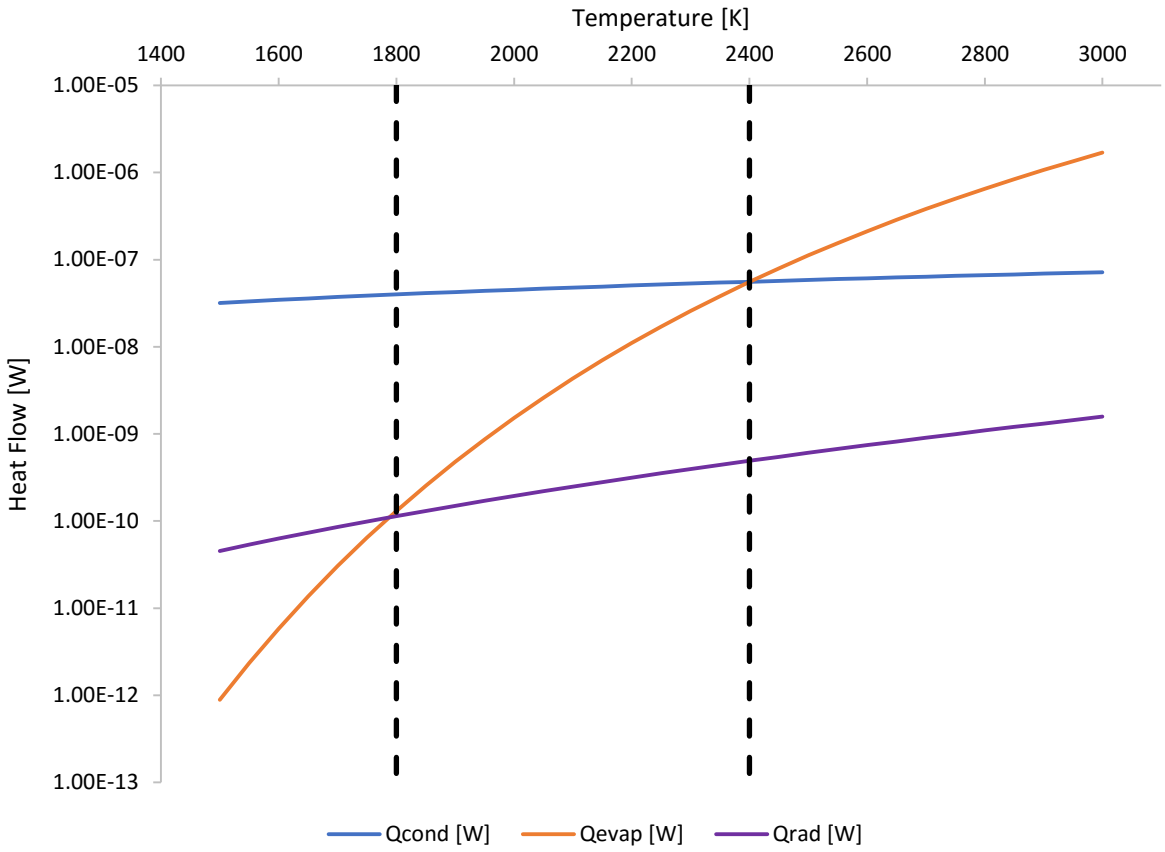

Fig. 11 Heat transfer modes for a simulated iron nanoparticle

From **Fig.** 11, it can be seen that there are primarily two regions of heat transfer for iron nanoparticles, the evaporation regime which occurs over 2400 K, and the conduction regime which occurs below 2400 K. it can also be seen that in both regimes, radiation is orders of magnitude below the dominant heat transfer mode which supports the simplifying assumption of removing it during the calculations, although radiation is more significant than evaporation below 1800 K. Also taking into account the previous work done by Sipkens et al. [37] iron nanoparticles have a temperature range of approximately 3000 K to 2200 K, signifying that there should be sufficient amounts of both evaporation and conduction over the duration of a TiRe-LII experiment so both the particle size and TAC can be recovered simultaneously.

The simulated silver heat transfer modes in **Fig.** 12 shows that there are two regimes dominated by evaporation and conduction where the transition temperature is approximately 1900 K. From preliminary tests as well as from Fillipov et al. [16], a typical TiRe-LII experiment on silver nanoparticles

has a very short period of incandescence, approximately less than 100 ns which results in an approximate temperature range from 2800 K to 2200 K. From these two observations, the assumption that TiRe-LII experiments for silver predominantly occur in the evaporation only regime is supported so only the nanoparticle size can be recovered since the evaporation model is not dependent on the TAC, which is only required in the conduction model.

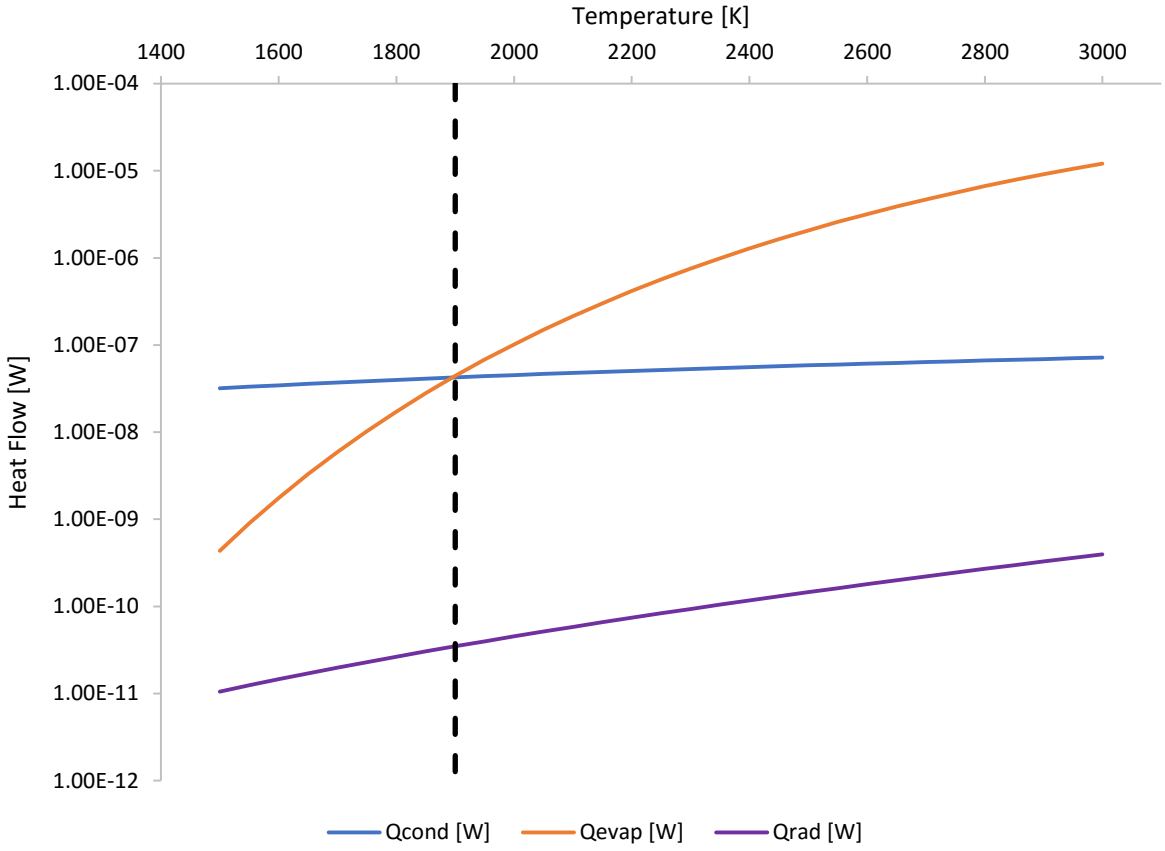

Fig. 12 Heat transfer modes for a simulated silver nanoparticle

Lastly, the simulated molybdenum data in **Fig.** 13 clearly shows that the dominant heat transfer mode for the entire TiRe-LII experiment range is conduction. This is consistent with previous studies work done by Murakami et al. [19] and Sipkens et al. [20] where only the nanoparticle size and TAC ratio could be determined due to molybdenum since Eq. (9) can be rewritten as,

$$\rho\left(T_p\right)c_p\left(T_p\right)\frac{\pi d_p^3}{6}\frac{dT_p}{dt}=-q_{cond}\left(t,d_p\right)=-\alpha\pi d_p^2\frac{P_g c_{g,t}}{4T_g}\left(2+\frac{\zeta_{rot}}{2}\right)\left(T_p-T_g\right) \tag{18}$$

which can be rearranged to

$$\frac{dT_p}{dt} = -\frac{\alpha}{d_p}\frac{3P_g c_{g,t}}{2\rho c_p T_g}\left(2+\frac{\zeta_{rot}}{2}\right)\left(T_p - T_g\right) \tag{19}$$

where the solution of Eq. (19) will always have depend on the nanoparticle size to TAC ratio. By assuming a weak temperature dependence for the density and specific heat capacity, integrating Eq. (19) and plotting $\ln(T_p-T_g)$ against time, allows the nanoparticle size and TAC ratio could be approximated as a fixed ratio from the slope. A more accurate method to recover the TAC, the nanoparticle size is determined through an *ex situ* method and then fed into the model to find the optimal TAC value during regression. In this work, the molybdenum particle size and size distribution was determined through TEM image analysis which can then be used to determine the TAC value through the model regression.

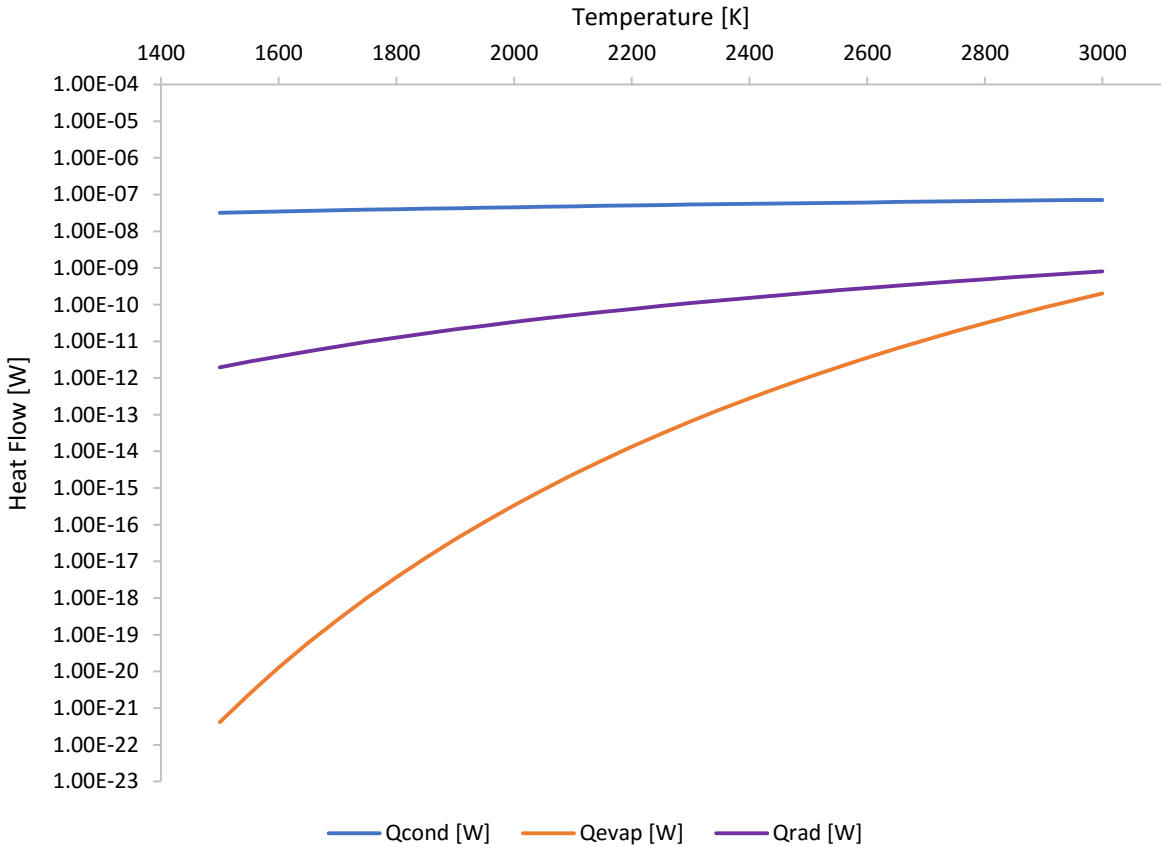

Fig. 13 Heat transfer modes for a simulated molybdenum nanoparticle

2.3 Nanoparticle Size and TAC Inference, and Uncertainty Quantification

The nanoparticle size and TAC values are inferred by regressing experimental effective temperatures with simulated data generated with the heat transfer model described in previous section. If the aerosolized nanoparticles are monodisperse (i.e. uniformly-sized), the parameters of interest, d_p and the TAC, can be inferred using Bayesian analysis following Sipkens et al. [66]. The posterior probability density, $P(\mathbf{x}|\mathbf{b})$, is found from Bayes' equation

$$P(\mathbf{x}\,|\,\mathbf{b}) = \frac{P(\mathbf{b}\,|\,\mathbf{x}) \times P_{pr}(\mathbf{x})}{P(\mathbf{b})} \tag{20}$$

where $\mathbf{x} = [d_p,\ \alpha]^\mathsf{T}$, $\mathbf{b}$ contains the effective temperatures, $P(\mathbf{b}|\mathbf{x})$ is the likelihood of $\mathbf{b}$ occurring for candidate values of $\mathbf{x}$, $P_{pr}(\mathbf{x})$ is the prior probability, and $P(\mathbf{b})$ is the evidence, which scales the posterior probability so that it satisfies the Law of Total Probability. This study uses an uninformed prior, $P_{pr}(\mathbf{x}) = 1$, and assumes that the effective temperatures are contaminated with normally-distributed measurement noise which results in the determination of the maximum likelihood estimator (MLE). While not explicitly defined as a prior, two physical restraints are placed on the results from this framework: the first being that the nanoparticle size must be greater than 0 nm since the nanoparticles exist; and the TAC is bound by a range of 0 to 1 since it corresponds to an energy transfer efficiency. Additionally, the minimization is conducted using MATLAB's built-in fminsearch function which utilizes a Nelder-Mead minimization algorithm unlike Sipkens et al. [37] who utilize MATLAB's built-in nonlinear least squares regression function, using the Levenberg-Marquardt algorithm. Under these conditions the likelihood function is proportional to

$$-\ln\left[P(\mathbf{b}\,|\,\mathbf{x})\right] \propto \sum_{j=1}^{N} \frac{\left[\mathbf{b}_{eff,j}^{exp} - \mathbf{b}_{eff,j}^{model}(\mathbf{x})\right]^2}{\sigma_j^2} \tag{21}$$

where σ_j^2 is the variance of the j^{th} temperature measurement; the incandescence signals are collected from 500 laser pulses, and observed noise is reduced by multishot averaging and also gives the variance of the measurements. An advantage to using a Bayesian statistical framework is it also allows the quantification of the error bounds for d_p and α, by marginalizing the posterior probability density following

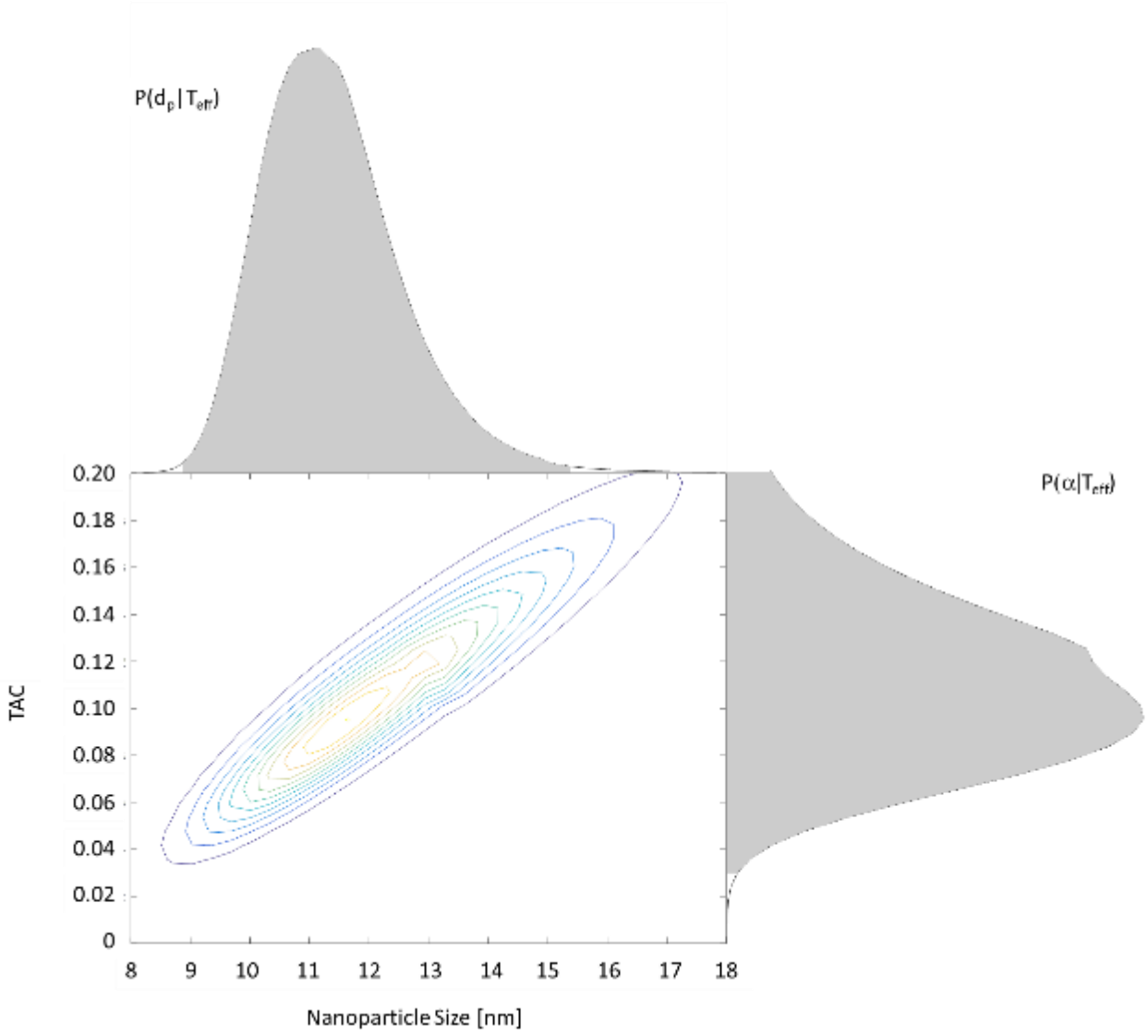

Fig. 14 Marginalization plot for a Fe-Ar aerosol

Sipkens et al. [66], and an example of this is shown in **Fig.** 14, where the respective 95% error bounds are shown as the filled in grey areas.

In addition to the quantification of the error bounds, there is an additional uncertainty assigned to each of the nanoparticles' physical properties as well as the operating conditions of the TiRe-LII instrument which cannot easily be quantified. For this study, a perturbation analysis is performed for some of the key physical parameters to determine the change, if any, from the recovered MLE solution.

Chapter 3 Experimental Apparatus

The TiRe-LII experimental apparatus is divided into two main subsystems: the TSI atomizer, which is responsible for aerosolizing and drying the nanoparticles; and TiRe-LII instrument itself to laser heat the nanoparticles and measure the incandescence. In this chapter, the operational parameters used in this study are introduced for both subsystems. Furthermore, *ex situ* characterization techniques which were used in conjunction with these subsystems, as they provide particle size measurements which can then be compared to the TiRe-LII measurements, are also introduced and the discussed.

3.1 TiRe-LII Experimental Overview

This work uses an identical TiRe-LII experimental setup to Sipkens et al. [37] and a general schematic is shown in entire process is depicted in **Fig.** 15, where the grey clusters represent the nanoparticles, the blue clusters represent water molecules, the solid blue dots represent the carrier gas, and the grey lines represent any residual materials from the synthesis procedure, including dispersants and trace contaminants. In the case of the iron nanoparticles, a polymer layer is applied to the surface to prevent the nanoparticles from oxidation and agglomeration which is assumed to be ablated during the laser heating process, depicted as the grey lines being removed in the schematic in **Fig.** 15. The silver nanoparticles use an aqueous dispersant to prevent nanoparticle agglomeration, which is removed during the aerosol drying, while the molybdenum nanoparticles are not prepared with any dispersant.

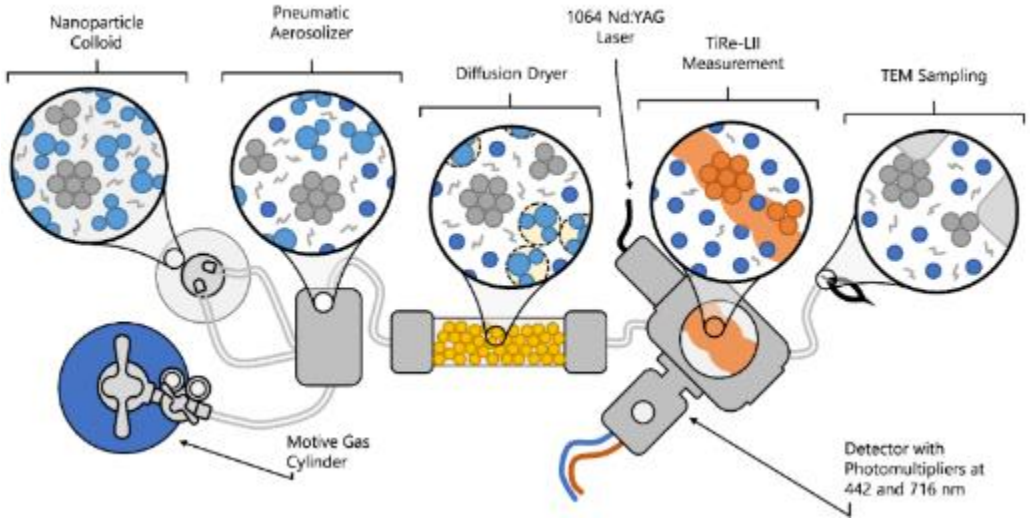

Fig. 15 Schematic of the TiRe-LII experimental apparatus [37].

The TiRe-LII instrument is set up to allow an aerosolized mixture flow through the sample chamber and then ventilated in a fume hood. When in operation, the system is completely closed which minimizes the likelihood of the experimental area being exposed to nanoparticles. After the nanoparticles of interest are made into a colloid, different aerosol mixtures are generated using a TSI Model 3076 pneumatic atomizer operating in recirculation mode using the carrier gas of interest, at an inlet pressure of approximately 200 kPa. This produces a stream of water droplets approximately 350 nm in diameter which contains the nanoparticle of interest, any residual byproducts from the nanoparticle synthesis, and a dispersing agent to prevent the nanoparticles from aggregating depending on the nanomaterial being tested.

After aerosolization, the wet aerosol pass through a diffusion drier charged with a silica gel desiccant, which removes any moisture from the aerosol. Since the residual byproducts and the dispersing agents remain in liquid, they are also removed by the silica gel. The dried aerosol then reaches the TiRe-LII sample chamber where the laser pulse heating occurs, and the incandescence is recorded as the nanoparticles are allowed to thermally equilibrate with the carrier gas. The aerosolized nanoparticles enter the sample chamber where the aerosol pressure is measured at 101.3 kPa ± 3.5 kPa using an Omega PX409-USBH pressure transducer for the duration of a TiRe-LII experiment shown in **Fig.** 16, and is at room temperature. From the schematic, the setup allows for an easy change of the motive gas which allows a variety of different aerosol mixtures to be tested. While Sipkens et al. [37] previously utilized He, Ar, Ne, CO, N_2, CO_2, and N_2O for their TiRe-LII study on iron nanoparticles, this study limits the carrier gases to be Ar, N_2 and CO_2.

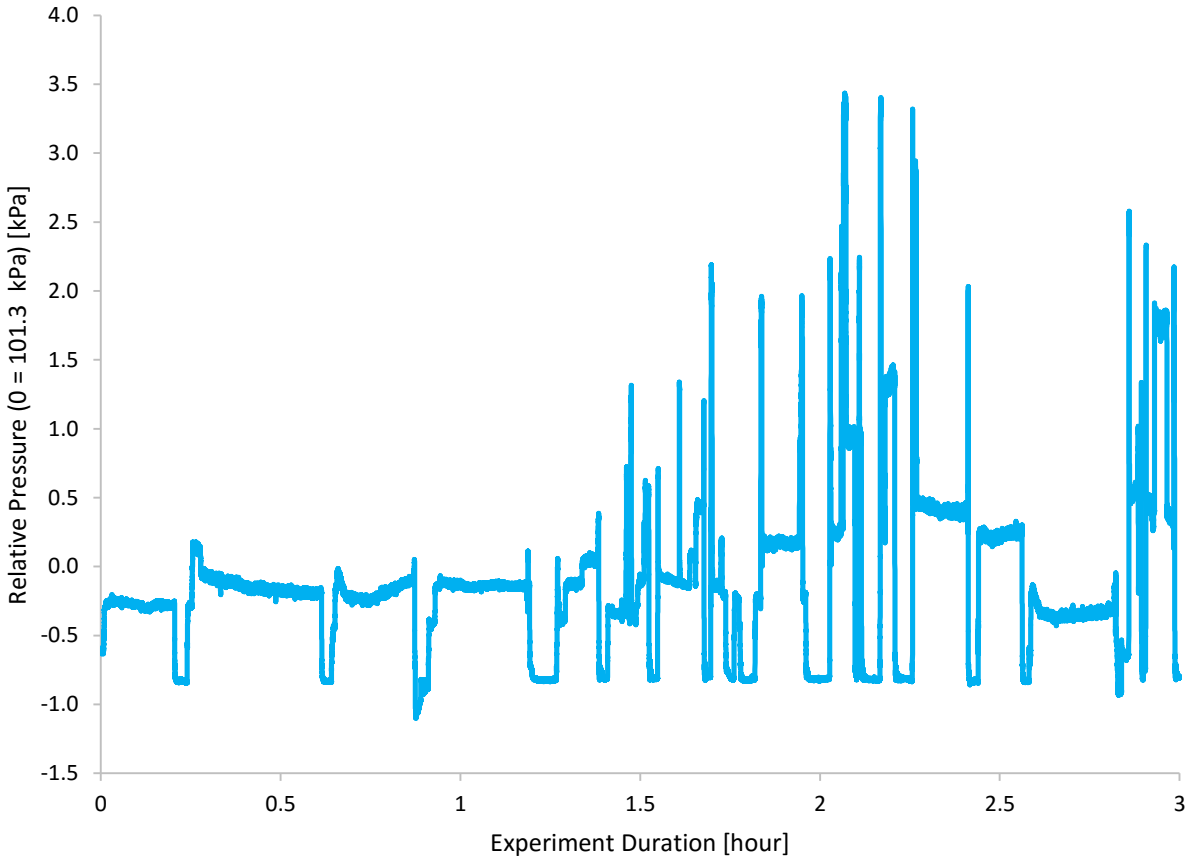

Fig. 16 Relative pressure changes during a TiRe-LII Experiment

3.2 TiRe-LII Subsystem

The TiRe-LII experiment is carried out using an Artium 200 M system and was calibrated before this study, under the supervision of Mr. Robert Sawchuk at the National Research Council of Canada. The nanoparticles are energized using a 1064 nm Nd:YAG laser operating at 10 Hz. The nominal laser fluence is 0.2630 J/cm^2 and could be adjusted by altering the flashlamp Q-switch delay with the nominal Q-switch value being 137 µs. After the laser pulse, the energized particles thermally equilibrate with the carrier gas and the spectral incandescence emitted during this cooling stage is measured using two photomultipliers (PMTs) equipped with bandpass filters centered at 442 nm and 716 nm (full width at half maximum of 50 nm), sampled every 2 ns, and for 500 laser pulses for each test.

To calibrate the TiRe-LII, first the laser was aligned such that it was following the appropriate path through the sample chamber. This was accomplished by replacing the sample chamber with flashpaper at the appropriate location of the target nanoparticles in the sample chamber, and then pulsing and readjusting the position of the laser source until the beam path was correct. After the laser was aligned, the laser beam was profiled using a Coherent USB LaserCam HR Head, to ensure that appropriate top-hat beam distribution was observed when the ceramic aperture and relay lens are used [39]. The beam profiler was placed at the same location of the flashpaper during the laser beam alignment and the laser was repeatedly pulsed until the laser distribution was successfully profiled. The results of the beam profiling before and after the addition of the ceramic aperture and relay lens are shown in **Fig.** 17. The first profiling was done on the direct laser beam, **Fig.** 17a, which was circular with the highest intensity at the centre of the beam as expected, then the ceramic aperture and relay lens was introduced into the beam path and profiling showed the expected top hat distribution with a more consistent intensity profile, **Fig.** 17b.

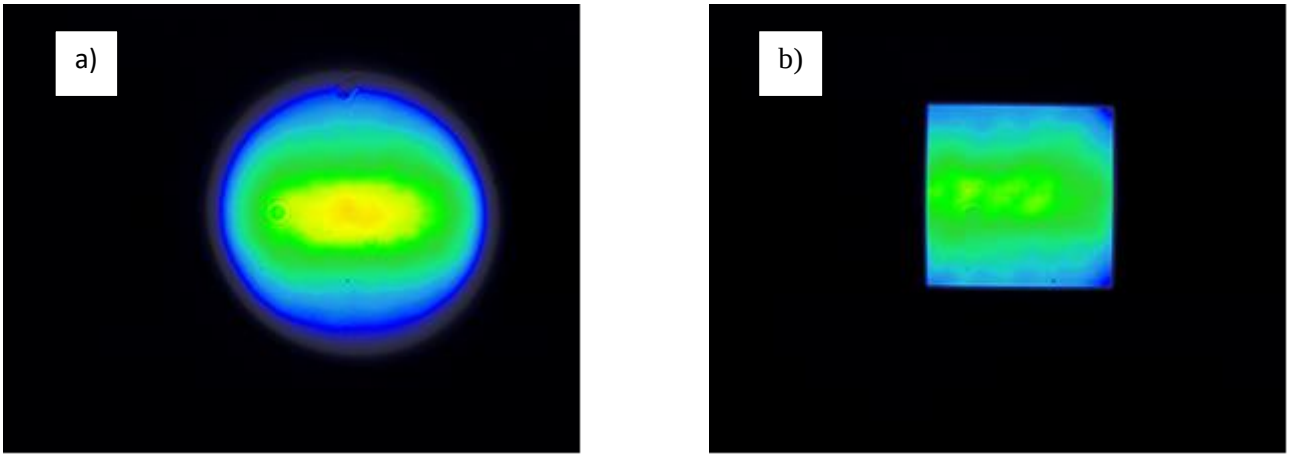

Fig. 17 Beam profile results of a) the direct laser beam, and b) the laser beam passing through the ceramic aperture and relay lens.

The laser energy per pulse the aerosolized nanoparticles are exposed to in the sample chamber was measured using a pyroelectric sensor (Coherent® J-25MB-IR). The sample chamber contains three sapphire glass windows (ESCO Optics, G110040 Sapphire Circular Windows), where two of them are responsible for decreasing the energy of the laser pulse prior to termination. The most significant decrease occurs as the laser pulse passes through the first window which is placed between the ceramic aperture and relay lens system and the probe area within the sample chamber. The second window is placed between the sample chamber and a laser beam trap which terminates the incident laser pulse, and the third window is placed between the sample chamber and the PMTs, neither contributing to any energy loss prior to the laser beam interacting with the aerosolize nanoparticles. To accurately reproduce the same conditions effect that the glass window has on the interaction between the laser beam and the aerosolized nanoparticles, one window is inserted between the ceramic aperture and relay lens system and the pyroelectric sensor, shown in **Fig.** 18.

The flashlamp input energy was set to 3.3 J and the laser output energy was controlled by changing the flashlamp's Q-switch delay value between 137 µs and 190 µs. For specific Q-switch values, the laser was pulsed 100 times, allowing the calculation of the average output laser energy and the respective standard deviation. The results of these measurements are summarized in **Table** 2. By measuring the laser pulse interaction area with the flashpaper used during the calibration the probe area

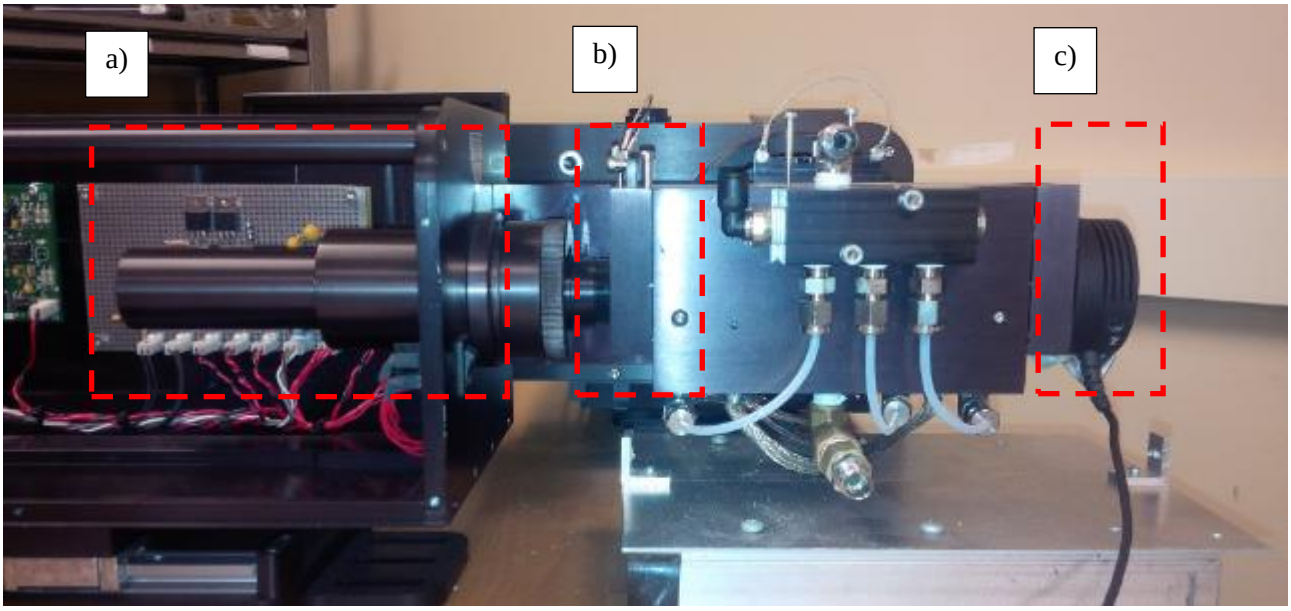

Fig. 18 TiRe-LII Apparatus showing a) aperture and lens system, b) window 1, c) pyroelectric sensor

in the sample chamber determined to be 2.5 mm × 2.5 mm, which allows the calculation of the laser fluence, reported in J/cm^2 and this value is also included in **Table** 2.

Table 2 Laser Energy Measurements

Q-Switch Delay [µs]	<Laser Energy> [mJ]	Standard Deviation [mJ]	Fluence [J/cm^2]
137	16.57	0.13	0.2630
150	16.54	0.09	0.2625
160	16.04	0.08	0.2546
170	15.20	0.09	0.2413
175	14.69	0.10	0.2332
180	14.16	0.06	0.2248
185	13.59	0.09	0.2157
190	12.95	0.07	0.2056

The detection apparatus is shown in **Fig.** 19, highlighting the aperture wheel, density filter wheel and the beam splitters and PMT. The factor calibration settings were used for the detectors and no

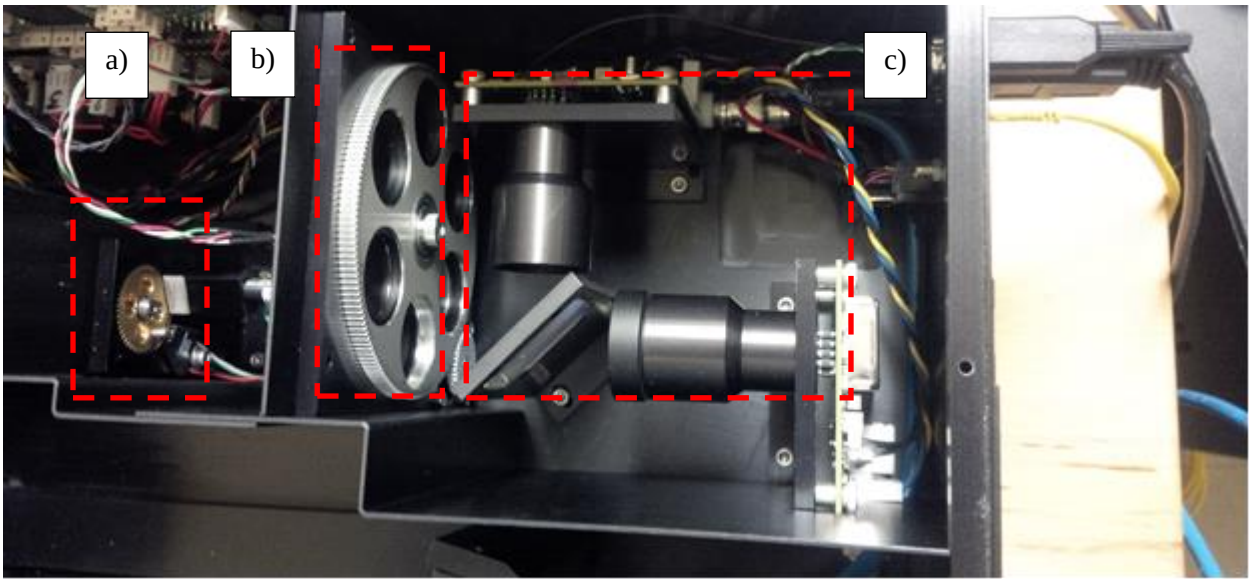

Fig. 19 TiRe-LII Apparatus showing a) collection aperture wheel, b) density filter wheel, c) beam splitter and the wavelength specific PMTs

attempts were made to perform any in-house calibration; these calibrations involved using a calibrated light source which was used to calibrate the response observed at the PMTs. In this setup, a collection aperture of 5 mm with no neutral density filter was used. Previous experimental work with this setup had shown that there was an adequate signal being measured for iron nanoparticles.

3.3 TSI Atomizer Subsystem

For this study, a TSI 3076 pneumatic atomizer operating in recirculation mode was selected for generating the aerosolized nanoparticle stream from a colloid. The nanoparticle colloid is contained in a bottle with a modified cap fitting which is attached to the atomizer assembly block via two tubes, one tube which the colloid is drawn into the assembly block and aerosolized and the other is to allow any excess liquid in the assembly block to return to the stock colloid. A picture of the system aerosolizing an iron nanocolloid, is shown in **Fig.** 20.

A pressurized carrier gas of interest source (200 kPa, controlled using the motive gas cylinder regulator) is connected to the inlet of the atomizer assembly block where it forms a high velocity jet which draws up the colloid due the Venturi effect. The liquid is atomized by the jet where the smaller nanoparticle droplets are exhausted through the top of the atomizer and larger droplets which strike the back wall of the atomizer and is drained back into the stock colloid bottle. According the manufacturer's

Fig. 20 TSI atomizer subsystem, aerosolizing an iron nanocolloid

specifications, the number mean droplet diameter of the exhaust aerosolized nanoparticle stream is 350 nm for water based colloids. From this, the approximate nanoparticle per droplet concentration can be determined, if the effects of dilution on the nanoparticle colloids is investigated in the future work.

After the aerosolized nanoparticles leave the atomizer assembly block, the nanoparticles are still contained within water which may be contaminated with leftover reactants, dispersants or other trace materials. Since the TiRe-LII cannot differentiate between the different sources responsible for the incandescence being detected, these contaminants need to be removed. The aerosolized nanoparticles are forced through a diffusion drier charged with an indicator based silica gel beads desiccant, which changes colour from orange to white as the beads absorb moisture. This provides a visual indicator that the aerosol is being dried, which is expected to draw out most of the water based contaminants. After drying, the aerosolized nanoparticles enter the TiRe-LII sample chamber for measurements.

3.4 *Ex Situ* Characterization

Dynamic light scattering is a colloidal characterization technique which allows the hydrodynamic particle size of a material to be inferred while in solution. It is a non-destructive light scattering technique which operates on the basis that the particles undergo Brownian (or thermal) motion which can be used to infer the diffusion coefficient of the particles and then calculate the particle size. Under dilute conditions, particles are free to diffuse throughout the solution based on the thermal energy of the system with the energy losses caused by the viscosity of the solvent. Smaller particles are expected to have a larger diffusion coefficient while larger particles are expected to have a smaller diffusion coefficient due to differences in the viscous losses as the particles move through the solvent. During DLS characterization, a stationary laser at a fixed angle with respect to the probe area and the detector is fired into the colloid and the scattering intensity is recorded. Qualitatively, since larger particles would have a smaller diffusion coefficient, the scattering profile is relatively consistent throughout the experimental duration while smaller particles move quicker, the scattering profile is expected to change rapidly. The dynamic laser intensity measurements can then be used to determine the autocorrelation function which quantifies the change of the laser intensity over time. While the calculation and derivation of the autocorrelation function is outside the scope of this work, it can then be used to calculate the translational diffusion coefficient and since the colloid is undergoing Brownian motion, the particle size can now be determined by rearranging the Stokes-Einstein equation

$$d_p = \frac{k_b T}{3\pi D} \tag{22}$$

where T is the temperature of the colloid, and *D* is the auto correlated calculated diffusion coefficient. The particle size is inferred from the diffusion coefficient which sets an empirical concentration limit for colloid characterization since the particles are required to be free from the influence of the other particles in the solution to determine the appropriate diffusion coefficient. Under moderate to high concentrations, since the particles now in a closer proximity to each other and effectively hindering the overall mobility of the particles, this is expected to decrease the overall laser intensity fluctuations and result in smaller values for the diffusion coefficient which results in a larger particle size. A 1:1000 colloid to solution (colloid + solvent) volume ratio was selected as a sufficient concentration for this study, while ideally for a robust DLS analysis, serial dilutions of the colloid and the extrapolation to an infinitely diluted colloid provides a more accurate analysis of the system and could be done in future experiments. It is important to highlight that DLS treats surface modified samples, such as the iron nanoparticles used in this study, as a single particle and cannot differentiate between the nanoparticle core and the surface coating. This artificially increases the DLS measured sizes for iron and provides more of an upper bound on what we could expect the nanoparticle size to be. A more compressive discussion of dynamic light scattering, including the mathematical models and colloidal chemistry can be found in Hiemenz and Rajagopalan [67].

Scanning electron microscopy and transmission electron microscopy are non-destructive imaging techniques which operate by probing a sample of interest with an electron beam. While they both probe the sample with an electron beam, their detection principles differ in that SEM looks at the intensity of electrons produced from the sample's surface while TEM looks at the scattering profile as electrons pass through the sample. In SEM, the sample ejects electrons (secondary electrons) as it is bombarded by the high energy electron beam (primary electrons) and the image is formed based on the relative amount of secondary electrons being emitted from the different surface features of the sample. Alternatively, TEM imaging operates on the principle of generating an image based on the electron scattering pattern as a high energy electron beam passes through it. The key requirement for TEM characterization is that the sample is sufficiently thin enough to allow a high energy electron to pass through it. An advantage to using these microscopy techniques is that they also allow for compositional analysis known as energy-dispersive X-ray spectroscopy (EDX), due to the emission of x-rays generated when core electrons are ejected from

Fig. 21 Preparation of the TEM grids

the material and a higher valance electron fills their void, releasing the difference in energy in the form of an x-ray. These electron transitions are well known for the elements and can provide information about the presence of contaminants in the sample and their relative portions. A more compressive discussion of electron microscopy characterization can be found in Leng [68]. Since there was no quantitative information on the expected size range of the iron and molybdenum nanoparticles, so TEM analysis was selected over SEM as it provided a much higher resolution, if it was required for small nanoparticle sizes. Since there was some prior knowledge of the expected size ranges of the silver nanoparticles and high resolution SEM had worked previously, SEM was used for this study. A main drawback to using TEM analysis is during the sample grid preparation; when a sample of the nanocolloid is placed onto the sample grid, there still may be some settling and agglomeration occurring while the sample dries as shown in **Fig.** 21, as the grids are being dried under a laboratory lamp. Also, there is usually a long period of time between the sample preparation and the imaging which may result in a larger nanoparticle size being measured due to oxidation of the nanoparticles as well.

For this work, a Malvern Instruments Zetasizer Nano-ZS90 instrument was used to conduct DLS measurements on the iron nanoparticles while a Vasco DL 135 instrument equipped with a 657 nm Nd:YAG laser, using a Padé-Laplace method was used to interpret the DLS data for the silver and molybdenum nanoparticles (the associated error for this instrument is ±5% of the measured value). For electron microscopy, a LEO 1550 instrument was used for the SEM analysis using the standard double sided carbon tape as the sample adhesive, and a JEOL 2010F instrument was used for the TEM analysis using 200-mesh copper TEM grids as the sample holders. The imageJ software package to quantify the nanoparticle size distribution statistics for both the SEM and TEM images.

Chapter 4 Experimental Procedure

Previous TiRe-LII experiments have relied on synthesizing nanoparticles *in situ* prior to laser heating, and included using a plasma reactor [66] and photolysis [19, 20] methods. These methods have the drawback of the carrier gas of interest interacting with the synthesis process and may result in different nanoparticle sizes for different aerosol mixtures [20]. In this work, the nanoparticle of interest is prepared as a colloid and then aerosolized using a pneumatic atomizer, so that the synthesis of the nanoparticles used in TiRe-LII experiments are independent of the aerosol gas used. This method also has the advantage of using traditional colloidal characterization techniques which allow the determination of the nanoparticle sizes which can later be compared to the TiRe-LII derived nanoparticle size. In this chapter, the preparation steps for all of the nanoparticle colloids used in this study are outlined, including their synthesis procedures, and associated *ex situ* characterization.

4.1 Nanoparticle Preparation

Immediately before a TiRe-LII experiment is conducted, the metallic zero valent nanoparticles were prepared in solution to minimize the effects of agglomeration and oxidation. In these types of synthesis experiments, the metal precursor is dissolved in a solvent, usually deionized water, and mixed with a reducing agent, the most common being sodium borohydride. A key advantage of preparing the nanoparticles as a colloid is that it allows the convenient production of aerosol mixtures with different carrier gases, and greater control of the concentration of the nanoparticles in the colloid. Another advantage of using a reductive synthesis is the use of *ex situ* characterization techniques to compare to the TiRe-LII derived nanoparticle sizes, including dynamic light scattering (DLS), scanning electron microscopy (SEM) and transmission electron microscopy (TEM), similar to the work by Sipkens et al. [37].

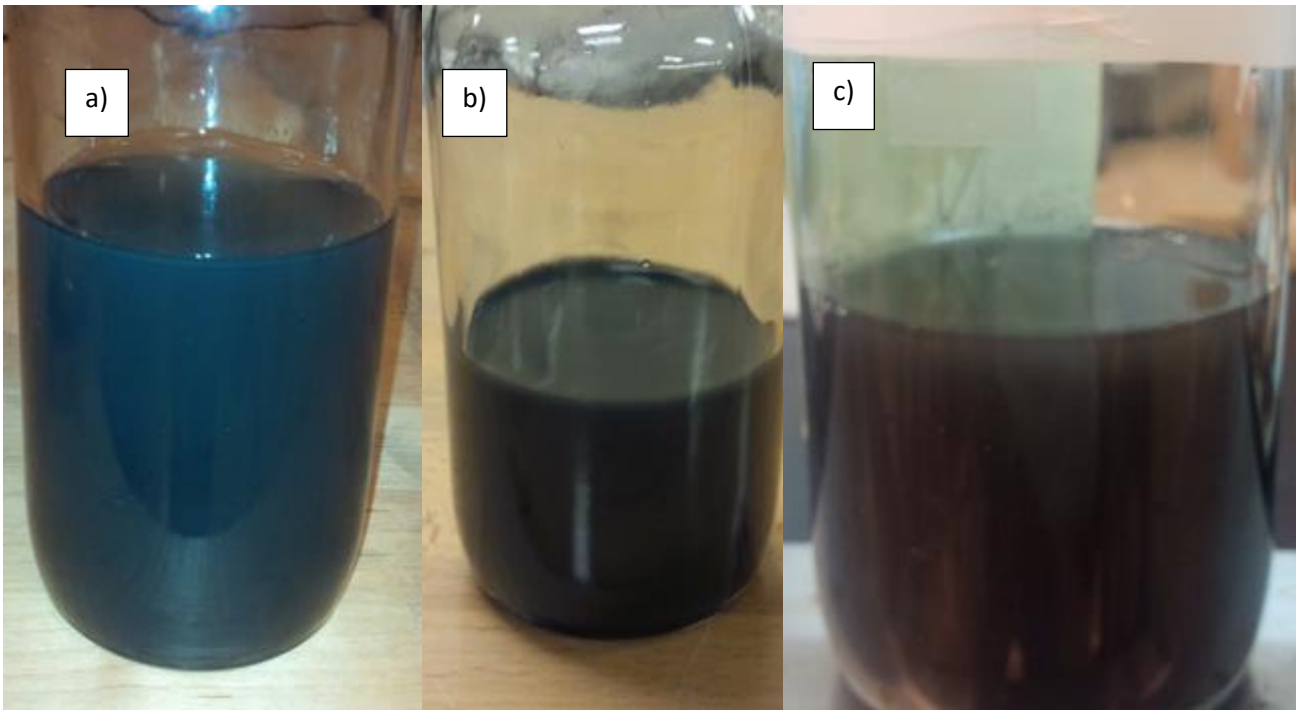

Fig. 22 Nanocolloids of: a) iron; b) silver; c) molybdenum

4.1.2 Iron Nanoparticle Preparation

The iron nanoparticles were synthesized in solution synthesized by reducing ferrous iron ions (Fe^{2+}) in a solution of sodium borohydride ($NaBH_4$) as the reducing agent and carboxymethylcellulose (CMC) to prevent agglomeration all in deionized water (DI-H_2O), following Liu et al. [69] and He and Zhao [70]. To prepare the iron colloid, 8.29 g of iron (II) sulfate heptahydrate ($FeSO_4 \cdot 7H_2O$) was dissolved in 25 mL DI-H_2O and then added to 60 mL of CMC solution (14 g/L, ca. 250 kDa) under vigorous mixing for approximately 10 minutes to ensure the formation of the CMC-Fe^{2+} complex. Separately, 1.13 g of $NaBH_4$ was dissolved in 15 mL of DI-H_2O and then slowly added to the CMC-Fe^{2+} solution, resulting in a black colloid, signifying the reduction of CMC-Fe^{2+} to CMC-Fe^0.

For the DLS analysis of the iron colloid, a refractive index of n = 2.87 was used since it corresponds to an iron nanoparticle which is surface modified with CMC polymer coating [71]. The average iron nanoparticle size was 41.9 nm with a standard deviation of 3.3 nm, measured at approximately 20 minutes after completion of the colloid synthesis. The colloid was retested at approximately 40 minutes from the completion of the synthesis and showed an average nanoparticle size of 151.9 nm and a standard deviation of 14.9 nm. While there was no apparent changes in the colour of the solution which would be an indicator

of oxidation, the increase of size was then attributed to the settling and agglomeration of the iron nanoparticles to form larger clusters.

TEM analysis was attempted on the iron colloid but the concentration of the nanoparticles was too high to gain quantitative images to allow for a statistical analysis to determine the average nanoparticle size. Qualitatively, iron nanoparticle sizes ranged from 50-500 nm, as shown in **Fig.** 23.

4.1.3 Silver Nanoparticle Preparation

The silver nanoparticles and associated SEM data were provided by Mr. Robert Liang from the University of Waterloo. The nanoparticles were synthesized in solution using the procedure outlined by Lee and Meisel [72]. A reflux condenser was attached to a three-necked round bottom flask, filled with 100 mL of deionized water and kept under a nitrogen gas atmosphere. Using a glass pipette, 1.7 mL of a 1% silver nitrate aqueous solution was added to the round bottom flask and the mixture was brought to a boil using a heating mantle for 15 minutes. Next, 2 mL of 1% citrate solution was then added to the reaction solution with a glass pipette, and the solution was left to reflux under vigorous mechanical stirring for one hour. The heating mantle was turned off and the solution was allowed to cool to room temperature before being stored in an amber glass bottle until usage.

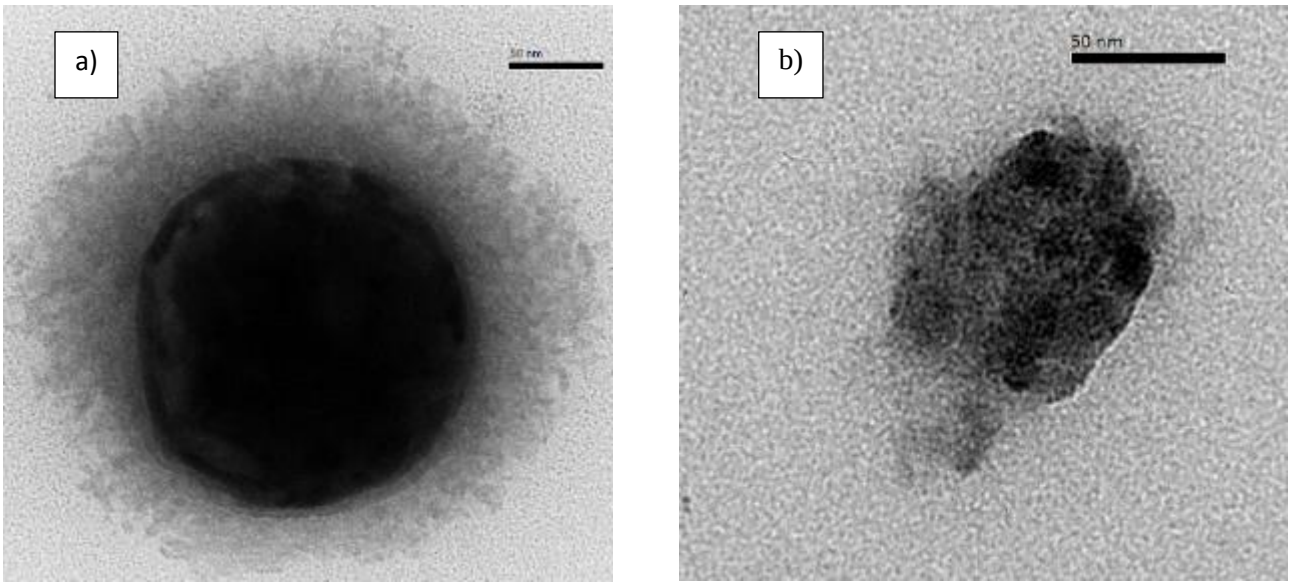

Fig. 23 Sample TEM images of the iron nanoparticles, a) a larger nanoparticle showing the CMC coating, b) a smaller nanoparticle. Scale bars corresponds to 50 nm in both images.

For the DLS analysis of the silver colloid, a refractive index of n = 0.16 was calculated for a laser wavelength of 657 nm using the data from Rakić et al. [73]. The measurements showed two separate particle sizes were initially recovered, centred at approximately 87 nm and 310 nm, likely due to the isolated silver nanoparticles and larger silver nanoparticle clusters, respectively. The sample was left undisturbed for approximately 15 minutes before retesting and two separate particle sizes were recovered again, increasing to approximately 118 nm and 337 nm, respectively. This indicates that agglomeration of both size classes of nanoparticles was present and may be observed in TiRe-LII experiments spanning over long periods of time.

SEM measurements was conducted on the silver nanoparticles shortly after synthesis using the lessons learned from having too high a concentration from the iron TEM analysis. From the image analysis, 164 individual silver nanoparticles were identified and showed a particle size range spanning from 34 nm to 95 nm, with the average particle size being 65 nm and a standard deviation of 12 nm, which is smaller than the DLS result. A sample image of the silver nanoparticles is shown in **Fig.** 24, which provides a good

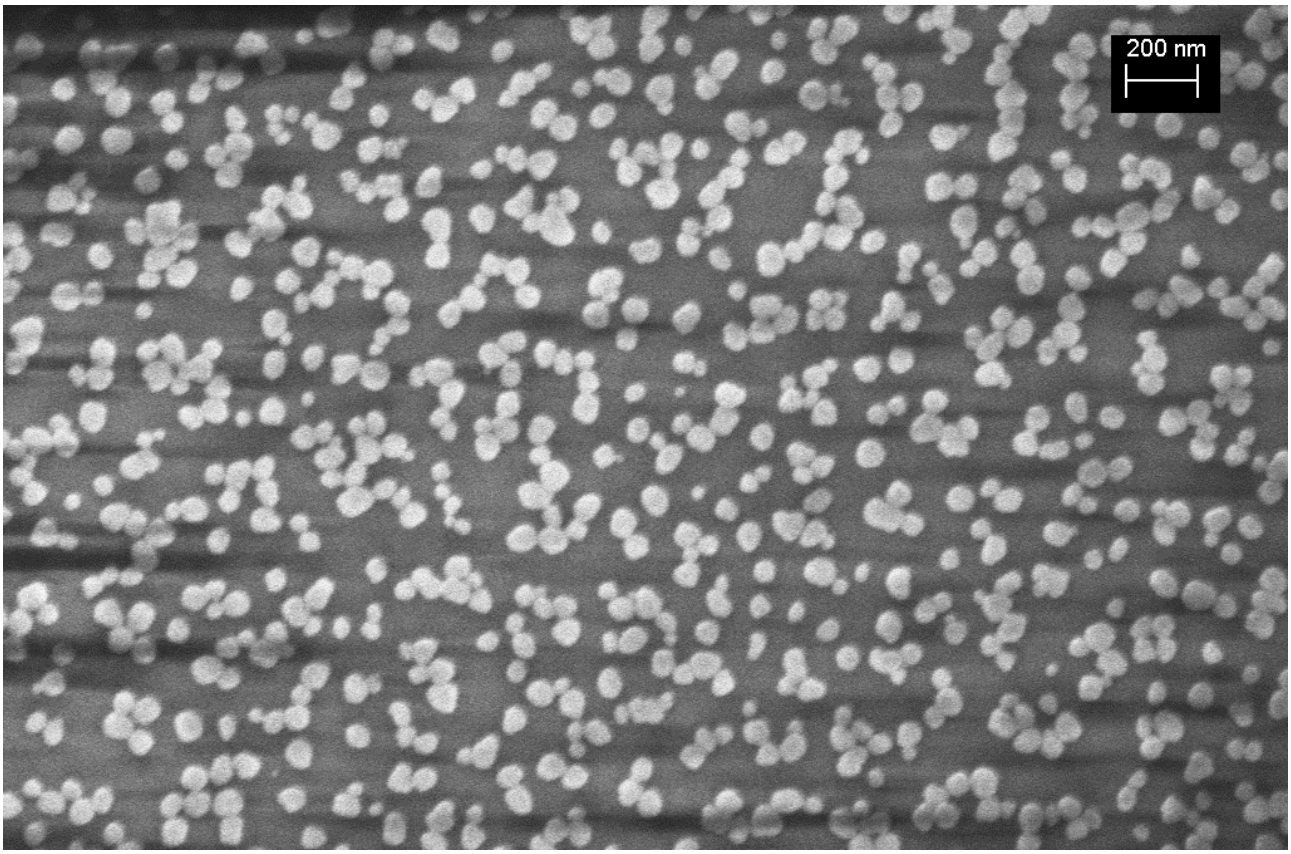

Fig. 24 Sample SEM image of the silver nanoparticles

representation of the size classes observed in the colloid. From the overall distribution is shown as a histogram in **Fig.** 25, using a 10 nm bin size, it can be seen that the silver nanoparticles studied showed a slightly right skewed normal distribution.

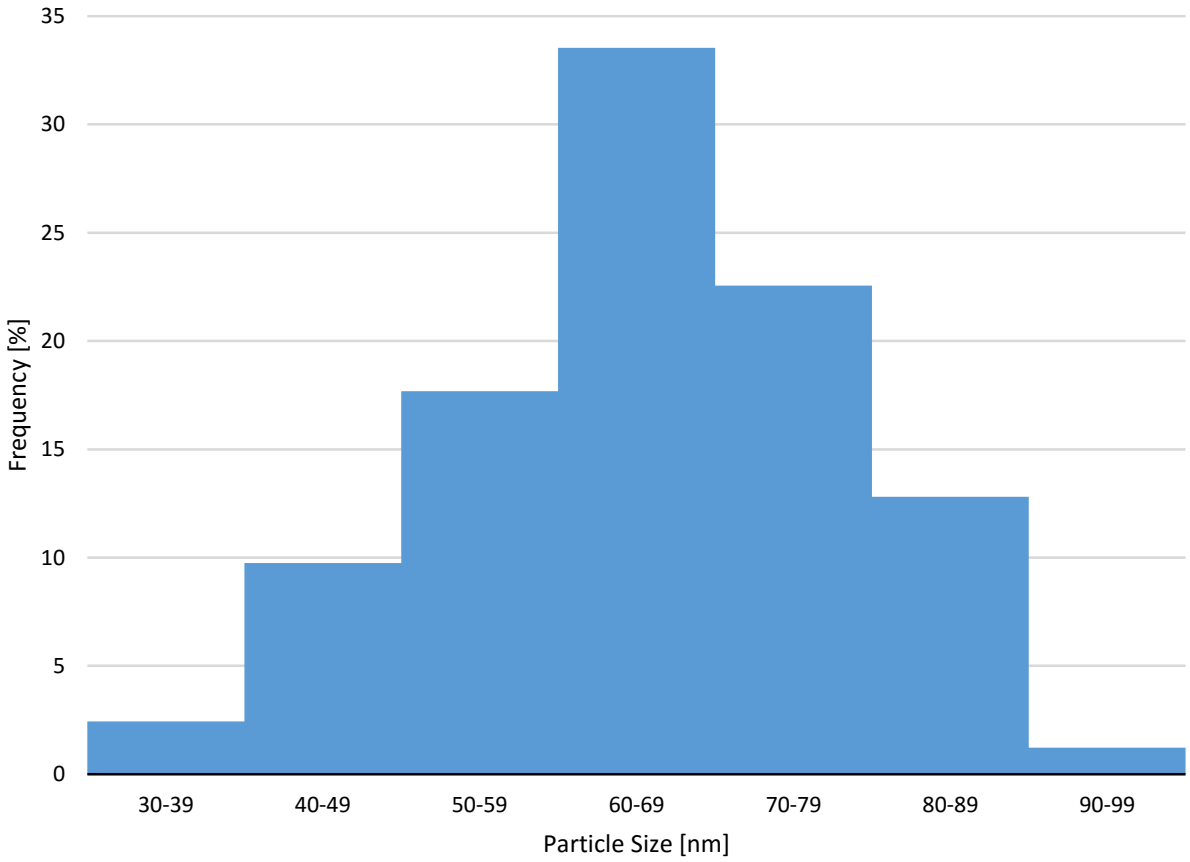

Fig. 25 Silver Nanoparticle SEM Histogram

4.1.4 Molybdenum Nanoparticle Preparation

A survey of the literature revealed no convenient reductive methods to synthesize molybdenum nanoparticles for this work with the current resources available at the time of this study. Instead, molybdenum nanoparticles were purchased from Sigma-Aldrich Canada (product number 577987, batch number MKBR4618V, nanopowder, <100 nm particle size (TEM), 99.8% purity) and was used without further purification. To prepare a molybdenum colloid, 0.5 g of the nanopowder was weighed using an analytical balance and then transferred into a vial containing 200 mL of deionized water. Unlike the other nanoparticles used in this study, the molybdenum nanoparticles had no dispersant to prevent agglomeration to larger particle clusters. To avoid the effects of nanoparticle agglomeration, the mixture was ultrasonicated for approximately 15 minutes to break up larger particle clusters to smaller nanoparticles, immediately before TiRe-LII experiments.

For the DLS analysis of the molybdenum colloid, a refractive index of n = 3.74 was selected for a laser wavelength of 653 nm, which was the closest value available to the DLS laser value of 657 nm, using the data from Ordal et al. [74]. Before the sample was ultrasonicated, a preliminary DLS measurement showed an aggregated particle size of approximately 76 nm. The sample was ultrasonicated for 15 minutes before

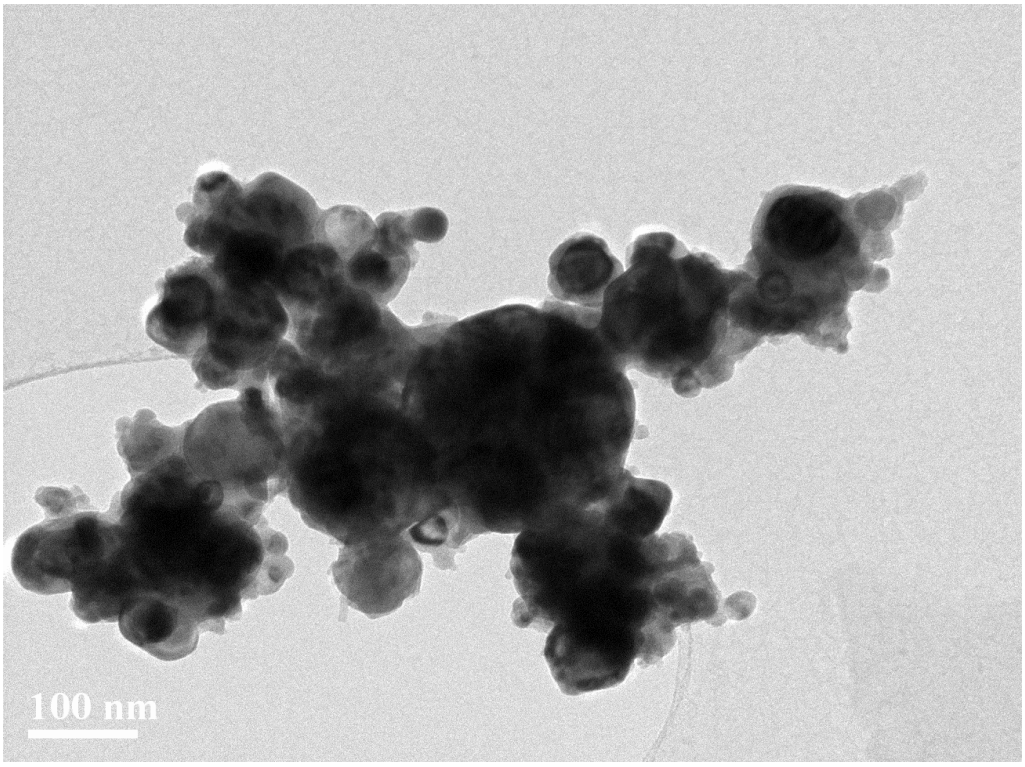

Fig. 26 Sample TEM image of a molybdenum nanoparticle cluster

retesting and the particle size had decreased to 51 nm. This indicates that agglomeration of both size classes of nanoparticles was present and may be observed in TiRe-LII experiments spanning over long periods of time.

TEM analysis of the molybdenum colloid showed that over time, there were larger clusters made up of smaller individual nanoparticles. The approximate size of the clusters ranged from 300-500 nm while the image analysis of 116 individual molybdenum nanoparticles showed a size range of 17-93 nm, with an average value of approximately 49 nm and a standard deviation of 18 nm which is in excellent agreement with the DLS results. A sample image of the molybdenum nanoparticles is shown in **Fig.** 26. Unlike the silver SEM results, the molybdenum distribution is more skewed left towards a smaller nanoparticle size and follows a more lognormal trend, as shown in **Fig.** 27, which could be attributed to the differences in the synthesis techniques utilized in the different laboratories.

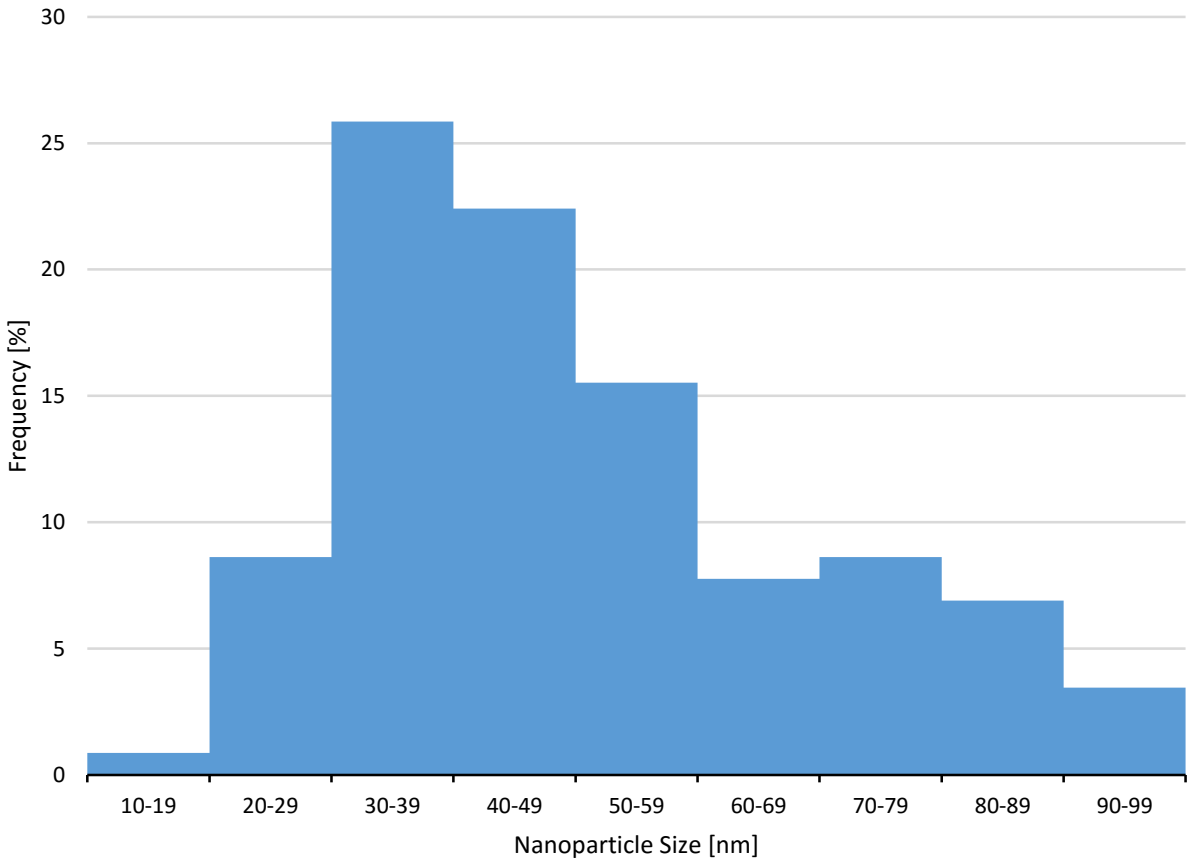

Fig. 27 Molybdenum Nanoparticle TEM Histogram

4.2 TiRe-LII Measurement Procedure

The following paragraphs describe the specific steps taken for each TiRe-LII measurement.

4.2.1 Preparation and Inspection

Before starting a TiRe-LII experiment, all of the gas tubing, and atomizer need to be inspected and cleaned of any form of contamination since trace contaminants could result in false results. The TiRe-LII setup is not designed to differentiate different incandescence sources so for example, residual soot or previous metallic nanoparticles trapped within the apparatus may give erroneous results while testing aerosols. All of the gas joints should be also be inspected to ensure that there are no leaks which may result in gases and nanoparticles escaping into the breathing environment, causing potential health concerns. To prevent this from happening, the exhaust stream from the TiRe-LII sample chamber is vented into a nearby laboratory fumehood. The sample chamber should also be inspected for contamination since the glass windows which are attached to it have previously been coated with the residue of the nanoparticles that were previously tested. When the experiment is over, pressurized shop air should be used to remove any residual nanoparticles that may have attached to the walls of any of the TiRe-LII apparatus and associated tubing.

4.2.2 Nanocolloid Synthesis and Setup

Upon the verification of the TiRe-LII and TSI atomizer system, the nanoparticles of interest are prepared as a colloid, and the carrier gas of interest is then used with the pneumatic atomizer to produce the dry aerosol. First, the colloid is loaded into a 1 L bottle with a specialized cap which allows Swagelok connections to the atomizer block. The carrier gas of interest is also connected to the atomizer block, and the gas inlet pressure is maintained at 200 kPa using a gas cylinder regulator.

4.2.3 Activate TiRe-LII Apparatus

The TiRe-LII is then turned on, starting with the laser power source and then the PMT detector module. After the instrument starts up the flashlamp Q-switch delay is checked using a remote keypad attached to the laser module, and then the associated computer software is started, Artium integrated management software (AIMS), and the appropriate experimental conditions are set, including the amount of laser pulses per experiment and the measurement recording time. Prior to taking recording the measured incandescence, trial runs are performed to ensure that the measured signals are not oversaturating the PMTs,

or to determine if the signal strength is too low, both of which are remedied by adjusting the PMT amplification gain. When the trial measurements are within the operational limits, the signals are recorded and then exported into Excel CSV files which contain the time-resolved incandesce signals at both detector wavelengths. These measurements are repeated for the different aerosol mixtures as well as the fluence study. Finally, throughout the TiRe-LII experiments, repeat measurements of the argon based aerosols are made and then used to determine if the TiRe-LII derived nanoparticle size or TAC changes over time to infer whether there is any type of measurement drift being caused by the nanoparticle chemistry changing, including agglomeration and oxidation.

4.2.3 Shut Down and Cleanup

Upon completion of the TiRe-LII experiment, the instrument is shut down by first cutting off the supply of the carrier gas of interest to the atomizer block, then the PMT detector module and laser power source are turned off. Pressurized shop air is connected to the atomizer, and then the sample chamber to remove any residual nanoparticles which may be trapped within the system. The remaining nanocolloid is collected and disposed of in accordance to the laboratory disposal guidelines.

4.3 Laboratory Safety

All laboratory work in this study was conducted according to the policies outlined by the University of Waterloo, in compliance with the workplace hazardous materials information system regulations (WHMIS). This includes, reviewing the MSDS prior to working with any chemicals, using the appropriate personal protective equipment (PPE) including lab coats and nitrile gloves, and the collection and disposal of any hazardous waste. The TiRe-LII instrument utilizes a contained class 4 laser which may cause permanent damage to the eyes, and burn skin if the appropriate precautions are not taken. Exposure to the laser can occur only during the instrument's calibration and maintenance since the laser beam is kept within a sealed enclosure at all other times. To avoid potential injury when the laser enclosure is removed, the appropriate laser glasses must be used as well as keeping the laser beam path unobstructed when the laser is in operation.

Chapter 5 Results

Upon completion of a TiRe-LII experiment, the incandescence for both the nanoparticle heating and cooling stages are recorded and then processed separately to determine the validity and application of both the spectroscopic and heat transfer model proposed. The incandescence values are converted to effective temperatures using two-colour pyrometry and the peak temperatures to serve as a first check on whether the selected experimental or Drude theory derived $E(\mathbf{m}_\lambda)$ values result in the temperatures being physically realistic and how do these temperatures change when compared to the previous assumption that $E(\mathbf{m}_\lambda)$ only weakly changes as function of wavelength and can be treated as unity. The nanoparticle cooling temperatures are used in the statistical model to recover the nanoparticle size and TAC, when applicable. Finally the results of the nanoparticle size and TAC recovery using heat transfer model with the selected physical parameters for the different iron, silver and molybdenum aerosol mixtures are presented.

5.1 Fluence and Spectroscopic Results

The first component of TiRe-LII analysis is determining if there is any change in the observed peak temperature when the laser fluence changes. In previous TiRe-LII studies conducted on soot [75], it was expected that the observed peak TiRe-LII signal or its equivalent effective temperature to increase with an increase of fluence until a plateau value is reached. This roughly corresponds to the sublimation temperature, and indicates the point where additional laser energy is offset by increased heat losses through phase change. By doing this analysis first, information could be gained to determine which heat transfer modes will be dominant for the material being used.

The spectroscopic properties could also be validated by performing an energy balance during the heat up stage of the TiRe-LII experiment. Following Eremin et al. [76] the complex index of refraction of the nanoparticles at the excitation laser frequency can be inferred from the peak pyrometrically-defined temperature found using $E(\mathbf{m})_r$ by performing an energy balance between the start of the laser pulse, when the nanoparticles are at T_g, and the pyrometrically-defined peak nanoparticle temperature, $T_{p,max}$,

$$q_{in} = \rho \frac{\pi d_p^3}{6} \left[H^\circ \left(T_{p,\max} \right) - H^\circ \left(T_g \right) \right] = q_{abs} - q_{cond} - q_{evap} \tag{22}$$

where $H^{\circ}(T_g)$ and $H^{\circ}(T_{p,max})$ is the enthalpy of the material at T_g and $T_{p,max}$. Although $T_{p,max}$ is due to a balance between q_{abs}, q_{evap}, q_{cond}, and the change in enthalpy of the nanoparticles, Eq. (20) can be simplified by neglecting evaporation and conduction heat transfer before the peak nanoparticle temperature is reached, in which case,

$$q_{abs} = C_{abs,\lambda_{laser}} F_0 = \frac{\pi d_p^2}{4} Q_{abs,\lambda_{laser}} \left(\mathbf{m}_{\lambda_{laser}}\right) F_0 = \frac{\pi^2 d_p^3}{\lambda_{laser}} E\left(\mathbf{m}_{\lambda_{laser}}\right) F_0 \tag{23}$$

where F_0 is the laser fluence in units of J/cm^2. Substituting Eq. (21) into Eq. (20) gives an expression for $E(\mathbf{m}_{\lambda laser})$,

$$E\left(\mathbf{m}_{\lambda_{laser}}\right) = \frac{\lambda_{laser} \rho\left(T_g\right)\left[H^{\circ}\left(T_{p,\max}\right) - H^{\circ}\left(T_g\right)\right]}{6\pi F_0} \tag{24}$$

where Eq. (22) could be used to approximate a lower bound estimate for $E(\mathbf{m}_{\lambda laser})$. The following sections, 5.1.1-5.1.3, discuss the specific results for the iron, silver, and molybdenum experiments.

The peak temperatures of the iron nanoparticles were calculated using $E(\mathbf{m})_r = 0.539$ taken from Krishnan et al. [45]. The peak temperature was plotted against the laser fluence and is shown in **Fig.** 28 for the Ar, N_2, and N_2O aerosol mixtures, where the error bars correspond to one standard deviation from the average peak temperature. At the time of testing CO_2 gas was not available and was replaced with another linear triatomic gas, N_2O; from the remainder of the fluence analysis in this work and consistent with Sipkens et al. [37], the peak temperatures calculated for each nanomaterial are independent of the aerosol mixture being tested and which is in contrast to Eremin et al. [77] who observed that the peak temperatures depended on the pressure and gas used in the aerosol mixture. A general trend observed is that at the lower fluences, the measured incandescence have a very poor signal to noise ratio and the standard deviation of the peak temperatures is significantly larger than the higher fluence measurements. With the exception of the lowest fluence data point, all three aerosol mixtures showing an increasing peak temperature as the fluence increases, from approximately 2750 K to 2850 K, well below the boiling point of iron, 3134 K [58] and indicates that cooling occurs in a mixed conduction and evaporation dominant regime. This result suggests that the energized nanoparticles is approaching the sublimation temperature but due to the limitations with the selected TiRe-LII's maximum fluence, further studies will be required at higher fluences.

To get a lower bound estimate on $E(\mathbf{m}_{\lambda laser})$, Eq. (22) was solved by setting the maximum temperature equal to the boiling point, resulting in $\left[H^{\circ}\left(T_{BP}\right)-H^{\circ}\left(T_{g}\right)\right]$ = 2026 kJ/kg taken from Desai [56], and using F_0 = 0.188 J/cm^2 results in $E(\mathbf{m}_{\lambda laser})$ = 0.479 which is significantly larger than the 0.065 value extrapolated from Krishnan et al. [45]. Sipkens et al. [37] reinterpreted from the data from Kock et al. [18], and calculated $E(\mathbf{m}_{\lambda laser})$ = 0.39 which is consistent with the value calculated in this study. To provide a comparison of these results to the literature, the MLE recovered iron nanoparticle size, shown in the next section, was used to calculate the size parameter and the $E(\mathbf{m}_{\lambda laser})$ is plotted against the results from Kock et al. [18], Eremin et al. [76], and the expected results from Mie theory, shown in **Fig.** 29. It can be seen that all of the experimentally determined $E(\mathbf{m}_{\lambda laser})$ values are larger than the Mie theory calculated values, a result that requires further experiments to determine the root cause of this deviation.

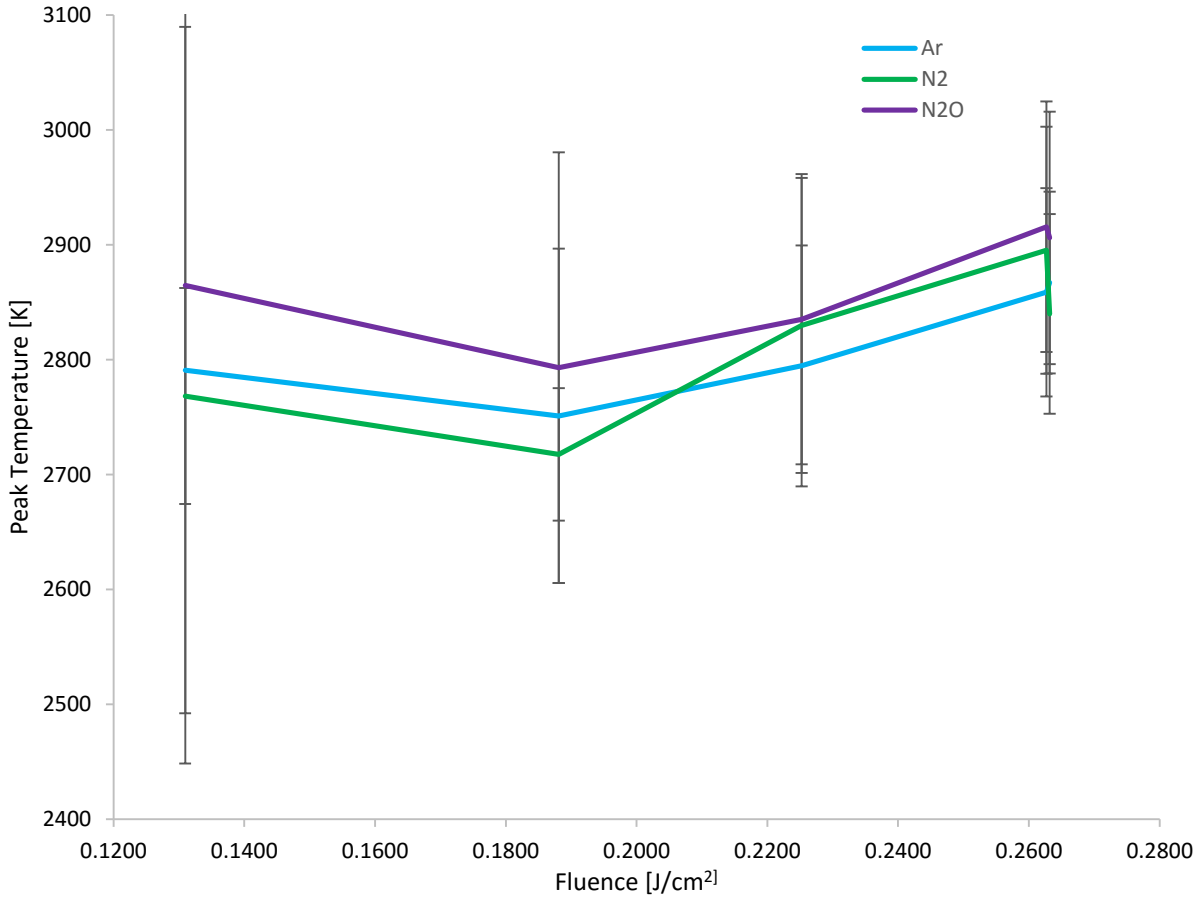

Fig. 28 Peak temperature vs fluence for iron nanoparticles

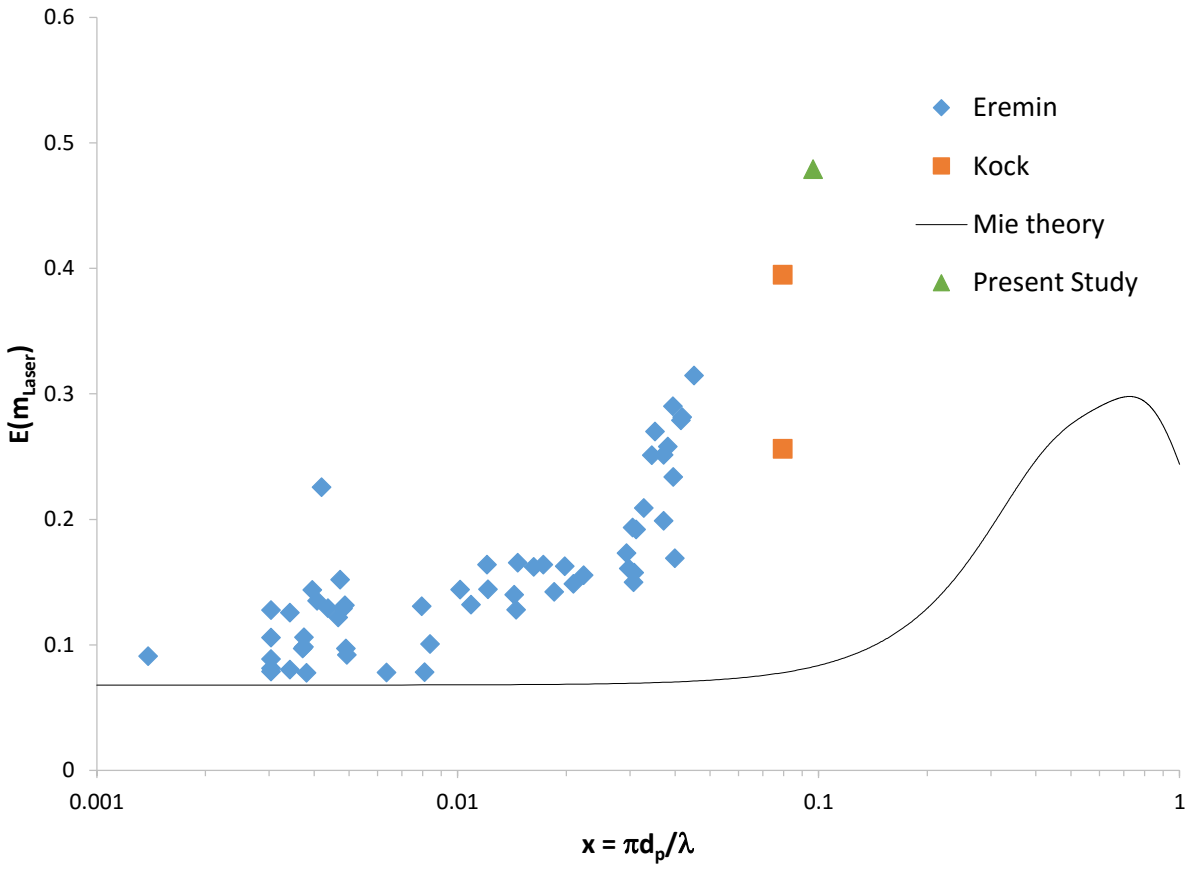

Fig. 29 Comparison of the $E(\mathbf{m}_{\lambda laser})$ from this study to the literature and Mie theory for iron

The peak temperatures of the silver nanoparticles were calculated using $E(\mathbf{m})_r$ = 0.366 derived from Drude theory using the data from Krishnan et al. [45] and Miller [43]. The peak temperature was plotted against the laser fluence and is shown in **Fig.** 30 for the Ar, N_2, and CO_2 aerosol mixtures, where the error bars correspond to one standard deviation from the average peak temperature. All three aerosol mixtures exhibit a maximum peak temperature of approximately 2800 K, well above silver's boiling point of 2466 K [59] and indicates that cooling occurs in an evaporation dominant regime. This result suggests that they're may be some superheating mechanism which is not being considered in the proposed models but further investigation is required. Also, the peak temperatures are generally consistent regardless of the fluence, unlike iron and molybdenum which show a general increase of peak temperature as the fluence increases, but this could be attributed to the temperatures already exceeding the boiling point of the silver nanoparticles.

To get a lower bound estimate on $E(\mathbf{m}_{\lambda laser})$, Eq. (22) was solved by setting the maximum temperature equal to the boiling point, resulting in $\left[H^{\circ}\left(T_{BP}\right)-H^{\circ}\left(T_{g}\right)\right]$ = 643 kJ/kg extrapolated from Cagran et al. [57], and using F_0 = 0.206 J/cm^2 leads to $E(\mathbf{m}_{\lambda laser})$ = 0.185 which is significantly larger than the 0.017 and 0.014 values reported by Krishnan et al. [45], and Miller [43], respectively.

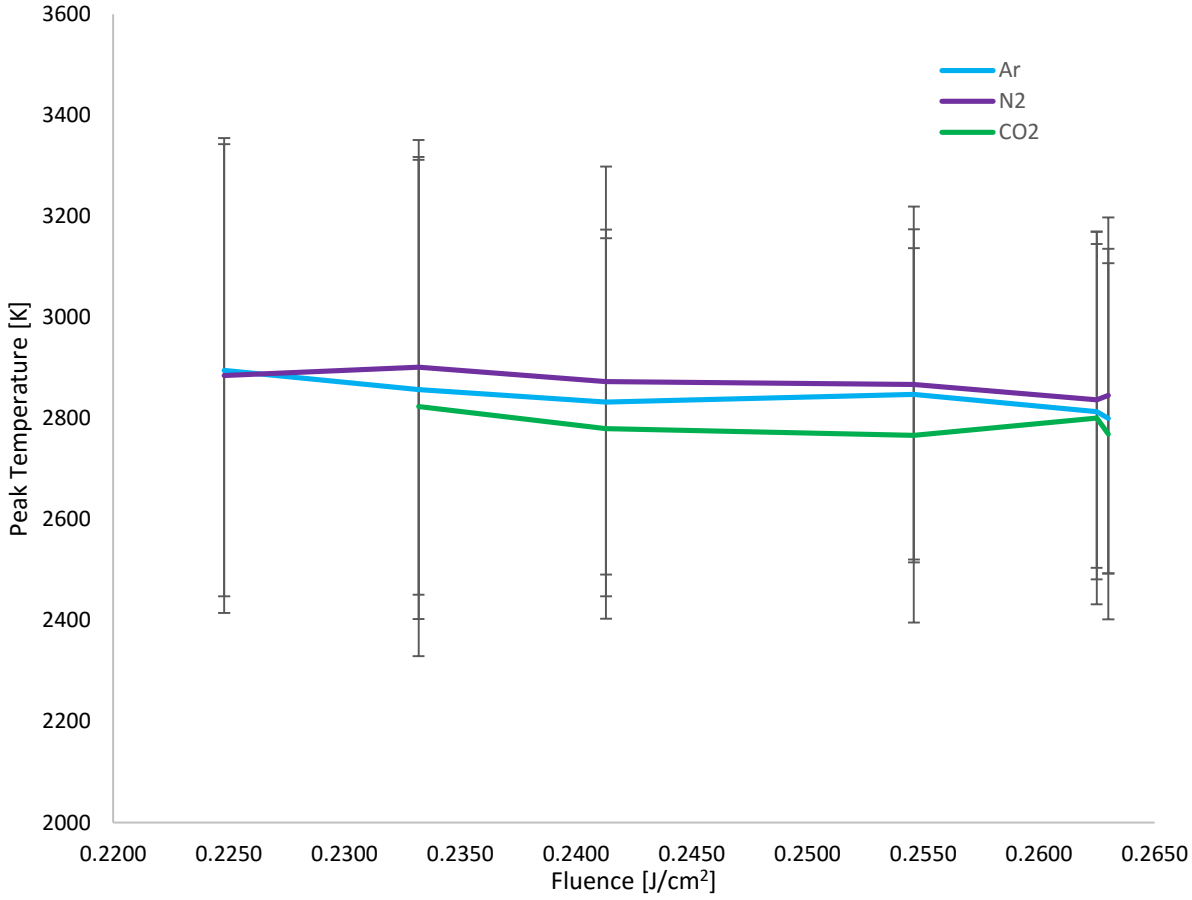

Fig. 30 Peak temperature vs fluence for silver nanoparticles

The peak temperatures of the molybdenum nanoparticles were calculated using $E(\mathbf{m}_{\lambda})_r$ = 0.642 derived from the experimental data from Barnes at 2000 K [51]. The peak temperature was plotted against the laser fluence and is shown in **Fig.** 31 for the Ar, N_2, and CO_2 aerosol mixtures, where the error bars correspond to one standard deviation from the average peak temperature. Unlike the iron and silver nanoparticles, the aerosol mixtures exhibit an increase of the calculated peak temperature as the laser fluence increases, starting from approximately 2830 K at 0.206 J/cm^2 and increasing to 2930 at 0.263 J/cm^2, slightly above molybdenum's melting point of 2896 K [50]. Due to the limitations of the TiRe-LII instrument not being able to exceed fluences of 0.263 J/cm^2, it is difficult to draw conclusions on whether

the system is approaching a steady state peak temperature as expected in soot from this experiment [75]. Another study from Eremin and Gurenstov [78] showed a possible steady-state peak temperature of approximately 3900 K at fluences higher than 0.3 J/cm^2 which is still significantly lower than the boiling temperature of bulk molybdenum, 4913 K [60], and may require further investigation, possibly with different particle sizes. To get a lower bound estimate on $E(\mathbf{m}_{\lambda laser})$, Eq. (22) was solved by setting the maximum temperature equal to the boiling point, resulting in $\left[H^{\circ}\left(T_{BP}\right)-H^{\circ}\left(T_{g}\right)\right]$ = 10280 kJ/kg taken from Desai [62] and using F_0 = 0.206 J/cm^2 in $E(\mathbf{m}_{\lambda laser})$ = 0.038 which is consistent with the value interpolated from Barnes [51] which is 0.065.

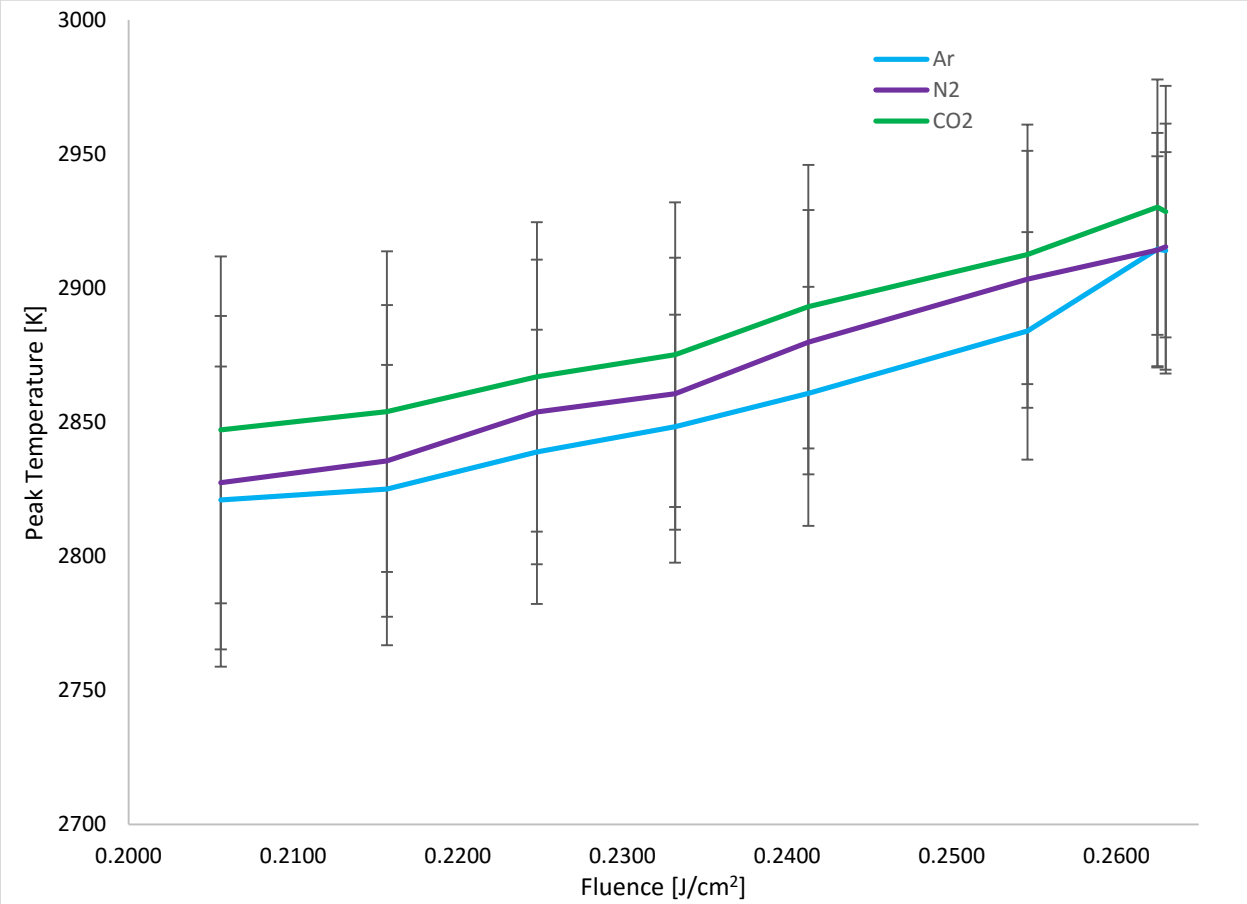

Fig. 31 Peak temperature vs fluence for molybdenum nanoparticles

Overall, it was shown that the $E(\mathbf{m}_{\lambda laser})$ for iron and silver were significantly higher when calculated using Eq. (22) using the data from the TiRe-LII experiments, when compared to the approximated values from the data available from the literature while molybdenum is the only value that is consistent between the TiRe-LII derived value and the value based on the literature value. Both iron and

molybdenum showed an increase of the calculated peak temperatures as the laser fluence increased, which was approaching their boiling and melting temperatures respectively, while silver showed a consistent peak temperature well above its boiling point. From this, it is difficult to draw conclusions from this analysis since the temperatures calculated are very sensitive to changes in the $E(\mathbf{m}_\lambda)$ values used to interpret the data. For example, the peak temperatures for silver is plotted again in **Fig.** 32 but calculated for both $E(\mathbf{m})_r = 0.366$ and $E(\mathbf{m})_r = 1$, with the error bars omitted for clarity. It can be seen that the peak temperatures calculated with $E(\mathbf{m})_r = 1$ are approximately 3600-3800 K which is significantly higher than the values calculated with $E(\mathbf{m})_r = 0.366$, which is approximately 2700-2900 K. This result is consistent for the other aerosol mixtures in this study and provides evidence for using accurate experimentally determined $E(\mathbf{m}_\lambda)$ values for molten metals. Since there is currently a lot of uncertainty in the optical properties for these materials, there needs to be further research into obtaining more reliable experimental values to minimize the error associated with using a specific $E(\mathbf{m})_r$ value.

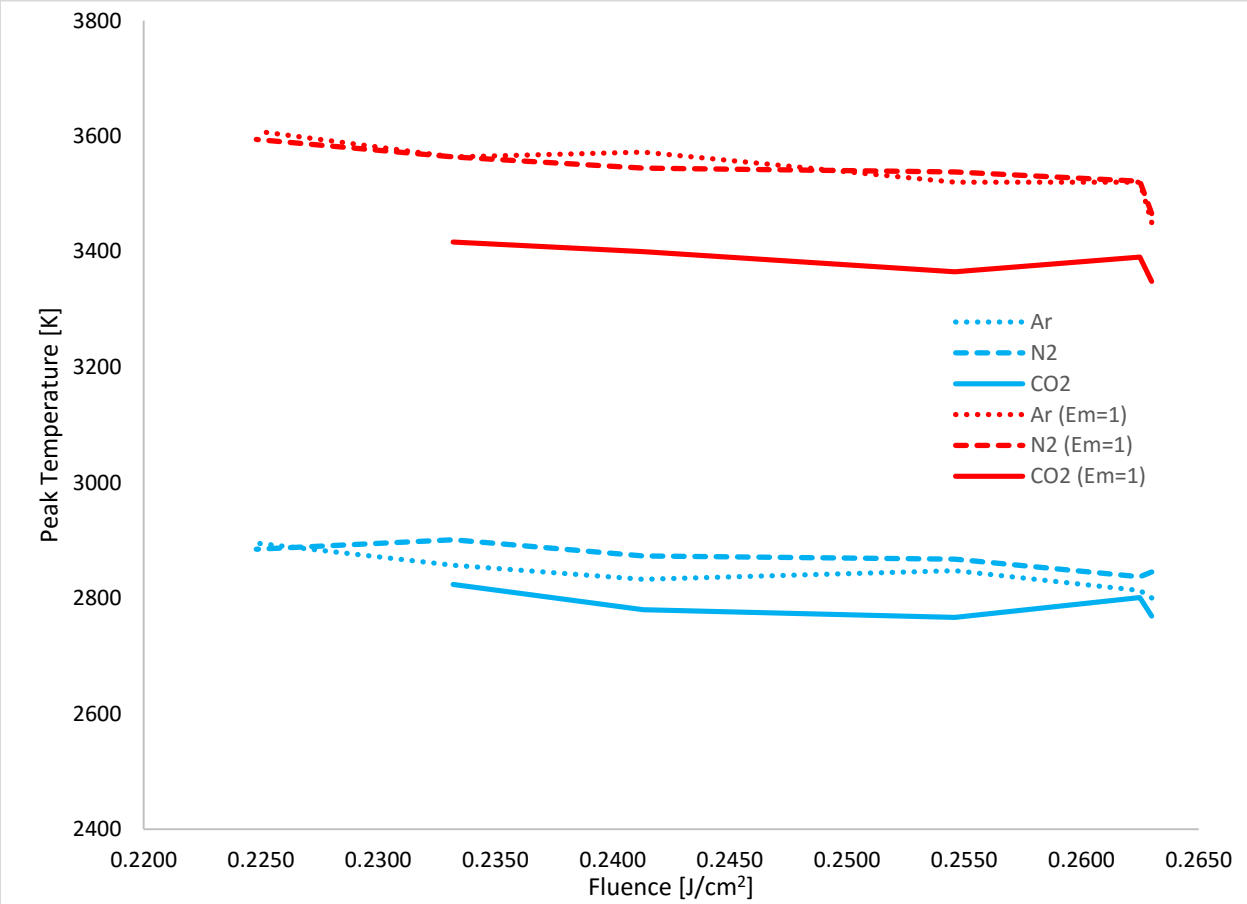

Fig. 32 Peak temperature vs fluence for silver nanoparticles for $E(\mathbf{m})_r = 0.366$ and $E(\mathbf{m})_r = 1$

5.2 TiRe-LII Nanoparticle Size and TAC Analysis

The nanoparticle size and the TAC for each of the aerosol mixtures were attempted to be recovered using the statistical framework previously outlined in Section 2.3. Using the peak temperature values from section 5.1, the iron data was interpreted using a combined evaporation and conduction model ($\mathbf{x} = [d_p, \text{TAC}]^T$), silver with an evaporation only model ($\mathbf{x} = [d_p]^T$), and conduction only model for molybdenum. As previously stated, for molybdenum, the nanoparticle size to TAC ratio can only be determined through the statistical framework, and will usually get trapped within a local minimum, so to get useful information out of this process, the molybdenum nanoparticle size was set to the TEM determined value of 49 nm and the TAC was recovered $\mathbf{x} = [\alpha]$. All three materials were expected to follow a lognormal nanoparticle size distribution and the value of σ_g was selected to be 1.5 as per previous studies [37].

5.2.1 Nanoparticle size and TAC recovery

The results for the iron nanoparticle TiRe-LII analysis are summarized in **Table** 3 using $E(\mathbf{m})_r$ = 0.539 taken from Krishnan et al. [45], and the uncertainties correspond to one standard deviation from the measurement. From the previous sections and from previous studies [18, 37], it is expected that the iron nanoparticle cooling occurs in the same temperature range which has sufficient heat transfer from both conduction and evaporation, which allows for the simultaneous and as expected the model was able to recover an optimal pair of the nanoparticle size and TAC which best fits the model to the data. The recovered nanoparticle sizes are significantly smaller than the DLS calculated value of 41.9 nm, which signifies that even though the model gives an excellent fit to the experimental values, there may be an underlying deficiency in some of the material properties which is leading to this discrepancy, most of likely being the $E(\mathbf{m})_r$ value. To attempt to improve upon the model fit, the $E(\mathbf{m})_r$ was adjusted until it was found that $E(\mathbf{m})_r$ = 0.909 provided an improved fit of the modelled temperature to the experimental temperatures, but is well above the experimental $E(\mathbf{m})_r$ value. The modeled and experimental temperatures are shown in **Fig.** 33 for the $E(\mathbf{m})_r$ = 0.909 fit, and the contour plot used to determine the uncertainty intervals is shown in **Fig.** 34 along with the MLE. As expected the signal to noise ratio decreases as the measurement time increases, resulting in a poorer model fit to the data, notably at times exceeding 500 ns as shown in **Fig.** 33.

Table 3 Iron nanoparticle TiRe-LII size and TAC analysis

Gas	x	$E(\mathbf{m})_r$ = 0.539		$E(\mathbf{m})_r$ = 0.909	
		MLE	**Uncertainty**	**MLE**	**Uncertainty**
Ar	d_p [nm]	11.0	0.07	32.7	1.9
	TAC	0.091	0.002	0.24	0.03
N_2	d_p [nm]	10.3	0.1	29.9	1.0
	TAC	0.028	0.0006	0.06	0.01
CO_2	d_p [nm]	10.4	0.06	29.0	1.4
	TAC	0.051	0.0006	0.11	0.01
TEM	d_p [nm]	50-500	-	-	
DLS	d_p [nm], 20 min	41.9	3.3		
	d_p [nm], 40 min	151.9	14.9		

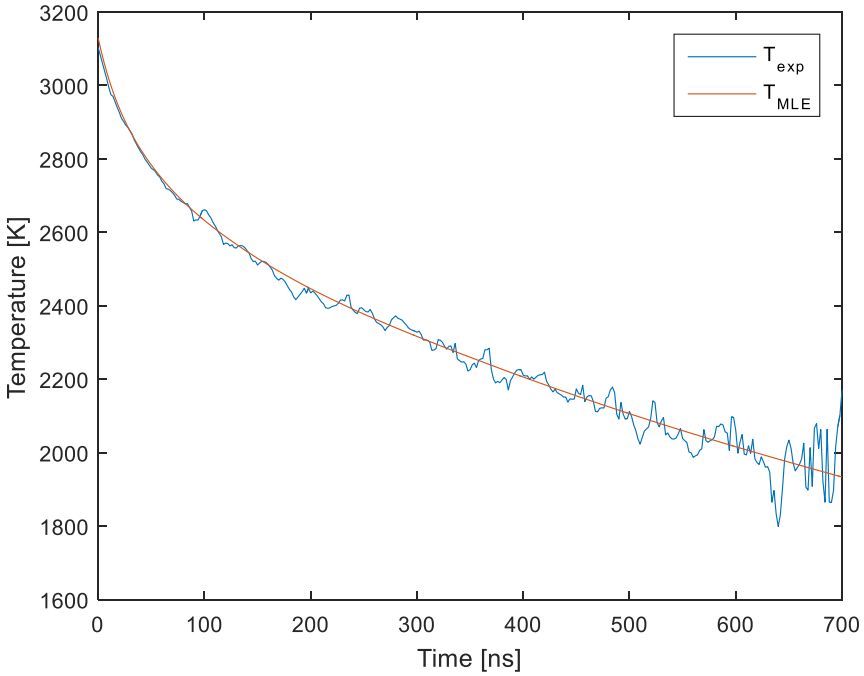

Fig. 33 Plot of the experimental and modeled temperatures for the Fe-Ar aerosol

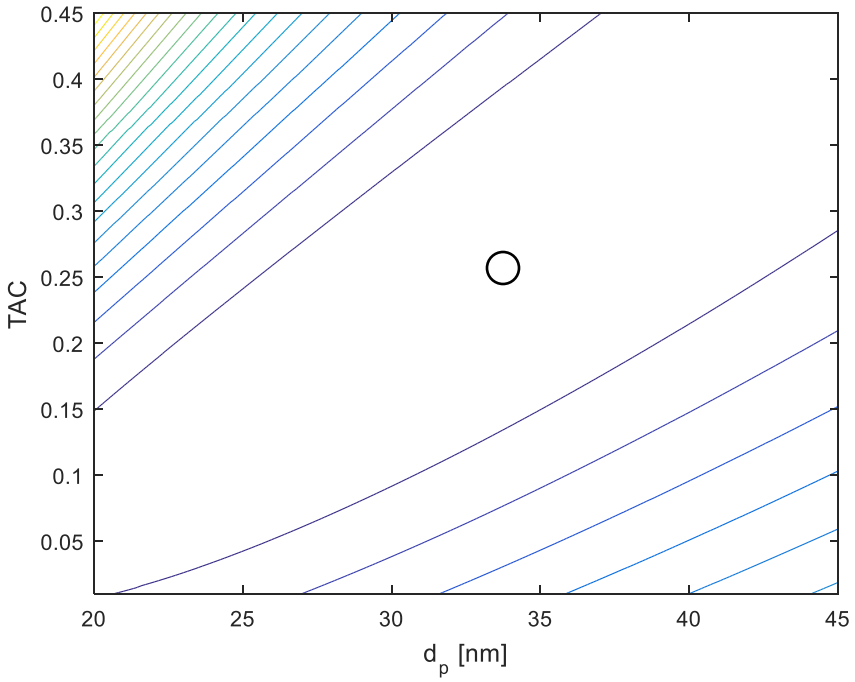

Fig. 34 Contour plot of the likelihood for the Fe-Ar aerosol

Throughout the experiment, there were visible changes in the colour of the iron nanocolloid, which is attributed to the oxidation of the iron nanoparticles to iron oxide. This colour change is shown in **Fig.** 35, at the synthesis completion where the mixture is homogenously black, at one hour where orange

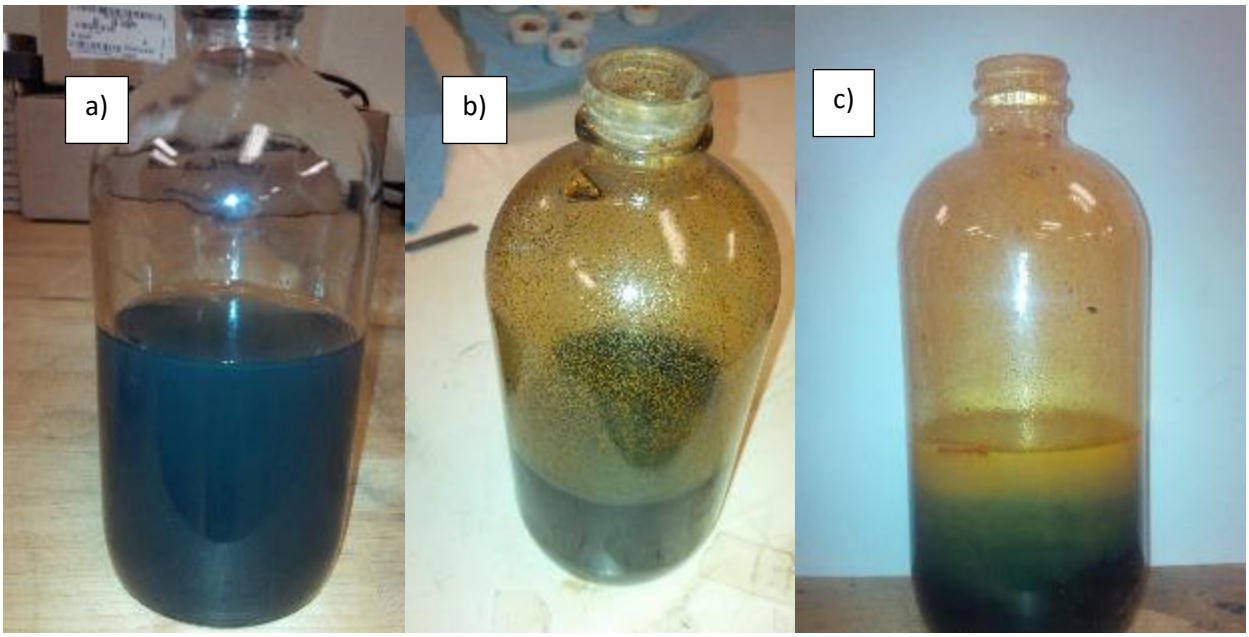

Fig. 35 Iron nanoparticle colloid colour at: a) synthesis completion; b) one hour; c) six hours

residue can be seen, and at approximately six hours where there is a significant amount of orange residue. This was only observed for the iron nanoparticles as there was no apparent visual indicators for the silver and molybdenum colloids; this should be further investigated in future experiments to determine if this is truly the case. TiRe-LII measurements on the Fe-Ar mixture was repeated at 4 intervals over the duration of the TiRe-LII experiment to determine if there were any changes in the TAC over time, and the results are shown in **Fig.** 36. As shown, there is a gradual increase of the TAC over time, and for the second set of measurements, there is a very large spread of TAC values calculated, with no experimental deviation from the other sets of measurements.

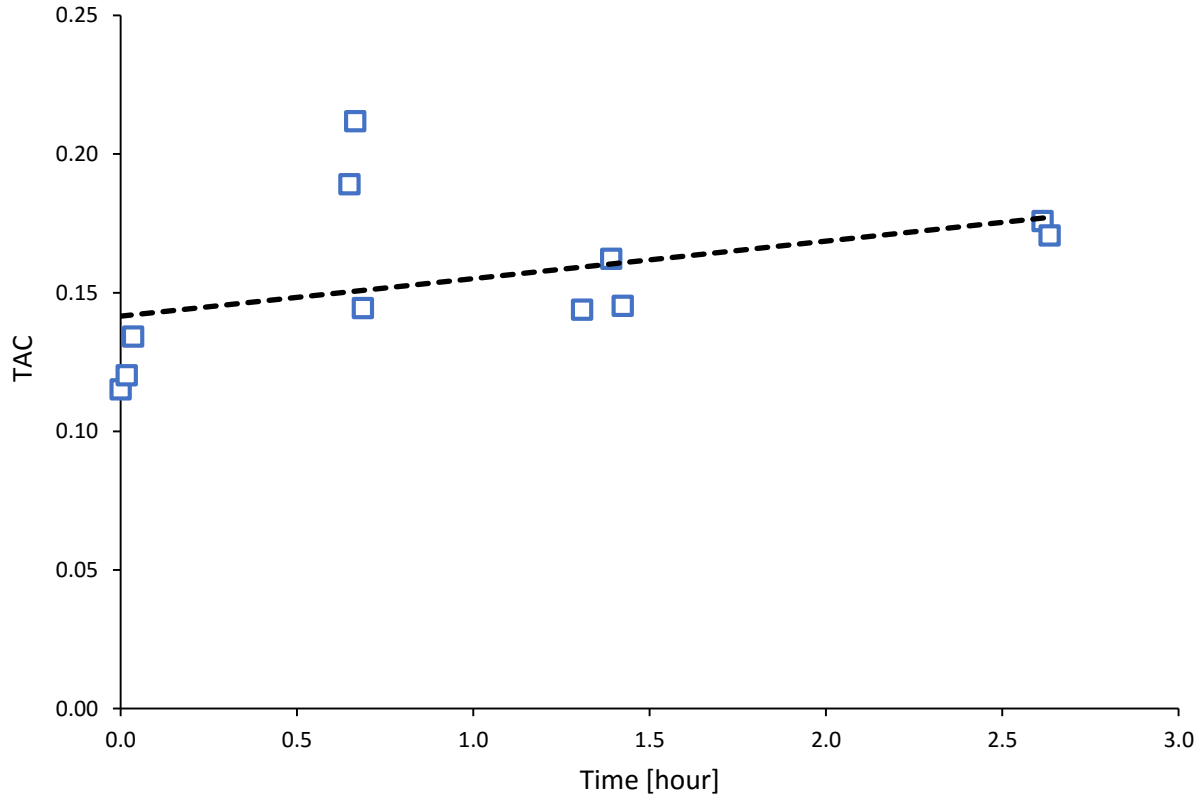

Fig. 36 Time evolution of the TAC for a Fe-Ar mixture during a TiRe-LII experiment

The silver nanoparticle TiRe-LII measurements were interpreted using $E(\mathbf{m})_r = 0.366$ derived from Drude theory using the data from Krishnan et al. [45] and Miller [43], summarized in **Table** 4 along with the one standard deviation error margins. From the previous sections, it is expected that the heat transfer mode occurs in the evaporation only regime, and attempts to incorporate the conduction model in the

interpretation of the data lead to unphysical values of the TAC being calculated. This included the TAC being on the order of 10^3 in an attempt to increase the conduction model values to a comparable level to the evaporation model. Since this is a nonphysical value as the TAC is an efficiency value bound between 0 and 1, the conduction model was disabled during this analysis. The TiRe-LII values for Ar and N_2 with each other but CO_2 was noticeably smaller than the other aerosol mixtures. Also, the Ar and N_2 values are consistent with the DLS results, 87 nm, but are larger than the SEM results, 65 nm, which is consistent with the CO_2 values.

One of the key issues with silver nanoparticles and the TiRe-LII experiments, which was also reported in the literature by Fillipov et al. [16], was that silver has poor optical properties in the visible and infrared spectrum, and the measured incandescence values were consistent with this by exhibiting poor signal strength. The TiRe-LII PMTs were set at their maximum operating gains which inherently increases the magnitude of the electrical noise observed in the incandescence signals and overall, resulting in a poor signal to noise ratio, even when the amount of measurements was increased to 500 runs per silver aerosol mixture. Another significant cause of this discrepancy is due to the fact that the TiRe-LII measurements from this study and from the literature on silver occur on a much shorter time scale than iron and molybdenum, at approximately < 80 ns [16] compared to over 500 ns [37, 19, 20], respectively. Due to the poor signal to noise ratio, the incandescence signals are rarely usable after 80 ns resulting in much less data being used to regress with the heat transfer model, and is a significant contribution of the model's uncertainty. This is shown in **Fig**. 37 where the modeled temperatures generally capture the experimental temperatures cooling trend but fail to replicate the specific features of the experimental data, with the associated contour plot shown in **Fig.** 38. The conduction model and the TAC was used to calculate the likelihood with the evaporation model, but was still shown to have a minimal impact on the likelihood demonstrated by the near one dimensional dependence on the candidate nanoparticle size.

Table 4 Silver nanoparticle TiRe-LII size analysis

Gas	x	MLE	Uncertainty
Ar	d_p [nm]	82	7
N_2	d_p [nm]	89	10
CO_2	d_p [nm]	75	8
SEM	d_p [nm]	65	12
DLS	d_p [nm], 0 min	87	4.4
	d_p [nm], 15 min	118	5.9

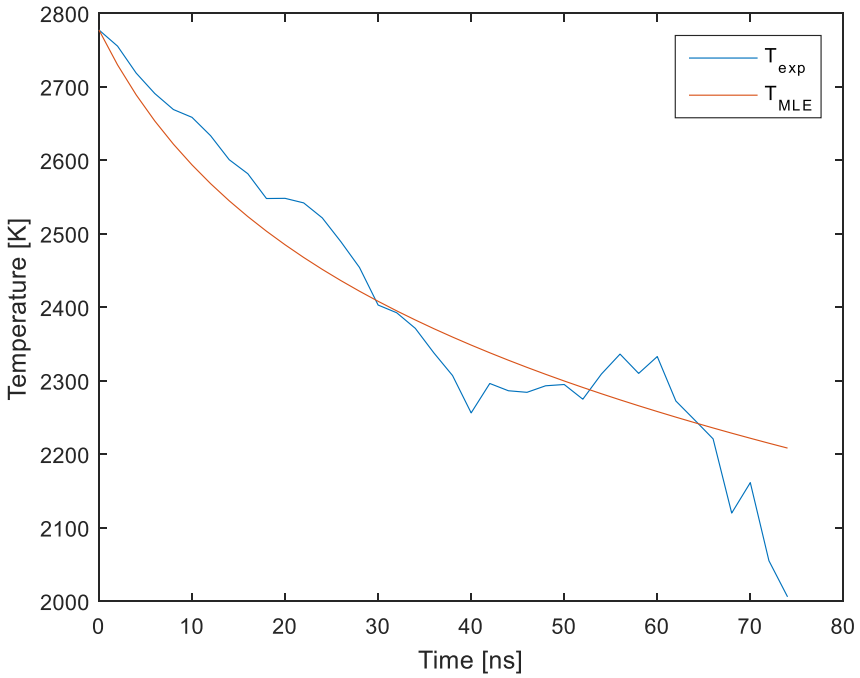

Fig. 37 Plot of the experimental and modeled temperatures for the Ag-Ar aerosol

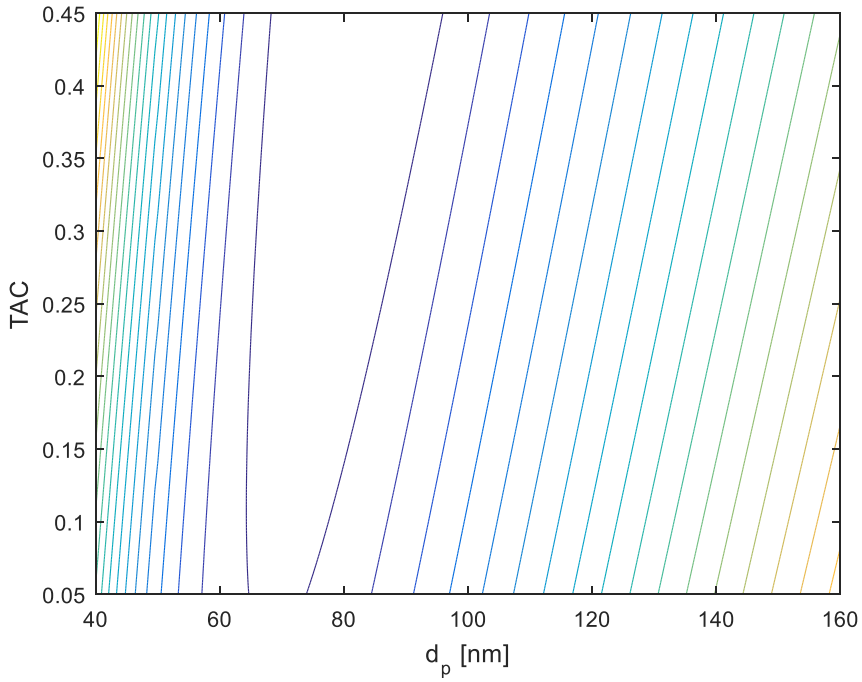

Fig. 38 Contour plot of the likelihood for the Ag-Ar aerosol

For the molybdenum nanoparticles, the TiRe-LII measurements were interpreted using $E(\mathbf{m}_\lambda)_r$ = 0.642 derived from the experimental data from Barnes at 2000 K [51], with the uncertainty corresponding to one standard deviation from the measured value. From the previous sections, and from the literature [19, 20], it is expected that the molybdenum nanoparticle cooling temperatures occur around its melting point and below, which corresponds to a conduction only heat transfer regime. Also from the same studies, this means that the nanoparticle size and TAC values cannot be independently recovered as they are solved as a fixed ratio, unless extra information about either the nanoparticle size or the TAC is incorporated into the model. From the DLS and TEM *ex situ* analysis, the molybdenum nanoparticle size was determined to be 51 and 49 nm respectively, so for this study the TEM molybdenum size was incorporated into the model and the TAC for the aerosol mixtures were recovered, summarized in **Table** 5.

Table 5 Molybdenum nanoparticle TiRe-LII TAC analysis using the TEM nanoparticle size

Gas	x	MLE	Uncertainty
Ar	TAC	0.24	0.002
N_2	TAC	0.16	0.001
CO_2	TAC	0.21	0.002
TEM	d_p [nm]	49	18
DLS	d_p [nm], no sonication	76	3.8
	d_p [nm], 15 min sonication	51	2.6

The modelled and experimental temperatures for the Mo-Ar mixture is shown in **Fig**. 39, where the model only fit to the experimental temperatures outside of the anomalous cooling regime, which occurs up to approximately 300 ns. A plot of the likelihood, calculated using the conduction model is shown in **Fig.** 40, with the MLE nanoparticle size and TAC ratio labelled as the dashed line. As expected the fixed ratio between the nanoparticle size and TAC can be seen from the almost linear arrangement of the contour lines. This further supports that for conduction dominant TiRe-LII analysis, an *ex situ* method of determining either the nanoparticle size or TAC is required to recover the other, or if there is prior knowledge or approximate value of the expected TAC of the material being tested, the nanoparticle size can be recovered, as the former was the case in this study.

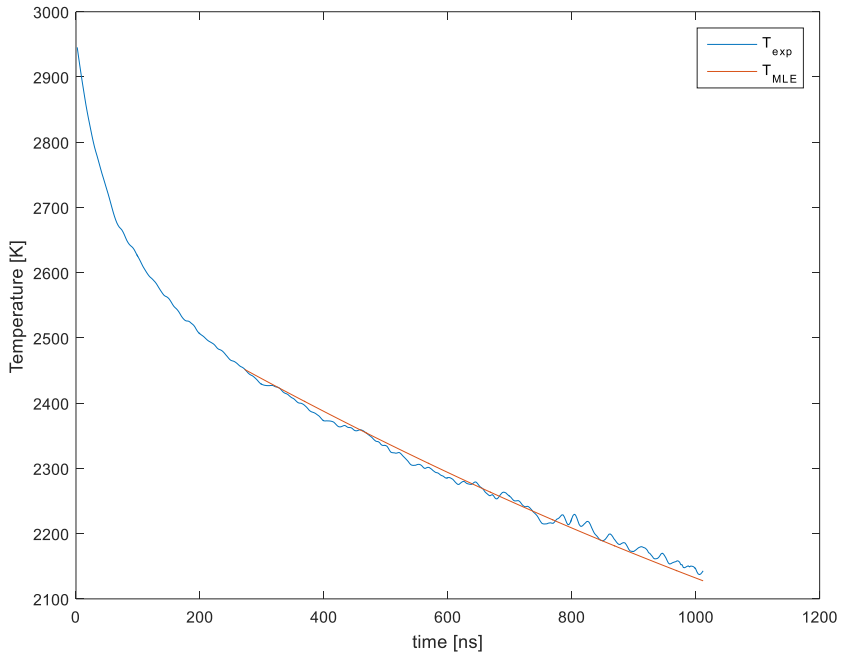

Fig. 39 Plot of the experimental and modeled temperatures for the Mo-Ar aerosol

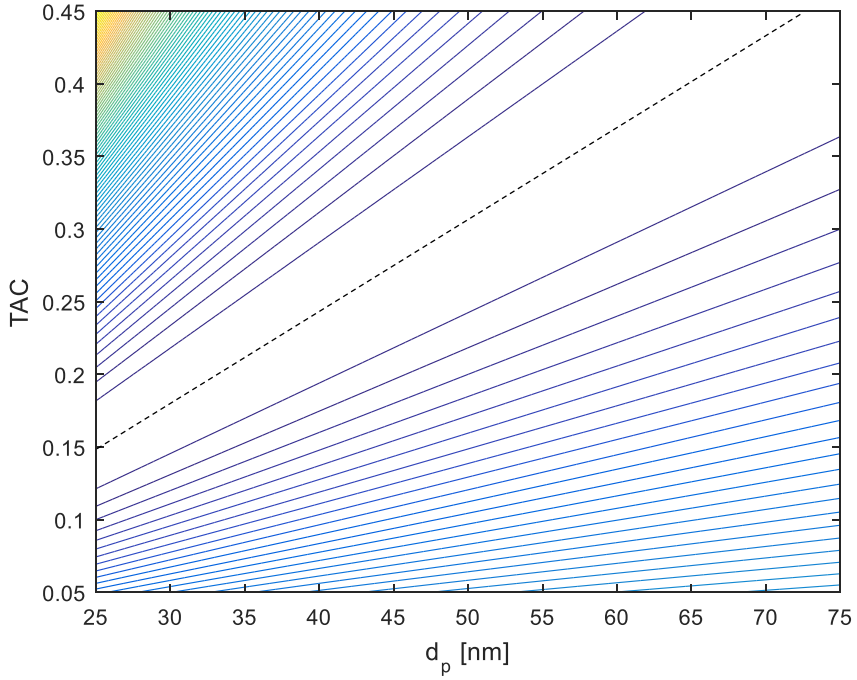

Fig. 40 Contour plot of the likelihood for the Mo-Ar aerosol

5.2.2 Perturbation Analysis

The recovered MLE values are contaminated with both the experimental noise as well as the associated uncertainties of the material properties used in both the spectroscopic and heat transfer models. Unfortunately, many of the error bounds for these parameters are not reported alongside their associated literature values, so some of the key parameters which impact the models are identified and perturbed to determine their impact on the recovered MLE values. These parameters and the perturbation factor used, as a percent, are listed in **Table** 6.

Table 6 Sensitivity analysis overview of parameters and perturbation factors

Parameter	Perturbation Factor [%]
T_g	0.5
ρ	5
c_p	5
ΔH_v	5[a]
Peak Temperature, T_{p0}	0.2
$E(\mathbf{m}_\lambda)_r$	5

[a] Molybdenum does not use a conduction model so the effects of perturbing ΔH_v are omitted

The perturbation factor is used to recalculate the MLE values for both the positive and negative scaling of parameter of interest, and taking the average of these two values results in the parameter induced error (PIE). The results of this analysis are shown in **Fig. 41**, **Fig. 42**, and **Fig.** 43 for the iron nanoparticle size and TAC, silver nanoparticle size, and molybdenum TAC respectively. For the iron nanoparticles this analysis was split between the nanoparticle size and TAC MLE values to see how the parameters influence the recovered components individually. For the iron nanoparticle size, perturbing $E(\mathbf{m}_\lambda)_r$ gave the largest deviation of approximately 46-48% , the carrier gas temperature showed almost no influence on the nanoparticle size at <2%, and the remainder of the parameters showed a moderate deviation from the nanoparticle size of approximately 10-20%.

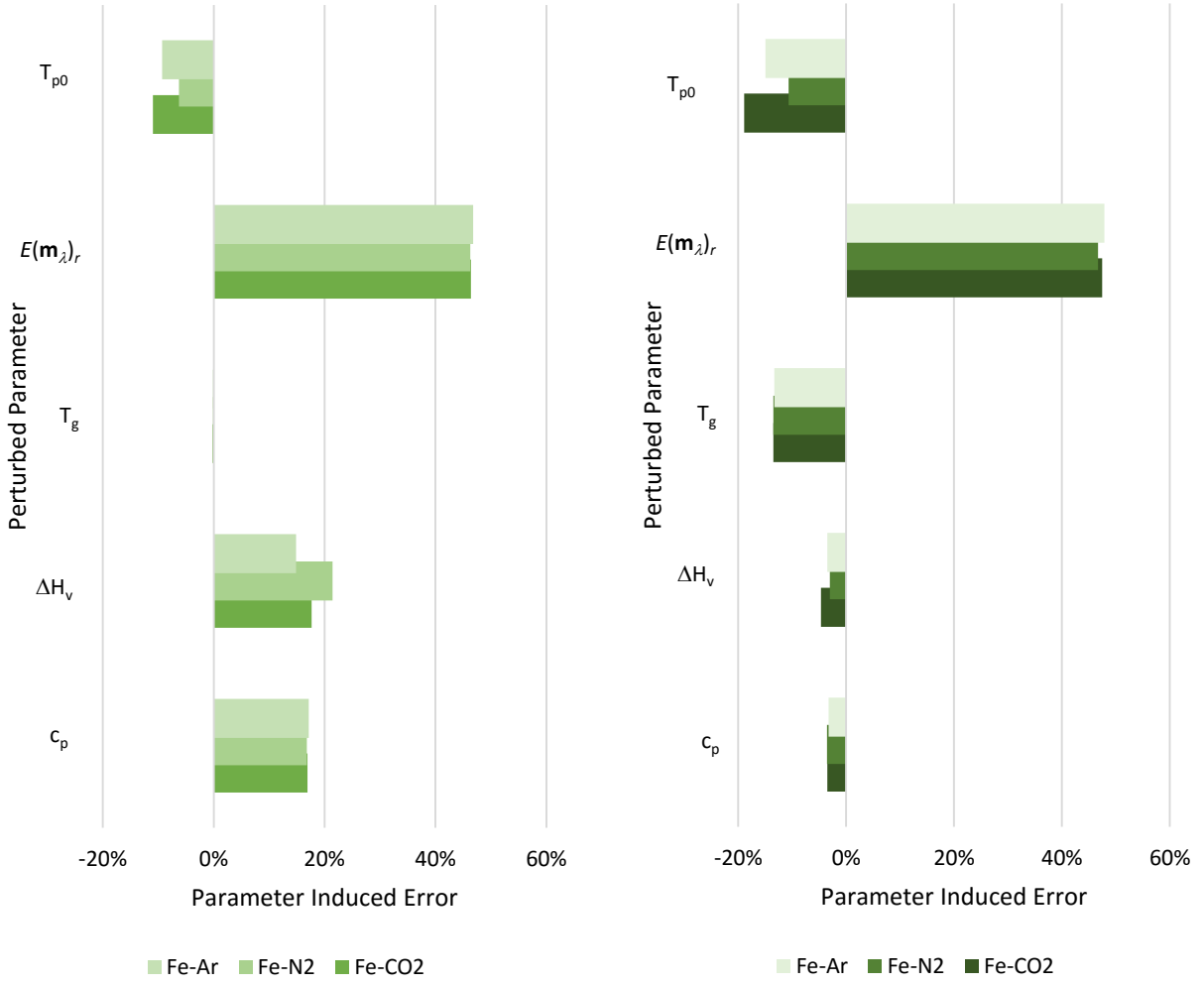

Fig. 41 Perturbation analysis results for the nanoparticle size (left) and TAC (right) for iron

For the silver nanoparticles, perturbing $E(\mathbf{m}_\lambda)_r$ and ΔH_v gave the largest deviation of approximately 35-38% from the recovered nanoparticle size, the carrier gas had no observable effect with <1%, while the peak initial temperature and the specific heat capacity showed a moderate contribution of approximately 20%. Finally for the molybdenum nanoparticles, perturbing ρ and c_p gave the largest deviation of approximately 21% from the recovered TAC value, while the remaining parameters deviated approximately 10-15%. Overall, it can be seen that perturbing $E(\mathbf{m}_\lambda)_r$ results in the most significant deviation from the recovered MLE values, although the contributions from the other parameters cannot be neglected. It is reasonable to approximate the carrier gas temperature as the room temperature, but the other parameters cannot be measured in real time, and accurate values with their error bounds need

to be determined before interpreting the TiRe-LII data. Although it is not within the scope of this and ongoing TiRe-LII studies, future work must include the accurate determination of the molten or high temperature optical properties and temperature dependent physical properties of the materials of interest.

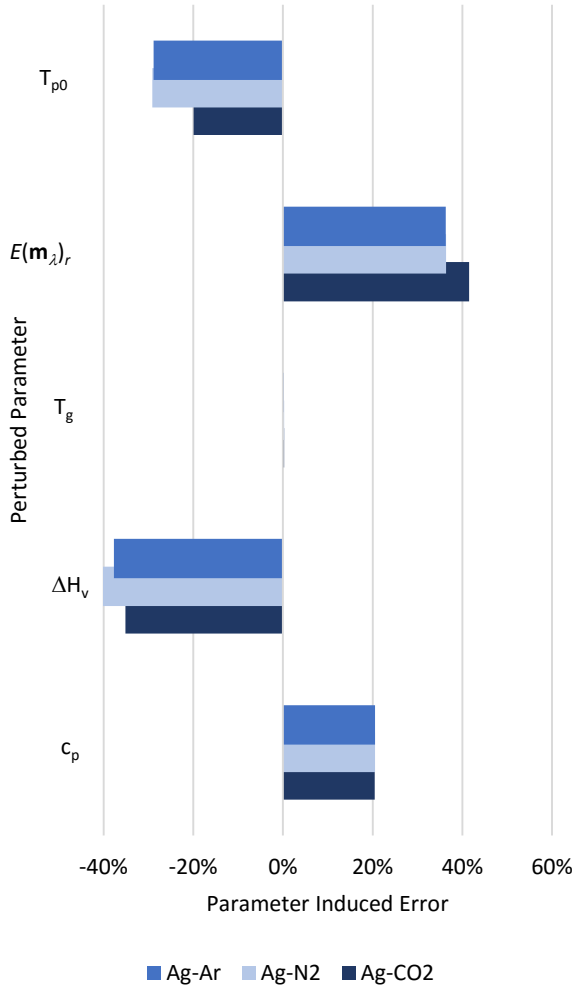

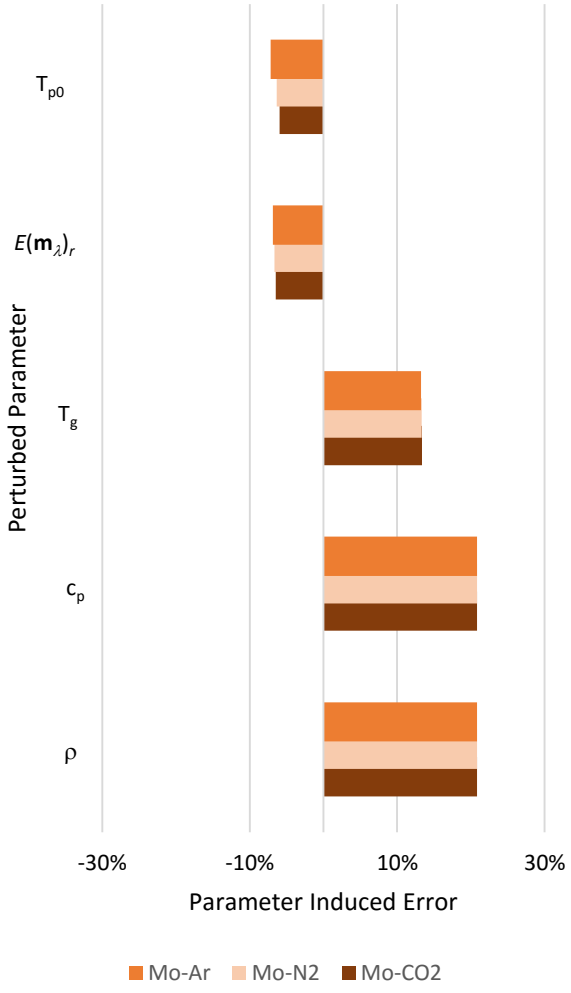

Fig. 42 (Left) Perturbation analysis results for the nanoparticle size for silver
Fig. 43 (Right) Perturbation analysis results for the TAC for molybdenum

Chapter 6 Conclusions and Future Work

This study was motivated by the need of developing a diagnostic which could provide real time aerosolized nanoparticle size measurements in a safe environment. TiRe-LII is a soot diagnostic which has been developed to conduct these nanoparticle size measurements. Previous TiRe-LII studies on synthetic zero-valent metal nanoparticles had disadvantages including: using deficient heat transfer models, not using the appropriate temperature dependent properties, or not being able to implement controls on the synthesis of the nanoparticles which make comparing results between studies difficult. In this work, each of the previous issues were addressed and the nanoparticle size and thermal accommodation coefficient were recovered for iron, silver, and molybdenum nanoparticles, when applicable.

The heat transfer model and spectroscopic models, including the temperature dependent material and optical properties required to interpret TiRe-LII measurements were presented and used to simulate the heat transfer regimes for iron, silver, and molybdenum nanoparticles. It was shown that iron has a mixture of both evaporation and conduction heat transfer modes, silver is dominated by evaporation, and molybdenum is dominated by conduction. Next, the TiRe-LII instrument calibration and setup was presented, including the laser alignment and energy measurements, as well as a brief discussion on the atomizer setup and the *ex situ* characterization that was used to compare to the TiRe-LII measurements. The nanoparticles were prepared as colloids instead of using previous gas based methods, such as hot wall reactors or excimer lasers, which provided removed the previous effect that the carrier gas had on the nanoparticle synthesis. The preparation steps for these colloids as well as their *ex situ* characterization results were then presented, along with the TiRe-LII measurement procedure.

From the fluence and spectroscopic analysis, none of the calculated $E(\mathbf{m}_\lambda)$ values for the TiRe-LII instrument's laser were consistent with the values approximated from the literature. Both iron and molybdenum peak temperatures showed the expected trend of an increasing peak temperature as the laser fluence increases while the silver nanoparticles peak temperatures were consistent for all fluences tested, as well as, the peak temperature was significantly higher than the boiling point of silver, suggesting a potential superheating effect that is not being accurately represented by the current models.

From the work done in this study, it was shown that the currently proposed heat transfer model is suitable for the recovery of the nanoparticle size and TAC for iron nanoparticles, the nanoparticle size for silver, and the nanoparticle size to TAC ratio for molybdenum. The TAC can be recovered for the

molybdenum nanoparticles if an *ex situ* derived nanoparticle size is previously determined and then used as a known model parameter. With the associated error bounds provided, it was shown that the TiRe-LII measured nanoparticle sizes were consistent with the *ex situ* nanoparticle sizes determined through electron microscopy and dynamic light scattering. This strengthens the case that TiRe-LII could be adapted to characterize synthetic aerosolized metal nanoparticles, provided that the spectroscopic and heat transfer models are well developed, as well as credible optical and physical properties of the tested nanomaterials are used.

From these results, the future studies should focus on the improvement of the error associated with the optical and physical properties of the nanoparticles used. From the perturbation analysis, almost all of the properties used in the model contributed a significant deviation from the TiRe-LII determined when a small perturbation factor was applied. Ongoing experiments are attempting to address these issues by using additional nanomaterials which may have better error bounds on their optical and physical properties, including silicon, copper, and nickel. Also, further time evolution studies and reanalysis of the previous work should be conducted to determine if there is any change in the nanoparticle morphology during an experiment which have been shown to present in the TiRe-LII size measurements for iron nanoparticles.

References

[1] T. M. Tolaymat, A. M. El Badaway, A. Genaidy, K. G. Scheckel, T. P. Luxton and M. Suidan, "Review - An evidence based envionmental perspective of manufactured silver nanoparticle in sytheses and applications: A systematic review and critical appraisal of peer-reviewed scientific papers," *Sci. Total Environ.,* vol. 408, no. 5, pp. 999-1006, 2010.

[2] D. C. Huber, "Synthesis, Properties, and Applicatins of Iron Nanoparticles," *Small,* vol. 1, no. 5, pp. 482-501, 2005.

[3] J. Park, E. Lee, N. M. Hwang, M. Kang, S. C. Kim, Y. Hwang, J. G. Park, H. J. Noh, J. Y. Kim, J. H. Park and T. Hyeon, "One-Nanometer-Level Size-Controlled Synthesis of Monodisperse Magnetic Iron Oxide Nanoparticles and their Structural and Magnetic Characterization," *Angew. Chem. Int. Edit.,* vol. 44, no. 19, pp. 2872-2877, 2005.

[4] G. Chen, I. Roy, C. Yang and P. N. Prasad, "Nanochemistry and Nanomedicine for Nanoparticle-based Diagnostics and Therapy," *Chem. Rev.,* vol. 116, no. 5, pp. 2826-2885, 2016.

[5] D. Wang, T. Xie and Y. Li, "Nanocrystals: Solution-based synthesis and applications as nanocatalysts," *Nano Research,* vol. 2, no. 1, pp. 30-46, 2009.

[6] H. H. Lara, N. V. Ayala-Nunez, L. C. I. Turrent and C. R. Padilla, "Bactericidal effect of silver nanoparticles against multidrug-resistant bacteria," *World J. Microb. Biot.,* vol. 26, no. 4, pp. 615-621, 2010.

[7] M. Stefaniuk, P. Oleszczuk and Y. S. Ok, "Review on nano zerovalent iron (nZVI): From synthesis to environmental applications," *Chem. Eng. J.,* vol. 287, pp. 618-632, 2016.

[8] T. Phenrat, T. C. Long, G. V. Lowry and B. Veronesi, "Partial Oxidation ("Aging") and Surface Modification Decrease the Toxicity of Nanosized Zerovalent Iron," *Environ. Sci. Technol.,* vol. 43, no. 1, pp. 195-200, 2009.

[9] C. R. Keenan, R. Goth-Goldstein, D. Lucas and D. L. Sedlak, "Oxidative Stress Induced by Zero-Valent Iron Nanoparticles and Fe(II) in Human Bronchial Epithelial Cells," *Environ. Sci. Technol.,* vol. 43, no. 12, pp. 4555-4560, 2009.

[10] S. Gaillet and J. M. Rouanet, "Silver nanoparticles: Their potential toxic effects after oral exposure and underlying mechanisms – A review," *Food Chem. Toxicol.,* vol. 77, pp. 58-63, 2015.

[11] K. Sheehy, A. Casey, A. Murphy and G. Chambers, "Antimicrobial properties of nano-silver: A cautionary approach to ionic interference," *J. Colloid Interf. Sci.,* vol. 443, pp. 56-64, 2015.

[12] L. Braydich-Stolle, S. Hussain and M. C. Hofmann, "In Vitro Cytotoxicity of Nanoparticles in Mammalian Germline Stem Cells," *Toxicol. Sci.,* vol. 88, no. 2, pp. 416-419, 2005.

[13] L. A. Melton, "Soot Diagnostics Based on Laser Heating," *Appl. Opt.,* vol. 23, no. 13, pp. 2201-2208, 1984.

[14] S. Schraml, S. Will and A. Leipertz, "Simultaneous Measurement of Soot Mass Concentration and Primary Particle Size in the Exhaust of a DI Diesel Engine by Time-Resolved Laser-Induced Incandescence (TIRE-LII)," *SAE Paper,* no. 01-0146, 1999.

[15] B. F. Kock, T. Eckhardt and P. Roth, "In-Cylinder Sizing of Diesel Particles by Time-Resolved Laser-Induced Incandescence (TR-LII)," *P. Combust. Inst.,* vol. 29, no. 2, pp. 2775-2782, 2002.

[16] A. V. Fillipov, M. W. Markus and P. Roth, "In-Situ Characterization of Ultrafine Particles by Laser-Induced Incandescence: Sizing and Particle Structure Determination," *J. Aerosol Sci.,* vol. 30, no. 1, pp. 71-87, 1999.

[17] R. Starke, B. Kock and P. Roth, "Nano-particle Sizing by laser-Induced Incandescence (LII) in a Shock Wave Reactor," *Shock Waves,* vol. 12, no. 5, pp. 351-260, 2003.

[18] B. F. Kock, C. Cayan, J. O. H. R. Knipping and P. Roth, "Comparison of LII and TEM sizing during synthesis of iron particle chains," *P. Combust. Inst.,* vol. 30, pp. 1689-1697, 2005.

[19] Y. Murakami, T. Sugatani and Y. Nosaka, "Laser-Induced Incandescence Study on the Metal Aerosol Particles as the Effect of the Surrounding Gas Medium," *J. Phys. Chem. A,* vol. 109, no. 40, pp. 8994-9000, 2005.

[20] T. Sipkens, G. Joshi, K. J. Daun and Y. Murakami, "Sizing of Molybdenum Nanoparticles using Time-Resolved Laser-Induced Incandescence," *J. Heat Transf.,* vol. 135, no. 5, 2013.

[21] T. A. Sipkens, R. Mansmann, K. J. Daun, N. Petermann, J. T. Titantah, M. Karttunen, H. Wiggers, T. Dreier and C. Schulz, "In Situ Particle Sizing of Silicon Nanoparticles by Time-Resolved Laser-Induced Incandescence," *Appl. Phys. B,* vol. 116, no. 3, pp. 623-636, 2014.

[22] N. R. Singh, T. A. Sipkens, K. J. Daun, N. Bizmark and M. Ioannidis, "Aerosolized Iron Nanoparticle Size Measurements Using Time Resolved Laser Induced Incandescence," in *2014 CI/CS Spring Technical Meeting*, Windsor, 2014.

[23] K. J. Daun, G. J. Smallwood and F. Liu, "Investigation of Thermal Accommodation Coefficients in Time-Resolved Laser-Induced Incandescence," *J. Heat Trans.,* vol. 130, no. 12, 2008.

[24] A. Boiarciuc, F. Foucher and C. Mounaim-Rousselle, "Soot Volume Fractions and Primary Particle Size Estimate by Means of the Simultaneous Two-Color-Time-Resolved and 2D Laser-Induced Incandescence," *Appl. Phys. B,* vol. 83, no. 3, pp. 413-421, 2006.

[25] J. Black and M. Johnson, "In-Situ Laser-Induced Incandescence of Soot in an Aero-Engine Exhaust: Comparison with Certification Style Measurements," *Aerosp. Sci. Technol.,* vol. 14, no. 5, pp. 329-337, 2010.

[26] R. L. Vander Wal, T. M. Ticich and J. R. West, "Laser-Induced Incandescence Applied to Metal Nanostructures," *Appl. Opt.,* vol. 38, no. 27, pp. 5867-5879, 1999.

[27] F. Liu, K. J. Daun, D. R. Snelling and G. J. Smallwood, "Heat Conduction from a Spherical Nano-Particle: Status of Modelling Heat Conduction in Laser-Induced Incandescence," *Appl. Phys. B,* vol. 83, no. 3, pp. 355-382, 2006.

[28] A. Eremin, E. Gurentsov and C. Schulz, "Influence of the Bath Gas on the Condensation of Supersaturated Iron Atom Vapour at Room Temperature," *J. Phys. D: Appl. Phys.,* vol. 41, no. 5, pp. 1-5, 2008.

[29] K. J. Daun, "Thermal Accommodation Coefficients Between Polyatomic Gas Molecules and Soot in Laser-Induced Incandescence Experiments," *Int. J. Heat Mass Transfer,* vol. 52, no. 21, pp. 5081-5089, 2009.

[30] K. J. Daun, J. T. Titantah and M. Karttunen, "Molecular Dynamics Simulation of Thermal Accommodation Coefficients for Laser-Induced Incandescence Sizing of Nickel Particles," *Appl. Phys. B,* vol. 107, no. 1, pp. 221-228, 2012.

[31] J. Reimann, H. Oltmann, S. Will, C. Bassano, E. L. Lösch and S. Günther, "Laser Sintering of Nickel Aggregates Produced from Inert Gas Condensation," in *Proceedings of the World Conference on Particle Technology*, Nuremberg, Germany, 2010.

[32] T. Lehre, R. Suntz and H. Bockhorn, "Time-Resolved Two-Color LII: Size Distributions of Nano-Particles from Gas-to-Particle Synthesis," *P. Combust. Inst.,* vol. 30, no. 2, pp. 2585-2593, 2005.

[33] F. Cignoli, C. Bellomunno, S. Maffi and G. Zizak, "Laser-Induced Incandescence of Titania Nanoparticles Synthesized in a Flame," *Appl. Phys. B,* vol. 96, no. 4, pp. 593-599, 2009.

[34] S. Maffi, F. Cignoli, C. Bellomunno, S. De luliis and G. Zizak, "Spectral Effects in Laser Induced Incandescence Application to Flame-made Titania Nanoparticles," *Spectrochim. Acta B,* vol. 63, no. 2, pp. 202-209, 2009.

[35] B. Tribalet, A. Faccinetto, T. Dreier and C. Schultz, "Evaluation of Particle Sizes of Iron-Oxide Nano-Particles in a Low-Pressure Flame-Synthesis Reactor by Simultaneous Application of TiRe-LII and PMS," in *5th Workshop on Laser-induced Incandescence*, Le Touquet, France, 2012.

[36] I. S. Altman, D. Lee, J. Song and M. Choi, "Experimental Estimate of Energy Accommodation Coefficient at High Temperatures," *Phys. Rev. E,* vol. 64, no. 5, 2001.

[37] T. A. Sipkens, N. R. Singh, K. J. Daun, N. Bizmark and M. Ioannidis, "Examination of the Thermal Accommodation Coefficient Used in the Sizing of Iron Nanoparticles by Time-Resolved Laser-Induced Incandescence," *Appl. Phys. B,* vol. In press., 2015.

[38] M. F. Modest, Radiative Heat Transfer, 3rd Ed., San Diego: Academic Press, 2013.

[39] D. R. Snelling, G. J. Smallwood, F. Liu, O. L. Gulder and W. D. Bachalo, "A Calibration-Independent Laser-Induced Incandescence Technique for Soot Measurement by Detecting Absolute Light Intensity," *Appl. Opt.,* vol. 44, no. 31, pp. 6773-6785, 2005.

[40] T. C. Bond and R. W. Bergstrom, "Light Absorption by Carbonaceous Particles: An Investigative Review," *Aerosol Sci. Tech.,* vol. 40, pp. 27-67, 2006.

[41] J. A. Creighton and D. G. Eadon, "Ultraviolet-Visible Absorption Spectra of the Colloidal Metallic Elements," *J. Chem Soc. Faraday Trans.,* vol. 87, pp. 3881-3891, 1991.

[42] K. M. Watson, "Thermodynamics of the Liquid State," *Ind. Eng. Chem.,* vol. 35, no. 4, pp. 398-406, 1943.

[43] J. C. Miller, "Optical Properties of Liquid Metals at High Temperatures," *Phil. Mag.,* vol. 20, no. 168, pp. 1115-1132, 1969.

[44] J. N. Hodgson, "Infra-red Measurements of the Optical Constants of Liquid Silver," *Philos. Mag.,* vol. 5, pp. 272-277, 1960.

[45] S. Krishnan, G. P. Hansen, R. H. Hauge and J. L. Margrave, "Spectral Emissiviites and Optical Properties of Electromagnetrically-Levitated Liquid Metals as Functions of Temperature and Wavelength," *High Temp. Sci.,* vol. 29, pp. 17-52, 1990.

[46] C. F. Bohren and D. R. Huffman, Absorption and Scattering of Light by Small Particles, New York: John Wiley & Sons, 1983.

[47] M. Quinten, Optical Properties of Nanoparticle Systems: Mie and Beyond, New York: John Wiley and Sons, 2011.

[48] H. Kobatake, H. Khosroabadi and H. Fukuyama, "Normal spectral emissivity measurement of liquid iron and nickel using electromagnetic levitation in direct current magnetic field," *Met. Trans. A,* vol. 43A, pp. 2466-2472, 2012.

[49] T. E. Faber, Introduction to the Theory of Liquid Metals, Cambridge, UK: Cambridge University Press, 1972.

[50] P. F. Paradis, T. Ishikawa and Y. Nosaka, "Noncontact Measurements of Thermophysical Properties of Molybdenum at High Temperatures," *Int. J. Thermophys.,* vol. 23, no. 2, pp. 555-569, 2002.

[51] B. T. Barnes, "Optical Constants of Incandescent Refractory Metals," *J. Opt. Soc. AM,* vol. 56, pp. 1546-1550, 1966.

[52] D. W. Juenker, L. J. LeBlanc and C. R. Martin, "Optical properties of some transition metals," *J. Opt. Soc. AM,* vol. 58, pp. 164-171, 1968.

[53] E. D. Palik, Handbook of Optical Constants of Solids, London: Elsevier, 2012.

[54] R. S. Hixson, M. A. Winkler and M. L. Hodgdon, "Sound Speed and Thermoyhysical Properties of Liquid Iron and Nickel," *Phys. Rev. B,* vol. 42, no. 10, pp. 6485-6491, 1990.

[55] A. V. Grosse and A. D. Kirshenbaum, "The temperature range of liquid lead and silver and an estimate of their critical constants," *J. Inorg. Nucl. Chem.,* vol. 24, pp. 739-748, 1962.

[56] P. D. Desai, "Thermodynamic Properties of Iron and Silicon," *J. Phys. Chem. Ref. Data,* vol. 15, no. 3, pp. 967-983, 1986.

[57] C. Cagran, W. Wilthan and G. Pottlacher, "Enthalpy, Heat of Fusion, and Specific Electrical Resistivity of Pure Silver, Pure Copper, and the Binary Ag-28Cu Alloy," *Thermochim. Acta,* vol. 445, pp. 104-110, 2006.

[58] J. A. Dean, Lange's Handbook of Chemistry, 15th ed., McGraw-Hill, 1999.

[59] F. Mafune, J.-Y. Kohno, Y. Takeda and T. Kondow, "Formation of Stable Platinum Nanoparticles by Laser Ablation in Water," *J. Phys. Chem. B ,* vol. 107, pp. 4218-4223, 2003.

[60] CRC Handbook of Chemistry and Physics, 96th Edition, 2015-2016, Cleveland, Ohio: CRC Press, 2015.

[61] D. A. Young and B. J. Alder, "Critical Point of Metals from the van der Waals Model," *Phys. Rev. A,* vol. 3, no. 1, pp. 364-371, 1971.

[62] P. D. Desai, "Thermodynamic Properties of Manganese and Molybdenum," *J. Phys. Chem. Ref. Data,* vol. 16, no. 1, pp. 91-108, 1987.

[63] B. J. Keene, "Review of Data for the Surface Tension of Iron and its Binary Alloys," *Int. Mater. Rev.,* vol. 33, no. 1, 1988.

[64] R. Novakovic, E. Ricci, D. Giuranno and A. Passerone, "Surface and transport properties of Ag-Cu liquid Alloys," *Surf. Sci.,* vol. 576, pp. 175-187, 2005.

[65] H. M. Lu and Q. Jiang, "Surface Tension and Its Temperature Coefficient for Liquid Metals," *J. Phys. Chem. B,* vol. 109, no. 32, pp. 15463-15468, 2005.

[66] T. A. Sipkens, R. Mansmann, K. J. Daun, N. Petermann, J. T. Titantah, M. Karttunen, H. Wiggers, T. Dreier and C. Schulz, "In Situ Nanoparticle Size Measurements of Gas-Borne Silicon Nanoparticles by Time-Resolved Laser-Induced Incandescence," *Appl. Phys. B,* vol. 116, no. 3, pp. 623-636, 2013.

[67] P. C. Hiemenz and R. Rajagopalan, Principles of Colloid and Surface Chemistry Third Edition, Revised and Expanded, Boca Raton: CRC Press, Taylor & Francis Group, 1997.

[68] Y. Leng, Materials Characterization Introduction to Microscopy and Spectroscopic Methods, Singapore: John Wiley & Sons (Asia) Pte Ltd, 2008.

[69] Y. Liu, S. A. Majetich, R. D. Tilton, D. S. Scholl and L. and G. V., "TCE Dechlorination Rates, Pathways, and Efficiency of Nanoscale Iron Particles with Different Properties," *Environ. Sci. Tech.,* vol. 39, no. 5, pp. 1338-1345, 2005.

[70] F. He and D. Zhao, "Manipulating the Size and Dispersibility of Zerovalent Iron Nanoparticles by use of Carboxymethyl Cellulose Stabilizers," *Environ. Sci. Technol.,* vol. 41, no. 17, pp. 6216-6221, 2007.

[71] T. Phenrat, H. J. Kim, F. Fagerlund, T. Illangasekare, R. D. Tilton and G. V. Lowry, "Particle Size Distribution, Concentration, and Magnetic Attraction Affect Transport of Polymer-Modified Fe0 Nanoparticles in Sand Columns," *Environ. Sci. Technol.,* vol. 43, no. 15, pp. 5079-5085, 2009.

[72] P. C. Lee and D. Meisel, "Adsorption and surfance-enhanced Raman of dyes on silver and gold sols," *J. Phys. Chem,* vol. 86, no. 17, pp. 3391-3395, 1982.

[73] A. D. Rakić, A. B. Djurišić, J. M. Elazar and M. L. Majewski, "Optical properties of metallic films for vertical-cavity optoelectronic devices," *Appl. Opt.,* vol. 37, no. 22, pp. 5271-5283, 1998.

[74] M. A. Ordal, R. J. Bell, R. W. Alexander, L. L. Long and M. R. Querry, "Optical properties of fourteen metals in the infrared and far infrared: Al, Co, Cu, Au, Fe, Pb, Mo, Ni, Pd, Pt, Ag, Ti, V, and W," *Appl. Opt.,* vol. 24, no. 24, pp. 4493-4499, 1985.

[75] S. De Iuliis, F. Migliorini, F. Cignoli and G. Zizak, "Peak soot temperature in laser-induced incandescence measurements," *Appl. Phys. B,* vol. 2006, pp. 397-402, 2005.

[76] A. Eremin, E. Gurentsov, E. Popova and K. Priemchenko, "Size Dependence of Complex Refractive Index Function of Growing Nanoparticles," *Appl. Phys. B,* vol. 104, no. 2, pp. 289-295, 2011.

[77] A. Eremin, E. Gurentsov, E. Mikheyeva and K. Priemchenko, "Experimental Study of Carbon and Iron Nanoparticle Vaporisation Under Pulse Laser Heating," *Appl. Phys. B,* vol. 112, no. 3, pp. 421-432, 2013.

[78] A. V. Eremin and E. V. Grentsov, "Sizing of Mo Nanoparticles Synthesized by Kr-F Laser Pulse Photo-Dissociation of Mo(CO)6," *Appl. Phys. A,* vol. 119, pp. 615-622, 2015.